공학박사학위논문

양파장 HiLo 이미징 기법을 활용한 고속 고해상도 3차원 프로파일 측정 시스템 개발

High-speed high-resolution 3D profile measurement system with dual-wavelength HiLo optical imaging technique

February, 2019

School of Mechanical & Aerospace Engineering
Seoul National University

Sewon Kang

양파장 HiLo 이미징 기법을 활용한
고속 고해상도 3 차원 프로파일 측정 시스템 개발

High-speed high-resolution 3D profile measurement system with dual-wavelength HiLo optical imaging technique

지도교수 고 상 근

이 논문을 공학박사학위논문으로 제출함

2018년 10월

서울대학교 대학원

기계항공공학부

강세원

강세원의 공학박사학위논문을 인준함

2018년 12월

위 원 장	**박 희 재 (인)**
부위원장	**고 상 근 (인)**
위 원	**고 승 환 (인)**
위 원	**김 대 근 (인)**
위 원	**임 시 형 (인)**

Abstract

High-speed high-resolution 3D profile measurement system with dual-wavelength HiLo optical imaging technique

Sewon Kang

School of Mechanical & Aerospace Engineering

The Graduate School

Seoul National University

Various techniques to measure the three-dimensional (3D) surface profile of a 3D micro- or nanostructure have been proposed. However, it is difficult to apply such techniques directly to industrial uses because most of them are relatively slow, unreliable, and expensive. HiLo optical imaging technique, which was recently introduced in the field of fluorescence imaging, is a promising wide-field imaging technique capable of high-speed imaging with a simple optical configuration. It has not been used in measuring a 3D surface profile although confocal microscopy originally developed for fluorescence imaging has been adapted to the field of 3D optical measurement for a long time. In this paper, to the best of our knowledge, HiLo optical imaging technique for measuring a 3D surface profile is proposed for the first time. Its optical configuration and algorithm for a precisely detecting surface position are designed, optimized, and implemented. In addition, a dual-wavelength HiLo method that removes the physical movement of the grating filter by using dual-wavelength light to further improve speed is proposed, and it is shown that with this method images similar to real-time images can be acquired without degradation of performance. Optical performance for several 3D microscale structures is

evaluated, and it is confirmed that the capability of measuring a 3D surface profile with HiLo optical imaging technique is comparable to that with confocal microscopy.

Keywords : 3D imaging, HiLo technique, Dual-wavelength illumination, Height measurements, High-speed imaging

***Student Number*: 2000-30646**

TABLE OF CONTENTS

LIST OF FIGURES

LIST OF TABLES

LIST OF VARIABLES

t	: Normalized x-axis displacement ($=\frac{2\pi}{\lambda} xNA$)	23
w	: Normalized y-axis displacement ($=\frac{2\pi}{\lambda} yNA$)	23
v	: Normalized distance from origin ($=\sqrt{t^2+w^2}$)	23
$J_0(\ )$	: Zero-order Bessel function of the first kind	23
$P(\rho)$	: Pupil function of defocus	23
$\tilde{\nu}$	: Normalized grid spatial frequency ($=\frac{8\pi}{\lambda} z\sin^2(\frac{\alpha}{2})$)	24
u	: Normalized axial movement ($=\frac{\lambda}{NA}\frac{2\pi}{p}$)	24
$J_1(\ )$	: Bessel function of the first kind	24
α	: Half the angular aperture of the objective lens	24
n	: Refractive index of the optical medium	27
$\vec{\rho}$	: Distance from origin, $\sqrt{x^2+y^2}$	53
$O(\vec{\rho})$	: Numerical model of the object shape	53
PSF	: Point spread function of the optical system	53
f	: Focal length of the lens	57
δ_{focal}	: Focal position difference of lens caused by wavelength difference of two illumination lights	59
N	: Number of images in image stack	73
t_{align}	: Image registration time of two images	75
$\Delta x_1, \Delta y_1, \Delta x_2, \Delta y_2$	: Lateral displacement values of each image slice by applying image registration algorithm	77,78
$z_{focal}(x,y)$	: Surface position at given lateral position *(x,y)*	80
$i(a,b)$	: Gray value of each image slice at *(a,b)* point	80

f	: Curve fitting function (Gaussian or parabola)	81
σ	: Standard deviation	81
M	: 5 × 5 or 7 × 7 intensity matrix near *(a,b)* point	81
$m(x, y)$	: Mean gray value of a 3 × 3 matrix near the lateral position *(x,y)*	82
$\vec{\upsilon}$	: Normal vector of a plane	97
$\vec{k}$	: Unit normal vector of x-y plane	97
θ	: Angle between normal vector $\vec{\upsilon}$ of specific plane and the unit normal vector $\vec{k}$ of x-y plane	97
$\vec{u}$	: Cross product of normal vector of specific plane and unit normal vector of x-y plane	99
R	: Rotation matrix of specific plane by θ with $\vec{u}$ as the rotation axis	99

CHAPTER 1.
INTRODUCTION

1.1. Motivation

The use of micro- and nanotechnologies in the electronic components such as semiconductors and sensors as well as products in various industries such as chemical, textile, pharmaceutical, and robotics, has been continuously increasing. Accordingly, there is continuing demand for measuring the surface profiles of these 3D micro- and nanostructures. As the size of 3D structures decreases to the micro- and nanoscale, 3D shapes should be precisely measured at this level, but this results in longer measuring times for 3D shapes. It is also becoming increasingly important to quantify their surface profiles in real time by installing inspection equipment directly on the production line, to improve product quality and reduce the defect rate [1]. Therefore, the techniques for assessing the 3D surface profiles of micro- and nanostructures should not only have reasonable precision with high accuracy, but also real-time measurement capability. Furthermore, these techniques should be cost-effective and highly reliable, and preferably noncontact, where the sample is measured without being contaminated or deformed [2].

Representative 3D profile measurement techniques

Representative techniques for measuring the surface profile of a 3D micro- or nanostructure have been proposed for a long time. Electron microscope [3] has higher

resolving power (in the order of a nanometer) than a typical optical microscope, but it operates in a vacuum and requires sample preprocessing such as gold coating. Moreover, transmission electron microscopy (TEM) [4] is quite expensive, and scanning electron microscopy (SEM) [5] requires significant image-acquisition time.

For this reason, despite the excellent performance of electron microscopy, it is more reasonable to use an optical measuring device that utilizes visible light for non-contact measurement in micro scale. The optical measuring device can be used at room temperature and atmospheric pressure, so there are no restrictions on environmental factors, and it is advantageous in terms of cost compared to the electron microscope since expensive vacuum equipment such as a vacuum chamber is not required. Furthermore, as the measurement technology continues to develop, it becomes possible to measure up to the sub-micro range close to the diffraction limit. As a result, the application range of the optical measuring device is being expanded.

In the field of 3D measurement using visible light, atomic force microscopy (AFM) [6][7], interferometry and white light interferometry (WLI) [8], laser scanning confocal microscopy (LSCM) [8], and structured illumination microscopy (SIM) [9] are being used. Among them, AFM has the best performance and is used for precision measurement in nano scale. However, since it has a slow image speed and limited measurement range, WLI and LSCM are commonly used for MEMS structure measurement corresponding to micro and sub-micro scale do. More detailed features and advantages and disadvantages of each technique are as follows.

AFM is a type of point-scanning microscopy that can achieve high measurement accuracy at the sub-nanometer level. The height and shape of the specimen are obtained by scanning the specimen with a probe with a nano-scale tip at the end of a fine flexible cantilever,

and sensing the height change of the probe with laser. The tip of the probe can be classified into a contact type in which the probe is in direct contact with the surface of the sample, and a non-contact type in which the attraction and repulsion between atoms are balanced to maintain a constant gap with the sample. As mentioned above, AFM has excellent vertical and horizontal accuracy with sub-nanometer resolution. The 3D shape of the specimen can be directly measured without additional mathematical analysis. But AFM has a relatively small field of view, and its height measurement range is only a few micrometers. And also, it generates surface profile very slowly, due to its scanning nature.

LSCM, another point-scanning technology, has an axial resolution of ~ 10 nanometer scale and has a lateral resolution close to the diffraction limit of the incident light source. The LSCM can obtain three-dimensional voxel information by placing a pin-hole on the front of the detector in the same optical system as a general optical microscope, and passing light through only the focused position to a specific point of the specimen. That is, by dismissing signals that are not in the surface position, it is possible to selectively recognize the surface information of the specimen more accurately, thereby achieving excellent axial resolution. However, in order to acquire information of one image for the whole specimen, it is difficult to perform high-speed imaging because either the laser light source or the specimen has to be moved sequentially to the x-y axis. At the same time, the scanning of moving the focus position of the objective lens in the z-axis direction is required for 3D reconstruction. Therefore, it takes a long time to reconstruct the 3D surface profile. In the case of the latest commercial LSCM, the acquisition time of the 3D image signal is shortened to within several tens of seconds by using the optical laser and the high-speed micro mirror, but it is difficult to further improve the image speed due to the structural limit to be scanned in both the horizontal and vertical directions.

A variety of 3D imaging techniques have been developed to overcome the slow acquisition speed of point scanning methods such as AFM and LSCM.

The best technique in terms of speed is fringe-pattern projection (FPP) [10]. It is possible to reconstruct the 3D profile with only one image acquisition by illuminating the structured illumination diagonally and measuring the displacement of the pattern formed on the surface of the specimen. However, since FPP cannot acquire information on the shadow region generated on the surface of the specimen, it is difficult to reconstruct the profile of the entire specimen, and precise measurement is limited as the axial resolution is twice as high as that of LSCM. For this reason, it is useful for rough 3D restoration such as handheld 3D scanner, but is rarely utilized in actual micro- and nano structure measuring equipment.

For this reason, techniques such as SIM or WLI that acquires acquiring a wide field image in the x-y plane and reconstructing the 3D profile through z-axis scanning are widely used as measurement methods capable of satisfying both speed and precision.

WLI, one of the most widely used wide-field surface profilers, is a kind of interferometry. Interferometry, originally developed by Michelson [11], utilizes two separate light interferences to determine the location of the specimen surface. WLI is a technique that overcomes the limitation of height measurement range which is a disadvantage of existing interferometry by using white light combined multiple wavelengths instead of incident light of single wavelength. This technique has a very precise axial resolution (on the order of a nanometer), whereas its lateral resolution is the same as for a conventional optical microscope. However, it is hard to measure very steep surfaces with WLI, because the interference fringes disappear [12]. Also, it is very sensitive to changes in the external

environment, since it utilizes the minute interference phenomenon of the light source, making the design and implementation of its optical system difficult.

SIM, another wide-field imaging-based technology, has the advantage of simple configuration to insert a grating pattern into the optical illumination path in wide-field microscopy (WFM) while maintaining comparable axial resolution to LSCM, which is highly competitive in terms of imaging speed and cost. Nevertheless, there is a hurdle to acquire images in real-time, since at least three sequential images with spatial phase shift of the grating pattern are required to generate the 3D surface profile. In addition, a large number of measurement errors are likely to occur in the process of moving the grating position sequentially by 1/3 of the spatial frequency in order to implement the phase shift.

Therefore, none of these 3D profile measurement techniques simultaneously satisfies the functional requirements including cost effectiveness, high precision, and real-time measurement, and there remains a demand for a new outstanding 3D profile measurement method to overcome these limitations.

Development target of this study

In this study, we will develop a 3D profile measurement technique that satisfies conditions such as high speed, high precision, and cost effectiveness for easy use in the industrial field. The specimen to be measured is a structure of several tens to several hundred micrometer scale, which is a scale corresponding to a flat panel display. The height measurement accuracy is aimed at a sub-micro level similar to LSCM. Although it will not be applicable to the semiconductor industry where the patterns are of several nanometers, it will be applicable to more general uses including inspection of flat panel

display, solar panel, metal powder, and functional MEMS structure, etc. Especially, if high-speed 3D profile measurement close to real-time is possible, its industrial application will be wider than that of conventional 3D measurement techniques. At the same time, we aim to lower the production cost to less than KRW 10 million, so that it will be 5 ~ 10 times more cost competitive than conventional techniques.

Investigating 3D profile measurement techniques that can meet the target specification

In order to develop the optical technology that can satisfy the target specification, we first investigate the existing measurement technique and judge whether it is applicable to the 3D profile measurement. Considering that many techniques such as LSCM and SIM have been introduced for the first time in the field of fluorescence staining and the application range has been expanded by measuring the surface profile, it is effective to investigate measurement techniques focusing on the field of fluorescence staining. First, the point scanning method is not suitable in terms of speed and should be excluded. In addition, it is difficult to use fringe projection because it is affected by shadow and has a measurement accuracy of 100 μm or more. Since the reliability of the measurement must be ensured even with the changes in ambient environment, such as vibration, it is difficult to apply interferometer which has a complex optical system and easily affected by vibration. In conclusion, structured illumination is the most realistic alternative. However, as described above, a conventional SIM has a limitation in real-time measurement and a new method is needed to improve the imaging speed. Here we have found the possibility of achieving

the development goal by applying HiLo imaging technique which was introduced and developed in the field of fluorescent dyeing to 3D surface profile measurement.

HiLo imaging technique, developed by Lim D *et al.* (2008) [13] and J. Mertz (2011) [14], is a kind of wide-field fluorescence microscopy (WFFM). This is a way to obtain 3D resolution close to a LSCM by signaling only two images, one structured illumination image and one uniform illumination image. This technology utilizes the same structured illumination as a SIM, but it requires only two images to obtain a 2D image, which allows for high-speed imaging compared to a SIM which requires a minimum of three image acquisitions. In addition, it has the merit of simpler and more robust optical configuration because it can acquire images by simply moving the entire grating, compared to SIM where the grating pattern must be precisely changed by 1/3 of the spatial frequency to obtain three images. It also has the advantage of having 3D optical resolution close to the LSCM. That is, it is suitable for high-speed and high-resolution images.

1.2. Previous research for HiLo imaging technique

HiLo imaging technique was first introduced in the field of fluorescence imaging in 2008 [13], and there have been various studies such as *in vivo* imaging using speckle illumination [15], endoscopic-image enhancement with structured illumination [16][17], imaging speed improvement by using two types of fluorescent dye to acquire two images simultaneously [18], and a light sheet-illumination-based 3D HiLo technique removing residual background noise [19]. This technique utilizes a grating similar to SIM's, but it is faster, simpler and more economical than SIM in that it only requires two images while

keeping its lateral resolution same as for SIM. This technique has potential for measuring a 3D surface profile without an expensive scanning optical device, as the LSCM used in fluorescence imaging was modified to reflected-light LSCM widely utilized in 3D surface profile inspection. Moreover, up till now, there has been no report on 3D surface profile measurement with HiLo optical imaging technique.

1.3. Main objectives

The main object of this study is to develop a high-speed, high-resolution, cost-effective optical 3D structural measuring system by applying HiLo technique. In addition, a novel technique for enhancing the speed of HiLo technique and realizing the image acquisition at a speed close to real-time is proposed. In order to accomplish this, the following implementation and verification were performed sequentially.

In Chapter 2, we show that HiLo imaging technique is not confined to fluorescence imaging, but can be applied to the measurement of the reflected light of the specimen, *i.e.* the surface profile. In order to achieve this, the HiLo algorithm proposed in previous research was mathematically verified and modified to fit the reflected light measurement. In order to verify the performance, hardware and software were built by utilizing general optical components, general purpose software and open source library. In addition, the core factors that affect the performance of HiLo image were selected, and the optimal values were found through experiments on multiple cases.

The lateral and axial resolutions of HiLo images were evaluated, and it was confirmed that high-speed imaging was possible for wide-field surfaces while maintaining high resolution as measured by LSCM.

In Chapter 3, we proposed a dual-wavelength HiLo technique that improving the image acquisition speed of the HiLo imaging technique presented in Chapter 2 by separating incident light and simultaneously imaging incident light of different wavelengths. With the existing HiLo imaging technique, the grating filter replacement and the light source imaging were inevitably performed sequentially. With the proposed technique, a light source which has passed through a grating filter and a light source which has not passed through a pattern filter are simultaneously illuminated, separated by a bandpass filter and simultaneously detected. The imaging speed is thereby improved by acquiring two images at once.

However, unlike existing HiLo, lens aberration causes errors due to the simultaneous use of two different wavelengths. In addition, two optical systems and two cameras are used, complicating the optical system and giving rise to optical system registration issue. In consideration of these factors, the method of image correction is also taken into account.

In Chapter 4, we proposed a 3D reconstruction algorithm that can reconstruct the image acquired through HiLo imaging method in 3D, and obtained an actual 3D image and compared it with existing 3D profile measurement technique such as LSCM. To do this, we proposed an algorithm to reconstruct the surface profile in 3D using the HiLo image stack obtained sequentially while moving the position of the objective lens focus in the z direction. The method of finding the height of the surface using the characteristic that the intensity is strongest in the focal plane was applied in a manner similar to that used in focus variation microscopy [8] (or shape from focus [20]) and LSCM.

In order to verify the performance, we compared the precision of measured values for 3D surface profile and height profile obtained by three methods, HiLo, dual-wavelength HiLo, and LSCM, based on the results of measurement with standard step-height sample and protected silver mirror specimen. In order to confirm the measurement performance of the slope surface, we compared the results through the experiments on the smooth surface and the rough surface.

Then, we selected various samples and measured them with LSCM, existing HiLo, and dual-wavelength HiLo techniques, and compared the results. We confirmed that it is possible to obtain a 3D surface profile similar to LSCM with both existing HiLo and dual-wavelength HiLo.

CHAPTER 2.

HILO IMAGING TECHNIQUE FOR SURFACE PROFILE MEASUREMENT

2.1. Basic optics of microscopy

Light passing through a lens cannot focus exactly on one point due to diffraction. Therefore, even if the sample is positioned exactly on the focal plane as shown in Figure 2.1, a blurred image compared to the original shape is acquired

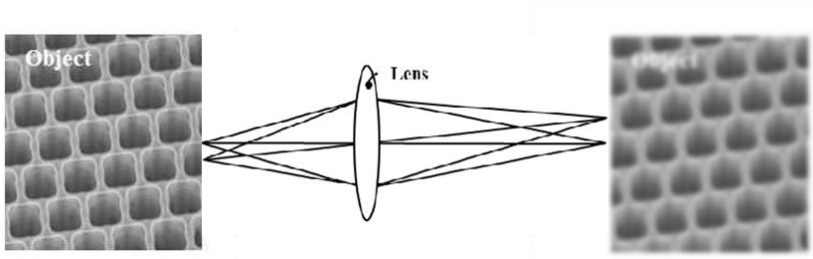

Figure 2.1 Lens diffraction effect and microscope image

The optical resolution is defined as the limit distance at which two points cannot be recognized because of the diffraction of light. As shown in Figure 2.2, lateral resolution and axial resolution can be distinguished by direction [21]. In general, optical resolution is determined by the numerical aperture (NA) of the lens and the wavelength of the light source. For general microscopy, lateral and axial resolution is expressed as Eq. (2.1)

$$R_{lateral} = 0.61\frac{\lambda}{NA},\ R_{axial} \propto \frac{\lambda}{NA^2} \tag{2.1}$$

where, *NA* : Numerical Aperture of lens, and

λ : Wavelength of illuminated light.

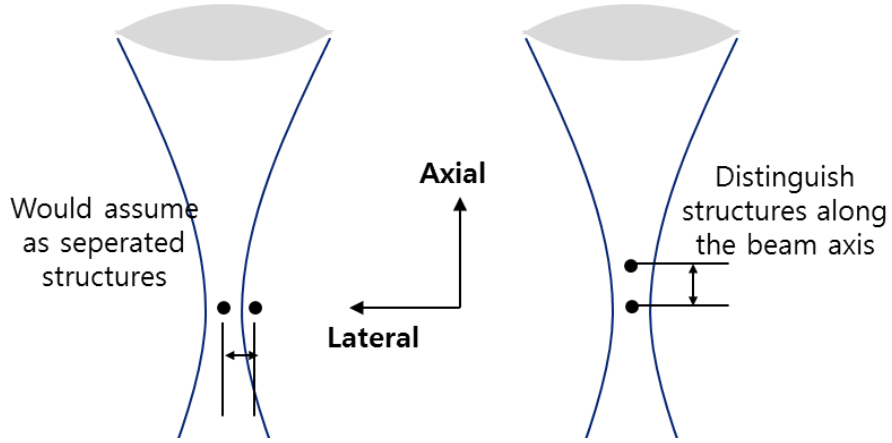

Figure 2.2 Concept diagram of lateral resolution (left) and axial resolution (right); modified from M. Peikari *et al.* [21]

Theoretically, optical microscopy can measure up to the resolution limit due to diffraction. In reality, we can only obtain microscopic images that do not meet the theoretical resolution. This is because in a general microscopic image acquisition process, the in-focus image in the axial direction of the incident light and the out-of-focus blurred image are not distinguished from each other and are acquired in a superimposed state as shown in Figure 2.3. If only the out-of-focus component, *i.e.*, the image component measured at the out-of-focus portion can be selectively removed, only the image acquired from the actual focal plane can be observed, and a measurement value close to the optical resolution

limit can be obtained. In addition, since the out-of-focus component is the physical measurement of image components at different heights in the focal plane and the z-axis direction, the resolution in the z-axis direction can be improved if the out-focus component is removed.

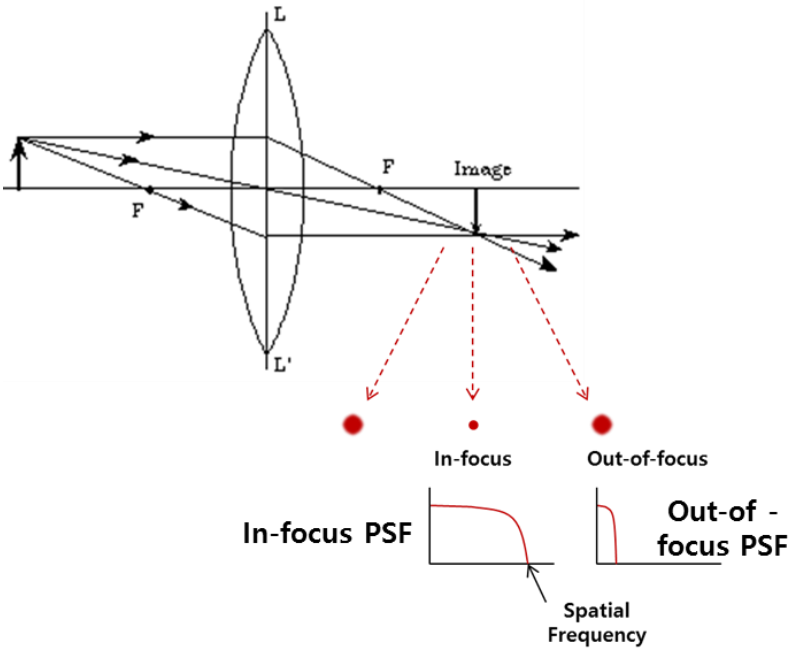

Figure 2.3 Diagram of in-focus and out-of-focus

For this reason, various methods for removing the background have been suggested, such as LSCM and structured illumination microscopy. The HiLo technique applied in this study is also one of the methods to improve optical resolution through background rejection.

2.2. Mathematical background for HiLo technique

Uniform- and structured illumination image

The images obtained from a microscope are the results of simultaneous measurement of in-focus and out-of-focus image components as described in Chapter 2.1. This can be expressed as the sum of the two components as in Eq. (2.2) and can also be visualized in the frequency domain as in Figure 2.4. It is shown that the high spatial frequency region contains only the in-focus signal, while the low spatial frequency region includes both the out-of-focus signal and the in-focus signal. If only the in-focus signal can be obtained by selectively removing only the out-of-focus signal, optical resolution can be improved.

$$I_u(x) = I_{in}(x) + I_{out}(x) \tag{2.2}$$

where, $I_{in}(x)$: the in-focus signal, and

$I_{out}(x)$: the out-of-focus signal.

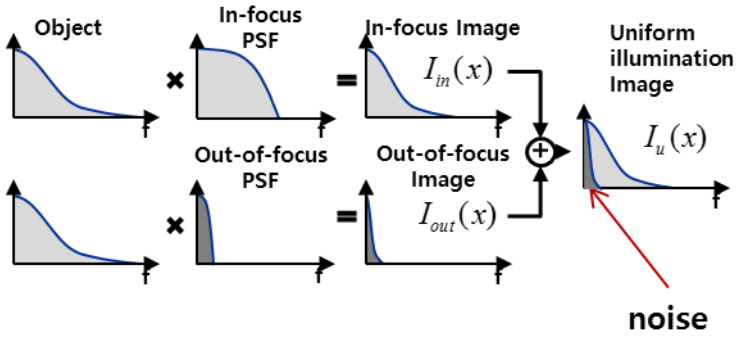

Figure 2.4 Diagram of the uniform illumination image in the Fourier domain

HiLo technique removes out-of-focus signal by obtaining a structured illumination image by entering a light source passing through a separate grating pattern, and then processing it with a uniform illumination image.

When a light source is passed through a grating filter of a stripe structure, a structured light source is created and a sinusoidal pattern is imaged on the surface of the specimen as the light passes through the lens. A structured illumination image is an image of a specimen illuminated by this structured light.

Structured illumination image is a convolution image of the signal whose image information is shifted by the grid and the original signal of specimen. This is in Figure 2.5 and can be expressed as Eq. (2.3). Here, the structural contrast produced by the grid pattern can be expressed as a sinusoidal function, and κ_g represents the grating spatial frequency of the structural contrast on the specimen surface. In Eq. (2.3), the out-of-focus component is composed of lower frequency components than the grating spatial frequency as shown in Figure 2.5. Out-of-focus images are not expressed as the mathematical term with a product of sine function since the grating image is not projected on the out-of-focus plane [22]

$$I_s(x) = I_{in}(x)[1 + M\sin(\kappa_g x)] + I_{out}(x)\,, \tag{2.3}$$

where, $\kappa_g = 2\pi / p$: the spatial frequency of grating,

p : the illuminated grating period

M : the grating modulation depth $M = (I_{\max} - I_{\min}) / (I_{\max} + I_{\min})$,

Sign function : the mathematical model for the illuminated grating pattern.

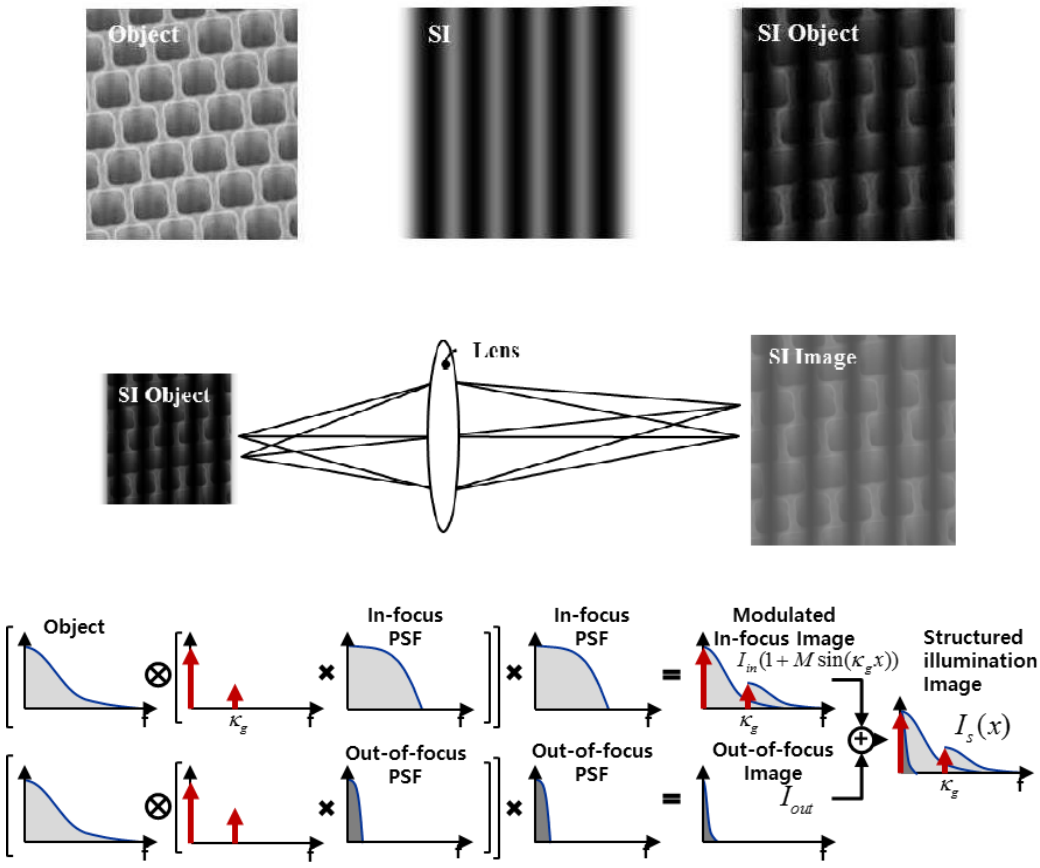

Figure 2.5 Structured illumination image and diagram in the Fourier domain

In order to obtain the two images required for HiLo technique, a movable grating filter is placed in the optical path of a general microscopy, and a uniform illumination image and a structured illumination image are sequentially acquired while moving the grating filter. Specifically, as shown in Figure 2.6, a structured light source is created by disposing a grating filter having a uniform interval in the incident light path of a microscope. The generated structured light is projected on the specimen, and the reflected light reflected from the specimen is photographed with a camera to obtain a structured illumination

image. Thereafter, the grating filter is removed to obtain a uniform light, which is then illuminated on the specimen to obtain a uniform image.

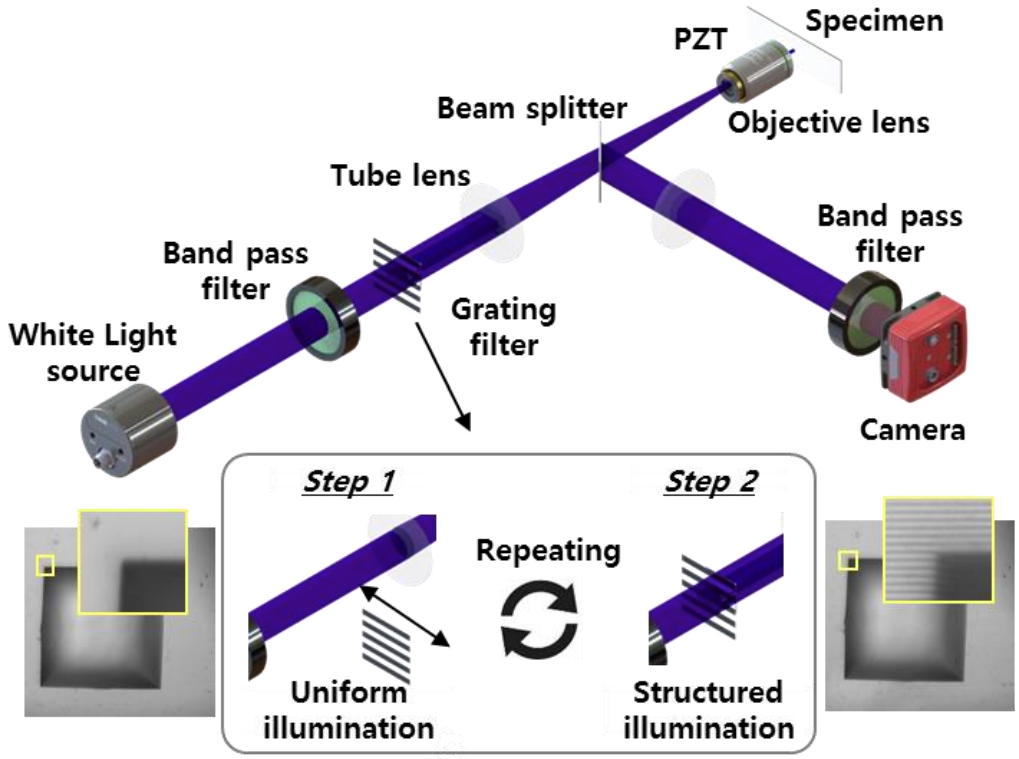

Figure 2.6 Concept diagram of HiLo technique. Structured illumination image and uniform illumination image are taken sequentially by moving the grating filter.

Mathematical processing with uniform- and structured illumination image

Let us define $D(x)$ as the difference between $I_u(x)$ and $I_s(x)$ in Eq. (2.4) and Eq. (2.3). As shown in Eq. (2.5), $I_{out}(x)$ is removed and $D(x)$ is expressed only with $I_{in}(x)$ component. However, since the sinusoidal element is included in the grating filter, additional calculation is required to obtain a pure $I_{in}(x)$ component.

$$D(x) = \left| I_s(x) - I_u(x) \right| = \left| M \sin(\kappa_g x) I_{in}(x) \right| \tag{2.5}$$

Here, the full rectified sine wave $\left| M \sin(\kappa_g x) I_{in} \right|$ can be expanded in Fourier cosine series.

$$\begin{aligned} \left| M \sin(k_g x) \right| &= \frac{2M}{\pi} - \sum_{n=1}^{\infty} \frac{4M}{\pi} \frac{\cos(2nk_g x)}{4n^2 - 1} \\ &= \frac{2M}{\pi} - \frac{4M \cos(2k_g x)}{15} - \ldots \end{aligned} \tag{2.6}$$

If both sides of Eq. (2.6) are Fourier transformed, Eq. (2.7) is driven.

$$FT(I_{in} \left| M \sin(\kappa_g x) \right|) = FT(I_{in}) \otimes FT\left(\frac{2M}{\pi} - \frac{4M \cos(2\kappa_g x)}{15} - \ldots \right) \tag{2.7}$$

Since

$$FT\left(\frac{2M}{\pi} - \frac{4M \cos(2k_g x)}{15} - \ldots \right) = FT\left(\frac{2M}{\pi} \right) - \frac{4M}{15} \left(\delta(\omega - \frac{\kappa_g}{\pi}) + \delta(\omega + \frac{\kappa_g}{\pi}) \right) - \ldots$$

If we assign it to Eq. (2.7) and calculate, $D(x)$ can be expressed as Eq. (2.8)

$$
\begin{aligned}
&FT(I_{in}\left|M\sin(\kappa_g x)\right|)\\
&= FT(I_{in}) \otimes FT\left(\frac{2M}{\pi} - \frac{4M\cos(2\kappa_g x)}{15} - \ldots\right)\\
&= \frac{2M}{\pi}FT(I_{in}) - \frac{4M}{15}\frac{1}{2}\left(FT(I_{in})\otimes\delta(\omega-\frac{\kappa_g}{\pi}) + FT(I_{in})\otimes\delta(\omega+\frac{\kappa_g}{\pi})\right) - \ldots\\
&= \frac{2M}{\pi}FT(I_{in}) - \frac{2M}{15}FT\left(I_{in}(x+\frac{\kappa_g}{\pi})\right) + \frac{4M}{15}FT\left(I_{in}(x-\frac{\kappa_g}{\pi})\right) - \ldots
\end{aligned}
$$

$$
\therefore D(x) = \left|I_s(x) - I_u(x)\right| = \frac{2M}{\pi}I_{in} - \frac{4M}{15}\left(I_{in}(x+\frac{\kappa_g}{\pi})\right) + \frac{4M}{15}\left(I_{in}(x-\frac{\kappa_g}{\pi})\right) - \ldots \qquad (2.8)
$$

As shown in Figure 2.7, the background component is removed from $D(x)$ and $D(x)$ has only the in-focus component, but it includes the component shifted κ_g/π by the grating pattern in the high-frequency region

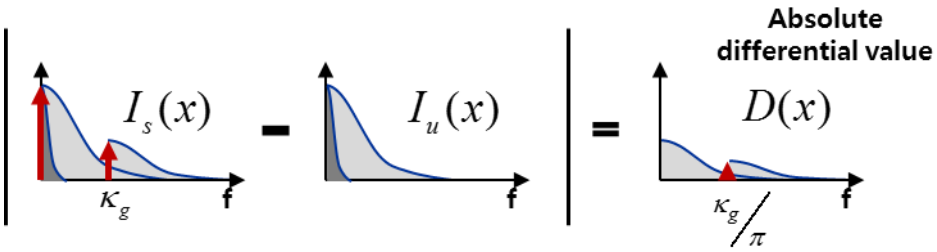

Figure 2.7 Differential image of structured image and uniform image

However, since the low frequency region of $D(x)$ includes only the in-focus signal from which the background is removed, it is possible to acquire only the low frequency in-focal image $I_{Low}(x)$ using a low-pass filter. Here, the cut-off frequency of the low pass filter

should be sufficiently smaller than κ_g / π . In actual operation, it is appropriately determined at half or one-third to one-half level of κ_g / π .

$$I_{Low}(x) = LP_{\kappa}(I_{in}(x)) = \frac{\pi}{2M} LP_{\kappa}(|I_s(x) - I_u(x)|) \tag{2.9}$$

The high frequency in-focal image can be obtained separately by applying a high pass filter to the uniform illumination image.

$$I_{high}(x) = HP_{\kappa}(I_u(x)) \tag{2.10}$$

When Hi image and Lo images thus obtained are multiplied by an appropriate weighting factor η capable of matching the intensity profile between the two images and summated, the complete in-focus image signal $I_{HiLo}(x)$ can be finally obtained as below.

$$I_{HiLo}(x) = I_{high}(x) + \eta I_{low}(x) \tag{2.11}$$

For a more intuitive understanding, the principle of HiLo imaging method is visualized in the Fourier domain in Figure 2.8 and an example of a HiLo image implemented using the real uniform image and the structural image is shown in Figure 2.9. As a result of removing the out-of-focus component through HiLo technique, it is confirmed that a clearer image can be obtained compared with a uniform illumination image

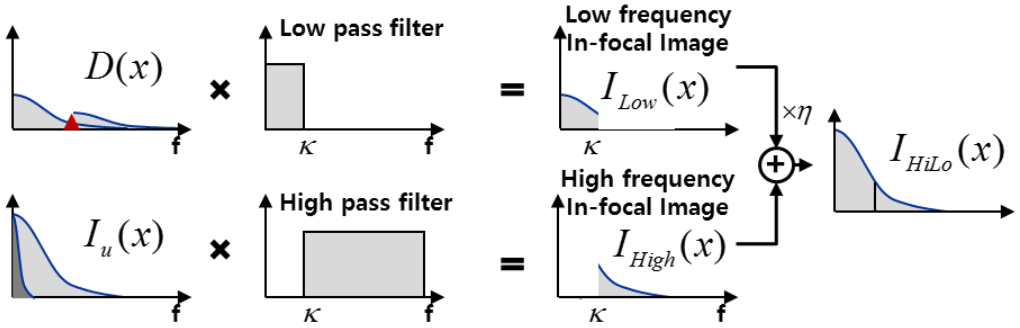

Figure 2.8 HiLo image composition with low frequency image and high frequency image

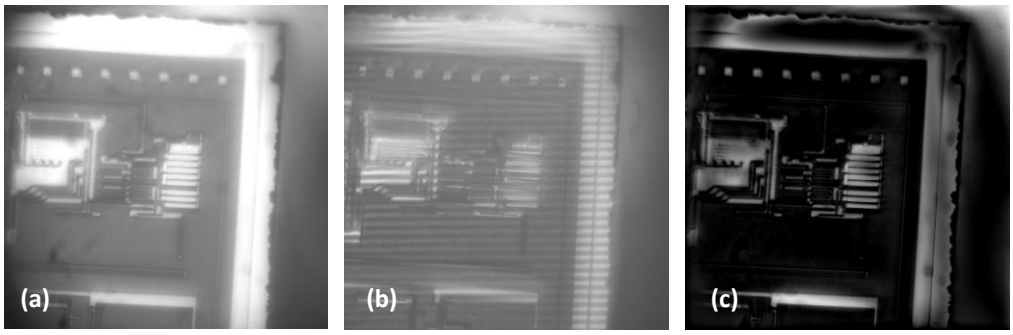

Figure 2.9 Result of HiLo imaging; (a) uniform illumination image, (b) structured illumination image, (c) HiLo image

Lateral resolution enhancement by HiLo technique

Theoretically, improved lateral resolution is synonymous with the expression of a larger spatial frequency component in the frequency domain. To do this, we use a technique of using incident light with a shorter wavelength, or synthesizing a number of images such as SIM to enlarge the OTF.

However, in the case of HiLo image, the high frequency domain component is utilized by high pass filtering the uniform image, so it is not related to the expansion of the high frequency domain. In other words, theoretically, the lateral resolution of HiLo image is obviously not improved. However, by removing the background signal in the same way as the LSCM, it is possible to acquire an image that does not include the blurred signal of the out-of-focus signal. This makes it possible to more clearly recognize the edge region of the specimen having a height step.

Effect of spatial frequency of grating on axial resolution

In general microscopy, the brightest and clearest images can be obtained when the surface of the specimen exactly matches the focal plane of the microscope. However, if the surface of the sample does not match the focus of the microscope, the intensity of the acquired image decreases and the image becomes blurred. In other words, the surface height of the specimen can be recognized by comparing the intensities of the measured images at the focal plane and the out-of-focus position, and finding the brightest spot. However, in a general WFM, the out-of-focus signal has a certain level of brightness irrespective of the reflected light from the surface. Therefore, it acts as a noise factor in the height recognition process using brightness difference. On the other hand, as HiLo technique removes the out-of-focus signal, it can recognize only the reflected light from the surface, which makes it advantageous for height profile measurement.

The axial resolution of HiLo technique can be interpreted by an optical sectioning technique using a grating. This applies equally to all cases using structured illumination such as SIM. Optical sectioning through structured light with a grating was proposed by

Neil (1997) [22] and Mertz (2011) [14]. Intensity at a specific point *(x, y)* in the measured microscope image is expressed by integrating the product of the shape *s(x, y)* of the specimen and the point spread function (PSF) *H(x, y)* of the optical system [23] as Eq. (2.12).

$$I(t,w) = \int\int s(t_1, w_1) H(t_1 + t, w_1 + w) dt_1 dw_1 \tag{2.12}$$

where, $t = \frac{2\pi}{\lambda} xNA$,

$w = \frac{2\pi}{\lambda} yNA$, and

λ : wavelength of the illuminated light.

Since the light incident through the objective lens is photographed on the camera through the same objective lens, the pupil function of the incidence and the reflection are the same and thus expressed as Eq. (2.13).

$$H(t,w) = \left| h_2(t,w) \right|^2, \tag{2.13}$$

$$h(v) = \int P(\rho) J_0(v\rho) \rho d\rho, \tag{2.14}$$

where, $v = \sqrt{t^2 + w^2}$,

$J_0(\,)$: zero-order Bessel function of the first kind, and

$P(\rho)$: pupil function of defocus.

However, the pupil function exists in various forms corresponding to individual microscopic methods, and it is difficult to calculate strict mathematical induction.

Therefore, in the case of structured illumination using the grating, the OTF model experimentally presented by Stokseth (1964) [24] is generally used. In case of reflected light measurement, modified Stokseth OTF model by Neil (1997) [22] is applied.

When measuring the reflected light of the surface, the intensity variation *g* is expressed as a function of normalized grid spatial frequency $\tilde{\nu}$ and normalized axial movement *u* by the Stokseth OTF model as shown in Eq. (2.15) [18] [22].

$$I_p(u,\tilde{\nu}) = \left|g(2u,\tilde{\nu})\right| = \left| f(\tilde{\nu}) \left\{ 2\frac{J_1[2u\tilde{\nu}(1-\tilde{\nu}/2)]}{2u\tilde{\nu}(1-\tilde{\nu}/2)} \right\} \right|, \tag{2.15}$$

where, $u = \frac{8\pi}{\lambda} z \sin^2(\frac{\alpha}{2})$,

$\tilde{\nu} = \frac{\lambda \nu}{NA} = \frac{\lambda}{NA}\frac{2\pi}{p}$,

$f(\tilde{\nu}) = 1 - 0.69\tilde{\nu} + 0.0076\tilde{\nu}^2 + 0.043\tilde{\nu}^3$,

J_1 : Bessel function of the first kind,

α : half the angular aperture of the objective lens, and

p : the illuminated grid period.

The Eq. (2.15) is visualized in Figure 2.10. The intensity decreases as the focus movement u increases or decreases with respect to the focal plane ($u = 0$). In this case, the closer $\tilde{\nu}$ is to 1, the better the axial response and the axial response is best when $\tilde{\nu} = 1$. If $\tilde{\nu}$ is greater than 1, both the axial response and the intensity are reduced. Therefore, considering the signal-to-noise ratio (SNR) in the experiment, it would be reasonable to set the $\tilde{\nu}$ value to less than 1.

Axial resolution can be expressed as full width at half maximum (FWHM), and it can be calculated as the *u* value when the intensity in Eq. (2.15) is 50% of the peak intensity. Since the $f(\tilde{\nu})$ affects only the magnitude of the intensity in the OTF, in the FWHM calculation it is necessary to find the *u* value when the value is 0.5 in the normalized intensity profile excluding $f(\tilde{\nu})$ as shown in Figure 2.11 [25][26].

$$2\frac{J_1[2u_{FWHM}\tilde{\nu}(1-\tilde{\nu}/2)]}{2u_{FWHM}\tilde{\nu}(1-\tilde{\nu}/2)}=\frac{1}{2} \tag{2.16}$$

$$J_1[2u_{FWHM}\tilde{\nu}(1-\tilde{\nu}/2)]=u_{FWHM}\tilde{\nu}(1-\tilde{\nu}/2)$$

$$2u_{FWHM}\tilde{\nu}(1-\tilde{\nu}/2)-(u_{FWHM}\tilde{\nu}(1-\tilde{\nu}/2))^3+\frac{1}{6}(u_{FWHM}\tilde{\nu}(1-\tilde{\nu}/2))^5-\ldots=u_{FWHM}\tilde{\nu}(1-\tilde{\nu}/2)$$

$$1-\left(u_{FWHM}\tilde{\nu}(1-\tilde{\nu}/2)\right)^2+\frac{1}{6}\left(u_{FWHM}\tilde{\nu}(1-\tilde{\nu}/2)\right)^4-\ldots=0$$

$$u_{FWHM}\approx\frac{1}{\tilde{\nu}(1-\tilde{\nu}/2)} \tag{2.17}$$

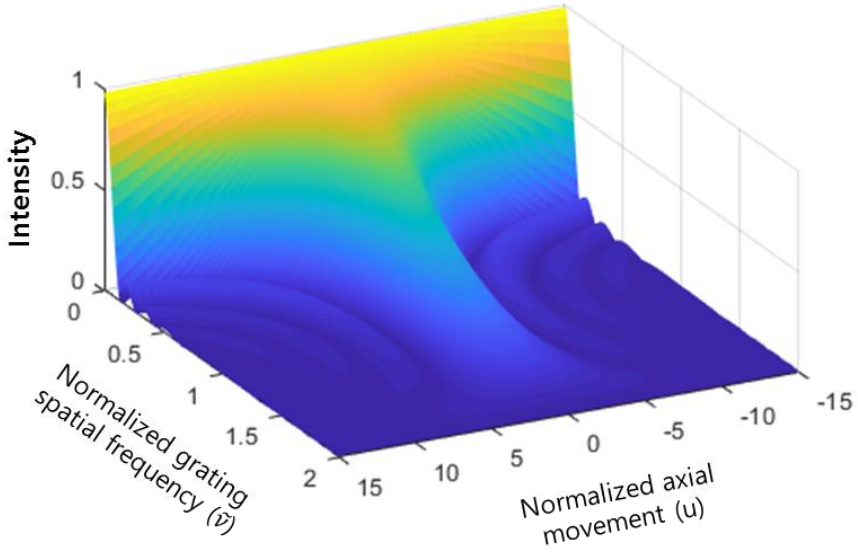

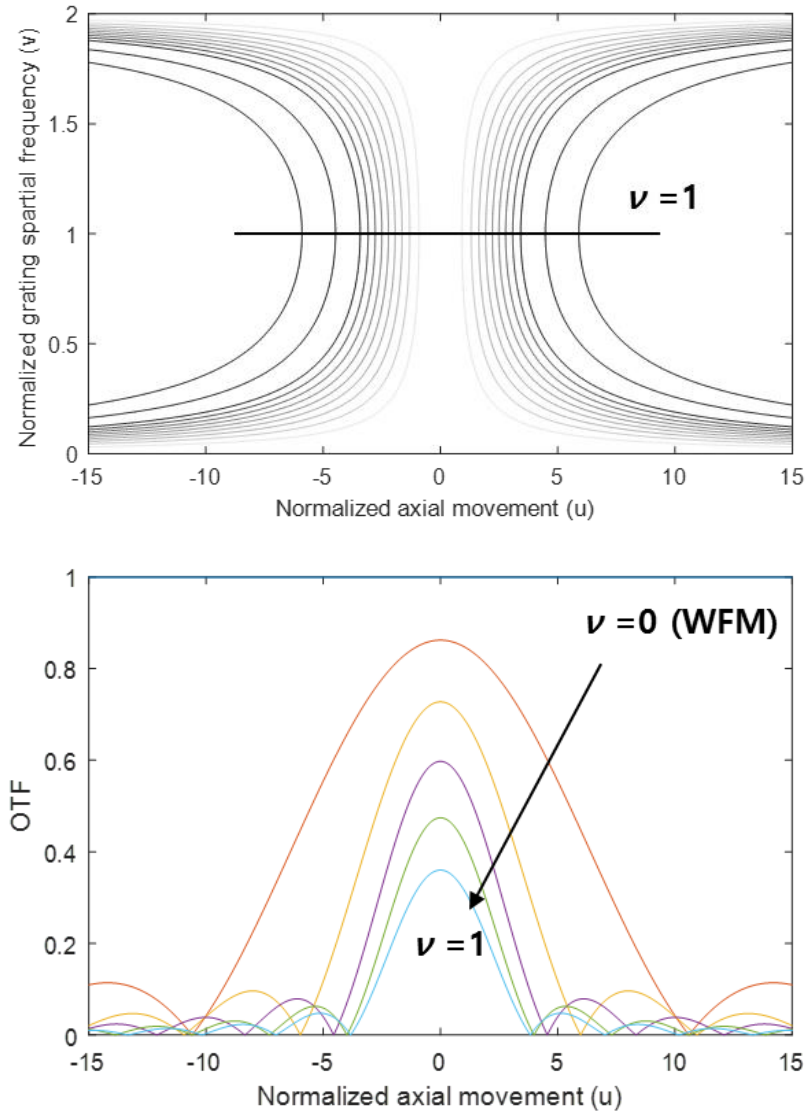

Figure 2.10 Stokseth OTF model for optical sectioning using grid pattern

When Eq. (2.17) is denoted p, λ, NA and the refractive index of the optical medium n, Eq. (2.18) can be derived.

$$\delta = \frac{\lambda / 2}{\sqrt{n^2 - \left(NA - \frac{\lambda}{p}\right)^2} - \sqrt{n^2 - NA^2}} \tag{2.18}$$

$$\delta_{\min} = \frac{\lambda / 2}{n - \sqrt{n^2 - NA^2}}, \quad \text{at} \quad p = \frac{\lambda}{NA} \tag{2.19}$$

It shows that the axial resolution, *i.e.* the minimum distance δ for distinguishing the intensity difference between axial positions, can be derived, and is at the minimum when the grating period is twice the cutoff frequency, by the Abbe limit, as shown in Eq. (2.19) [27][28].

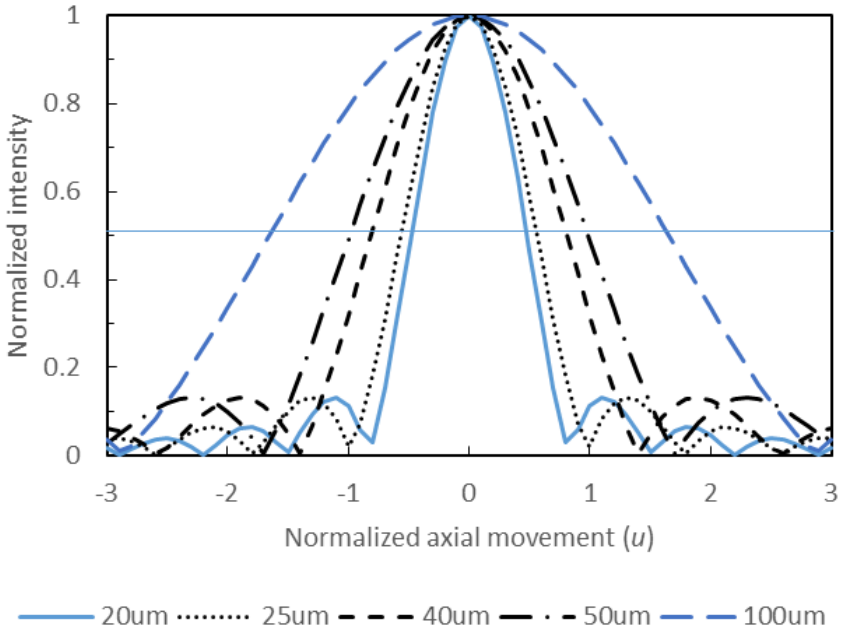

Figure 2.11 Normalized theoretical z-axis intensity variation of the optical sectioning using grating pattern

2.3. Optical configuration

The experimental setup was constructed according to the concept of HiLo imaging technique shown in Figure 2.6. The whole optical configuration and the core parts are described, and specifications such as FOV and camera pixel size of the constructed optical system were measured. The grating, which is a key performance parameter of HiLo technique, was described in more detail. And the grid spatial frequency of the incident light passing through the grating on the surface of the specimen was measured.

Optical system configuration and optical component description

As shown in Figure 2.12, an optical device for applying HiLo imaging technique was constructed. The body part of the Olympus BX41 model, which is a commercial upright optical microscope, was used as it is, and optical components, *i.e.* a light source, grating filter, tube lens, piezo positioner, and camera, were placed over the body.

The light source was a mercury arc lamp, a white light sources generally used in fluorescence microscopy. However, when using a white light source where various wavelengths are mixed, it is difficult to separate the characteristics of HiLo technique because of the aberration caused by the difference of the lens refractive index depending on the wavelength. Therefore, it is necessary to selectively use only the wavelength of a specific frequency by using a band-pass filter. In order to utilize the short wavelength band between 400 *nm* and 450 *nm*, which has superior optical resolution, the mercury arc lamp has a band pass filter which selectively passes only 440 *nm* considering that the spectral intensity peaks at 436 *nm* wavelength.

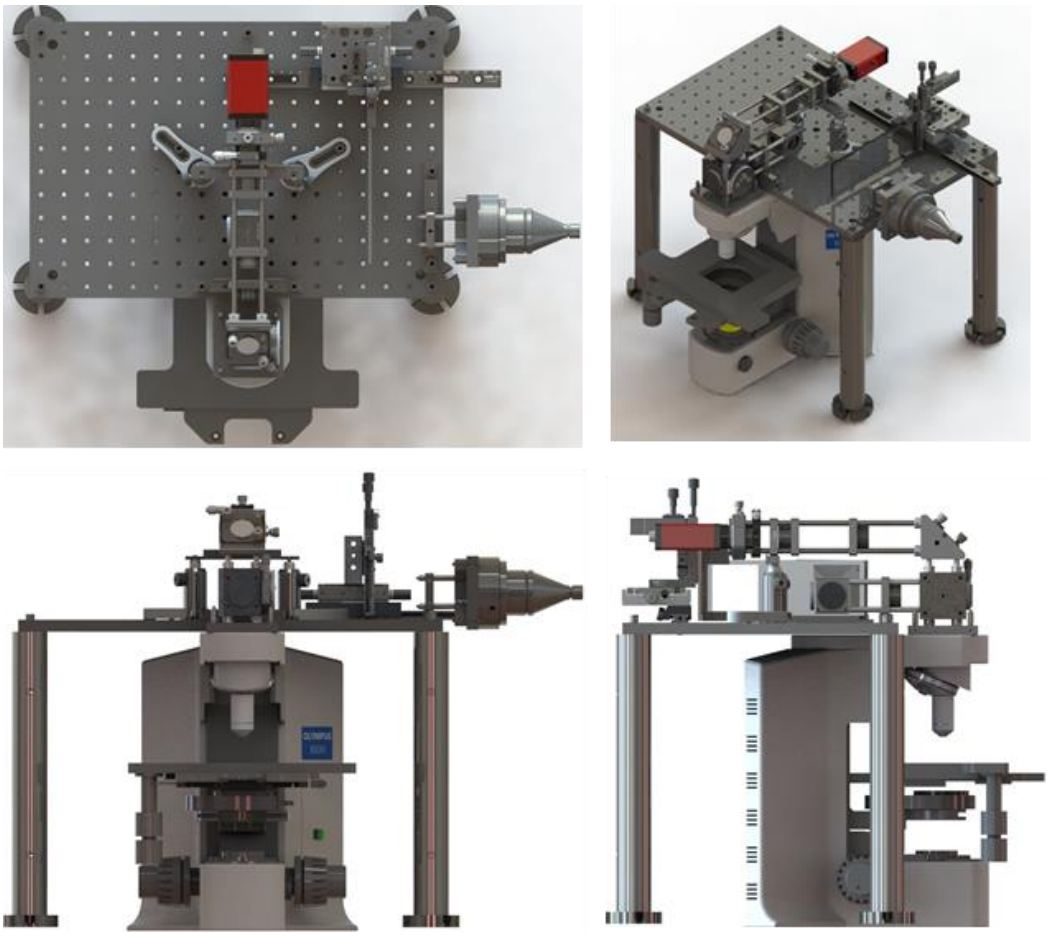

Figure 2.12 Optical Configuration of HiLo imaging technique

A grating filter was placed in the optical path of incident light to enable structured illumination. The structured illumination is constructed by locating the customized grating on the image-conjugate plane so that the image of the grating is formed on the focal plane of the objective lens, whereas the uniform illumination is produced without the grating. A translation stage is placed to move the grating filter up and down so that uniform illumination and structured illumination can be sequentially performed. The grating filter

was customized by coating a chromatic mask on a glass plate, and four kinds of grating filters, 50, 40, 25 and 20 line pairs / mm (lp/mm), were made to find the optimum grid period.

Olympus MPlanApo N 50×, *NA* = 0.95, 50×, apochromatic lens, was mainly used as objective lens. Olympus Ach 40x, *NA* = 0.65, 40×, achromatic lens, was also used in parallel. Tube lens and imaging lens were set to focal lengths of 200 mm (LA1708, Thorlabs, Inc.) and 150 mm (LA1433, Thorlabs, Inc.), respectively, considering the sensor size, pixel size, and number of pixels of the camera, and the camera and optical components were arranged according to the focal distance

A beam splitter (50:50, CCM1-BS013, Thorlabs, Inc.) was placed in front of the objective lens instead of a dichroic mirror. It is taken into account that the dichroic mirror which is commonly used in a microscope cannot be used for reflected light measurement in which the frequencies of incident light and reflected light are the same.

In consideration of the mechanical limitations, the reflective mirror and beam splitter were selected as thin plate type. Most of the optical element parts were selected from stock items. Custom-made optical components were used where space limitations exist.

As for the camera, G-145-B gigabit Ethernet model of Allied Vision Technology was selected. The camera has an image sensor of 2/3 inch, 1388×1038 pixels and can acquire up to 30 frames per second of 8bit or 12bit mono images.

For the 3D measurement, the focal plane is moved by moving the objective lens in the axial direction so that continuous imaging can be performed. Piezo positioner (PZT) was directly connected to the objective lens for z-axis movement. The adopted Piezo positioner is P725-4CD model of PI GmbH., which can move with a position error less

than 1.25 nm within the range of 0 ~ 400 μm for closed loop control. It has an USB communication port for external control, and is connected to the device through the USB communication port of the PC and controlled by our custom-made software.

Major optical components used in the optical configuration are summarized in Table 1.

Table 1 Core component list of the optical configuration

Parts	**Maker / Name**	**Specification**
White Light Source	Excelitas tech. / X-cite 120PC Q	Mercury Arc. Lamp, 120W (peak at 405 *nm*, 436 *nm*)
Band pass filter	Thorlabs / FB440-10	440 *nm*, FWHM 10 *nm*
Tube lens	Thorlabs / LA1708	f = 200 mm, uncoated
Imaging lens	Thorlabs / LA1433	f = 150 mm, uncoated
Objective lens	Olympus / MPlanApo N 50x Olympus / Ach 40x	50×, NA = 0.95 40×, NA = 0.65
Piezo positioner	PI / E-709 (Controller) PI / P-725 4CD (Positioner)	Travel range ~400 μm (at closed loop) Resolution 1.25 *nm* (at closed loop)
Beam splitter	Thorlabs / CCM1-BS013	50:50, non-polarizing
Camera	Allied Vision Tech / manta-G145b	1388×1038, 30 fps, 8bit or 12bit mono

Specification of the optical system

To determine the basic specification of the optical configuration, we measured the field of view (FOV) and image size per camera pixel. The Ronchi-ruler with 400 lp/mm, or 2.5 μm gaps, was shoot as the specimen as shown in Figure 2.13 and the results were calculated. The measurements were made with 50× and 40× objective lens, and the FOV was 178 μm × 133 μm and 224 μm × 167 μm, respectively, and the pixel size of the camera was 0.128 μm and 0.161 μm, respectively; see Table 2.

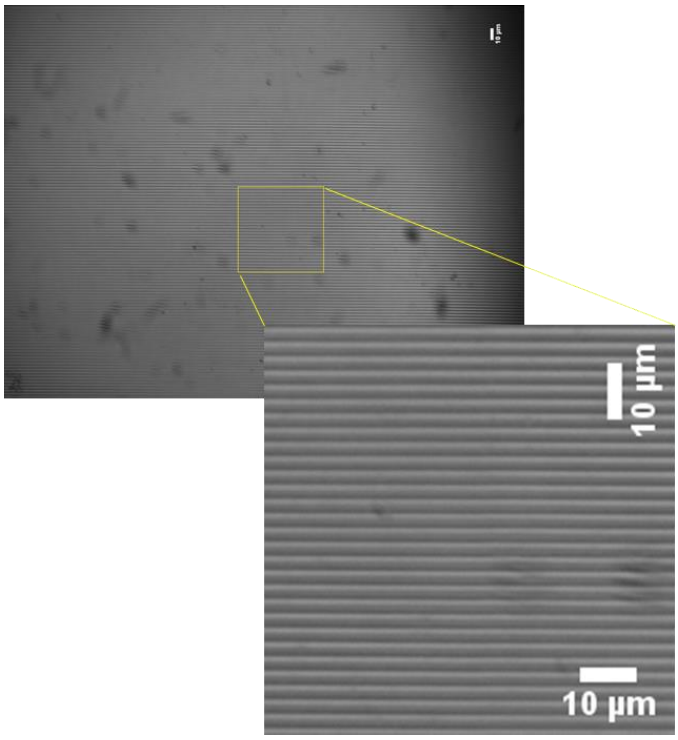

Figure 2.13 Ronchi-ruling image for getting CCD imaging area; grid period: 400 lp/mm (2.5 μm/line)

Table 2. FOV and pixel size of the optical system

Objective lens	Field of view (μm)	No. of pixels	Pixel size (μm)
50×	177.7 × 132.9	1388 × 1038	0.128
40×	223.8 × 167.4	1388 × 1038	0.161

The grating design

As shown in Eq. (2.18), axial resolution in HiLo technique is affected by wavelength of light, *NA* of objective lens, and grating spatial frequency. However, the wavelength depends on the type of light source and is difficult to change, and the objective lens needs to be changed from time to time according to the size of the specimen to be measured. For such reasons, it is necessary to select the grating spatial frequency corresponding to the optimum value according to the objective lens, and then to match the optimal grating spatial frequency for each objective lens in the specimen measurement. In order to find the optimum, four gratings with different spatial frequencies of 20, 25, 40, and 50 lp/mm were fabricated on the glass plate with a chrome mask pattern.

Figure 2.14 is an example image of the light source which passes through each pattern and is expressed in the actual measurement sample. It can be seen that, due to diffraction, the light source passing through each grating filter is represented as a form of sinusoidal function. Table 3 shows the number of camera pixels and grid period per grating period measured with two types of objective lenses, 50× *NA* = 0.95 and 40× *NA* = 0.65.

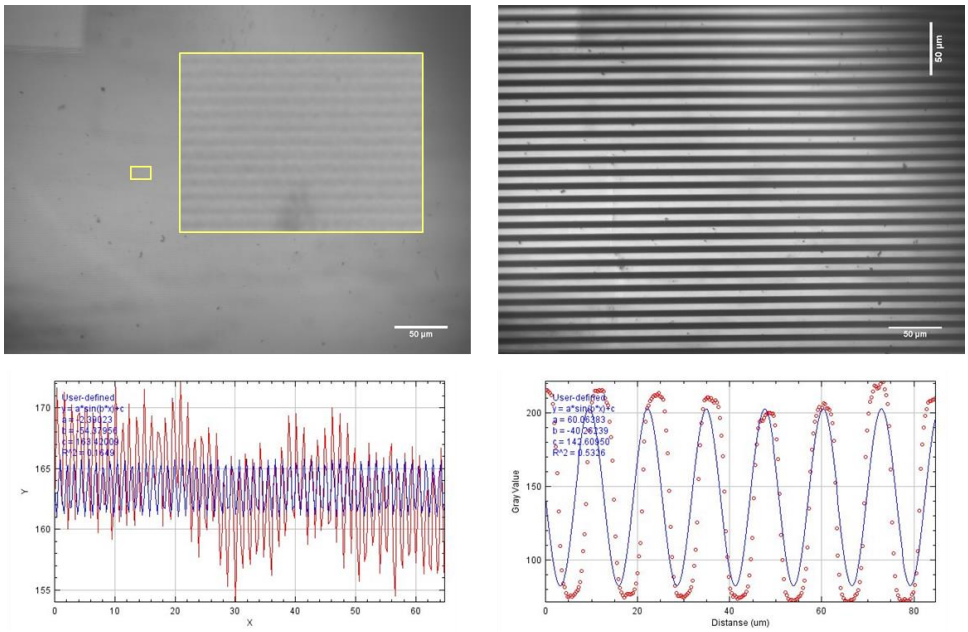

Figure 2.14 Illumination pattern through 20 μm (left), 100 μm grid filter (right); and illuminated grid by pattern filter (original (red) and curve fitted (blue))

Table 3. The illuminated grating period on a specimen surface of the light passed through the grating at the 40× and the 50× objective lens

Grating pattern period	**Illuminated grating period on sample surface**			
	50×, *NA* = 0.95		40×, *NA* = 0.65	
	No. of camera pixels	Illuminated grid period (μm)	No. of camera pixels	Illuminated grid period (μm)
20 μm (50 lp/mm)	3.9	0.50	3.7	0.60
25 μm (40 lp/mm)	4.8	0.61	4.6	0.74
40 μm (25 lp/mm)	7.7	0.99	7.1	1.14
50 μm (20 lp/mm)	9.6	1.23	8.9	1.42

2.4. Software configuration

A software was created to implement HiLo imaging technique using the acquired uniform- and structured illumination images. In the following sections, we described HiLo image processing algorithm and then described the overall process and configuration for actual image acquisition and processing.

HiLo image processing algorithm

Figure 2.15 shows HiLo algorithm in a block diagram form. First, the grating spatial frequency κ_g is calculated through the selected grating period, and a high pass filter with a cut off frequency of $\kappa_g / 3$ is applied to the uniform illumination image to obtain a high frequency image $I_{Hi}(x)$. Separately, $D(x)$ was obtained by subtracting the structured illumination image and the uniform illumination image and taking the absolute values. Then $I_{Low}(x)$ was obtained by applying a low pass filter at the same cut off frequency as the high pass filter. Then the Hi and Lo images are added to realize HiLo image. Here, the scale factor for reproducing the contrast of HiLo image was appropriately set between 1 and 5.

In the software code, the operation was sequentially performed according to the block diagram shown in Figure 2.15 and the formula given in Chapter 2.2. The process is shown briefly in Table 4.

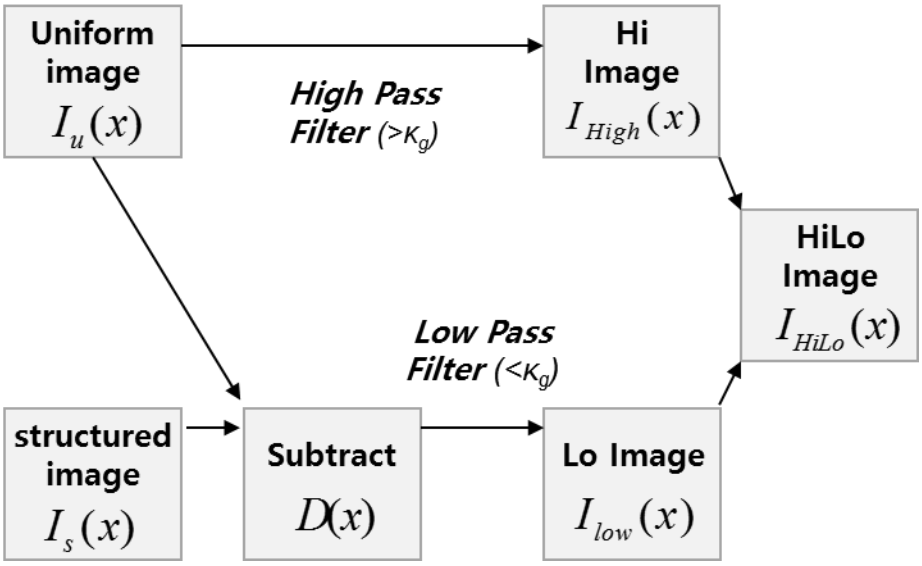

Figure 2.15 HiLo principle block diagram; (modified from the picture of Boston University Lab. Website, http://biomicroscopy.bu.edu/research/hilo-microscopy)

Table 4. HiLo algorithm implementation

No.	Process
1	Read image slices - Uniform illumination image : $I_u(x)$ - Structured illumination image slice : $I_s(x)$
2	Calculate grid spatial frequency ($2\pi / p$)
3	Obtain $I_{High}(x)$ by applying High-Pass Filter (> κ_g) to $I_u(x)$
4	Normalize image contrast by mean value of image
5	Calculate absolute difference value ($D(x)$)
7	Obtain $I_{Low}(x)$ by applying low Pass Filter (< κ_g) to $D(x)$
8	Acquire $I_{HiLo}(x)$ by composing $I_{Low}(x)$ and $I_{High}(x)$
9	Save source images and HiLo image

Overall software configuration

Figure 2.16 shows the complete software diagram for HiLo imaging and 3D reconstruction. It consists of 6 stages as follows.

1. Obtain uniform illumination image and structured illumination image by moving grating filter
2. Implement HiLo algorithm with two images (Acquire I_{HiLo})
3. Store two source images and I_{HiLo} image
4. Make image stack of I_{HiLo} with focus movement using PZT
5. Align the image stack in axial direction
6. 3D reconstruction and visualization

Steps 5 and 6 are 3D reconstruction of the surface profile and described in more detail in Chapter 4.

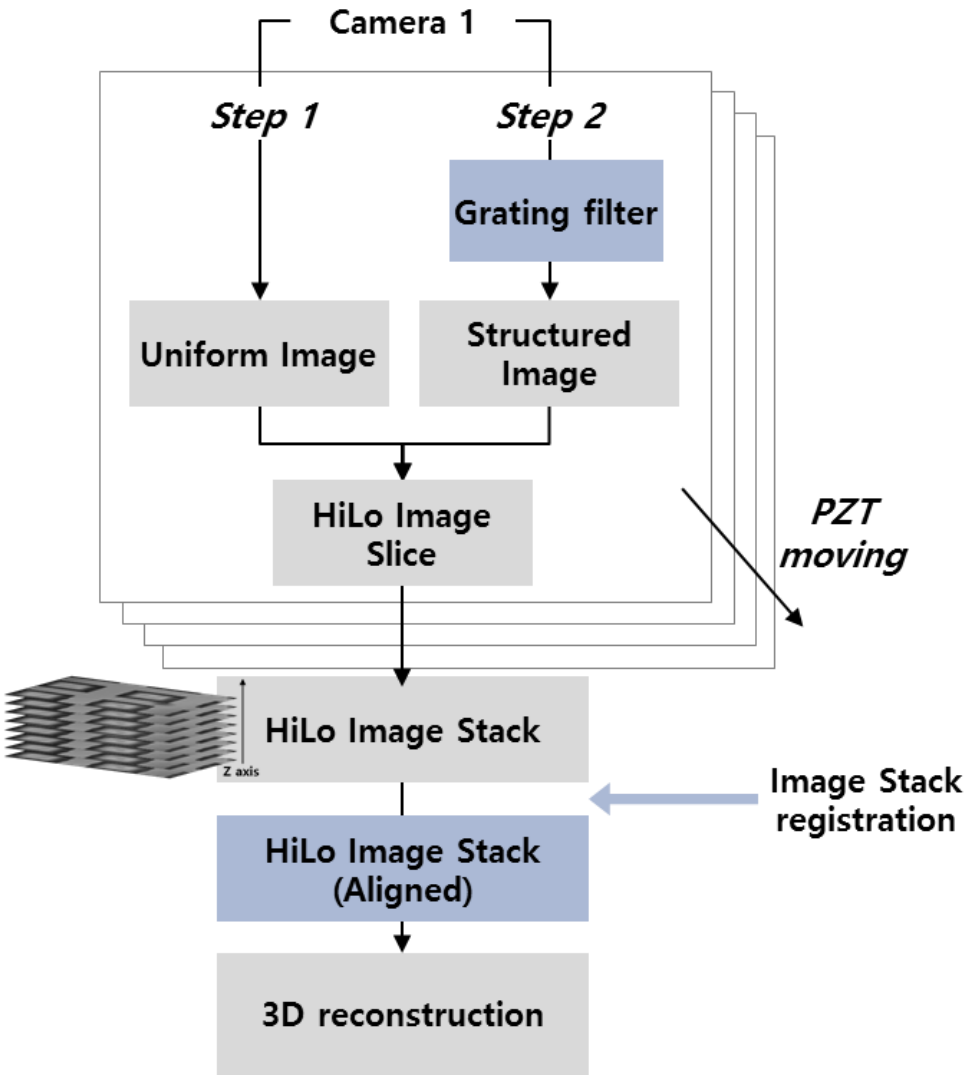

Figure 2.16 Overall process of 3D surface measurement with HiLo technique

In order to acquire an actual HiLo image, it was necessary to implement separate functions such as hardware control of camera, PZT and grating fiber, image acquisition, image registration, saving and other functions, and to develop a software that integrate all the functions as well as to apply HiLo algorithm.

The integrated software was built using Microsoft Visual C # as the basic framework (Figure 2.17). In the process, we actively utilized software development kit (SDK) and open source library provided by each hardware manufacturer.

The camera image acquisition was included in the custom-made software using the VIMBA 2.3 library, which is a free software development kit (SDK) from the manufacturer. However, single-time variables such as camera exposure, gain, and operation mode were set by the Vimba viewer software separately provided by the manufacturer.

HiLo processing algorithm was implemented by using ImageJ [29], a representative image-based research software, and then transferred to custom-made software. For HiLo algorithm, we referred to the HiLo plugin of ImageJ [30] from the website of Biomicroscopy Lab at Boston University, which first introduced HiLo technique and the source code provided by Professor Jerome Mertz.

At each focal plane, the structured and uniform images are obtained with the two different illuminations by inserting and removing the grid sequentially, and HiLo image at given focal plane is processed using the two images. The 3D HiLo image stack is generated by accumulating depth-resolved HiLo images at different focal planes.

For the 3D reconstruction, which obtains the surface profile from the image stack, the algorithm that is applied to the focus variable and the shape from focus, etc., was also applied. This 3D reconstruction algorithm, described in Chapter 4, is first implemented using MATLAB and then ported to the custom-made software.

Open CV [31], a representative image processing open source library, was utilized in the process of transferring HiLo image processing and 3D reconstruction algorithms to the

custom-made software. Open CV provides functions necessary for image operations such as addition, filtering, and includes optimized codes for CPU and GPU characteristics. Therefore, it was considered more efficient to use Open CV than to write an individual operation code for each image point.

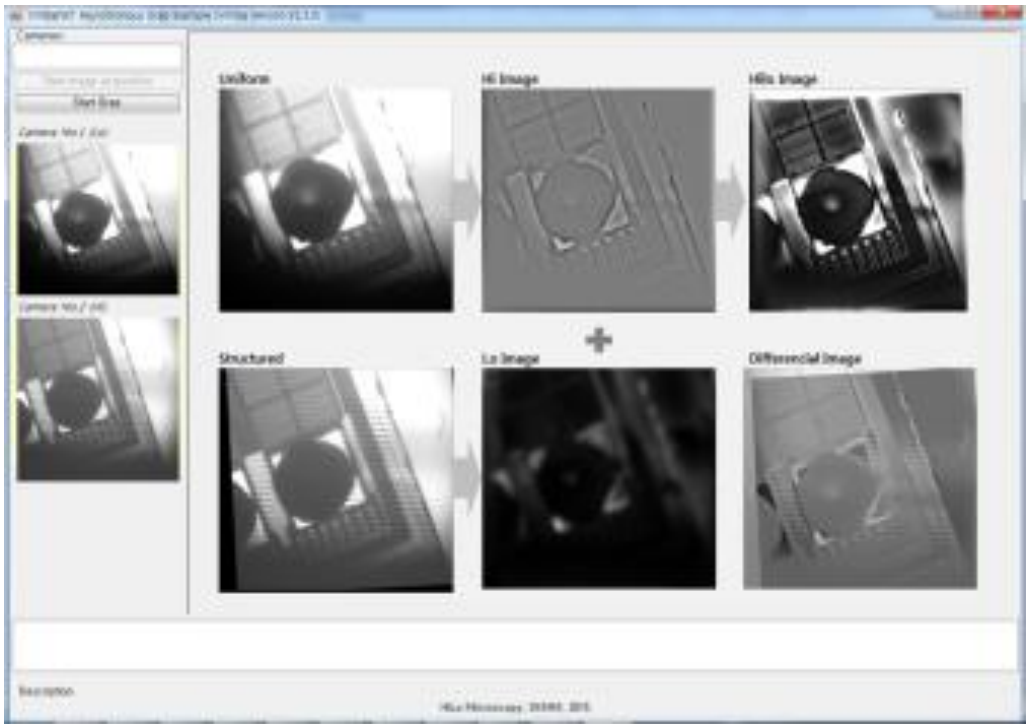

Figure 2.17 Screen shot of custom-made software

2.5. Optical resolution of HiLo imaging technique

To verify the performance of HiLo technique, lateral and axial resolutions were compared with those of WFM and LSCM.

Lateral resolution of HiLo technique

In order to evaluate the performance of HiLo technique for surface profile measurement, the lateral resolution is measured in 2D images.

The following three cases were selected for the comparison of microscope techniques.

Case 1) Commercial LSCM (LEXT OLS 5000, Olympus Corp., Japan)

Case 2) WFM image at illumination wavelength 440 *nm*

Case 3) HiLo image at 440 *nm* with several grating period

To compare performance of each case, USAF-1951 Target group 7 was measured. 50× *NA* = 0.95 objective lens was used for all cases. By operating the equipment in the darkroom, the disturbance caused by other light sources was blocked as much as possible.

As shown in Figure 2.18, the lateral resolution measured by WFM, HiLo and LSCM at the edge is 0.77 μm, 0.38 μm, and 0.25 μm, respectively. They are all larger than the theoretical diffraction limit (0.28 μm for both WFM and HiLo, and 0.17 μm for LSCM), but it is confirmed that the lateral resolution in HiLo is improved by 50% compared to that of WFM. The lateral resolution in LSCM is about 52% smaller than that of HiLo, but

it can be seen that it has a comparable lateral resolution, considering that the slopes of intensity profile in the boundary are similar to each other.

The lateral resolution is almost the same at the edge, regardless of different grating periods in HiLo. Rather, the smaller the grating period, the greater the noise around the edge. Therefore, when selecting the grating period, the grid period should be set to be larger than the minimum period indicated by Eq. (2.19).

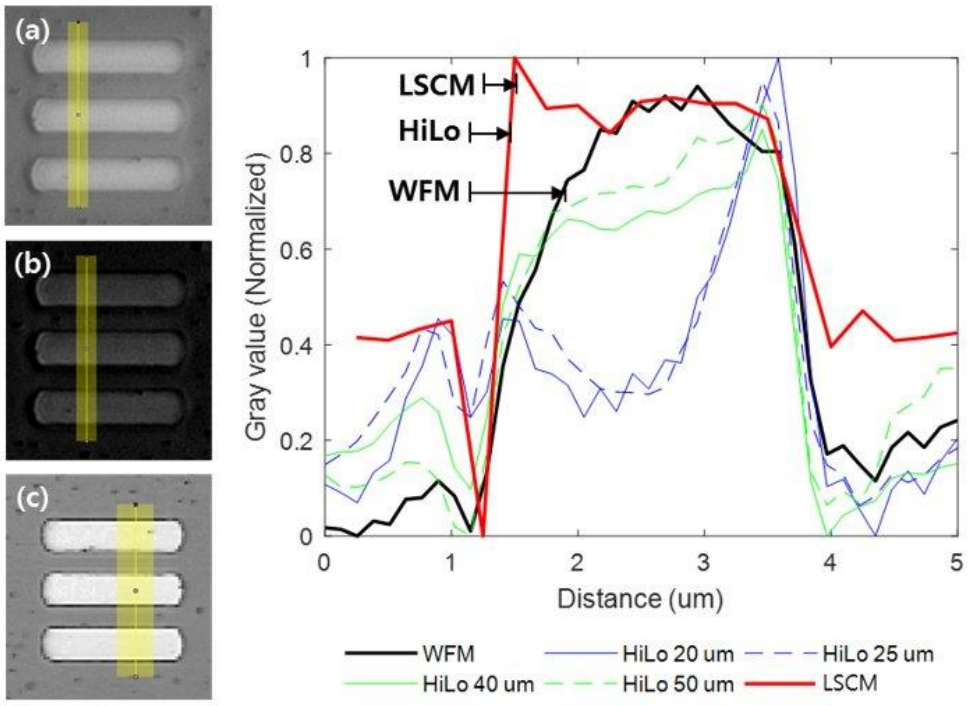

Figure 2.18 Lateral resolution comparison of (a) WFM, (b) HiLo by grid periods and (c) LSCM. FWHM for WFM, HiLo and LSCM is 0.77 μm , 0.38 μm , and 0.25 μm , respectively. Target: USAF-1951 Positive, group 7 elements 6, objective lens: 50× *NA* = 0.95, wavelength of light: WFM & HiLo 440 *nm*, LSCM 405 *nm*

Table 5. Lateral resolution comparison for each microscopic technique

	FWHM	vs. WFM
WFM	0.77 μm	
HiLo	0.38 μm	50 %
LSCM	0.25 μm	48.4 %

Axial resolution of HiLo technique according to grating periods

To assess the axial resolution, the full width at half maximum (FWHM) in the z direction was measured and compared to that of the Stokseth OTF model (Eq. (2.15)). Figure 2.19 shows the axial intensity profile measurement for HiLo and general WFM, using a protected silver mirror ((Ø = 1", PF1-03-P01, Thorlabs, Inc., USA). The intensity profile in HiLo was similar to that of the Stokseth OTF model. Moreover, since the axial intensity profile had a peak value at the mirror surface plane, the mirror surface position could be obtained easily. On the other hand, in the case of general WFM, it was difficult to identify a particular point as a surface point, although the intensity tended to decrease as the focal plane became away from the surface.

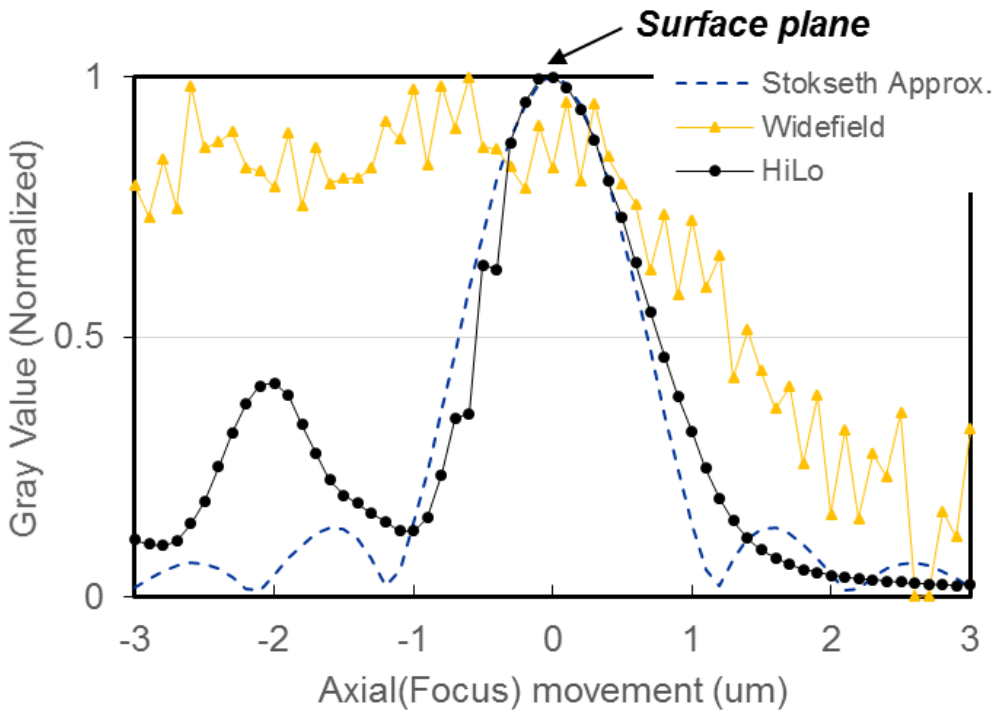

Figure 2.19 Axial intensity profile comparison of HiLo optical imaging technique (black circles and line) and general WFI (yellow triangles and line) using a protected silver mirror. The Stokseth OTF model (dashed line) is also presented as the theoretical value.

Optimization of grating period for HiLo optical imaging technique

The grating period is an essential parameter for determining axial resolution, as shown in Eq. (2.18). As shown in Figure 2.20, the FWHM of the axial intensity profile decreased as the grating period became smaller when measuring the axial intensity profile for a protected silver mirror (Ø = 1", PF1-03-P01, Thorlabs, Inc., USA) with different grating periods. In terms of axial resolution, the smaller the grating period, the higher the axial

resolution. However, as shown in Figure 2.20, the ratio of the main lobe to side lobes, which could be considered as SNR, increased as the grating period increased. So, choosing the optimal grating period required a tradeoff between the axial resolution and the noise due to side lobes. Side lobes are generated by spherical aberration, in which the intensity first increases at the point where the reflected light from the front focus is combined with the reflected light from the back focus [32]. To reduce the spherical aberration, a method of reducing the aperture of the optical system can be utilized [33]. However, when the aperture is reduced, it should be approached carefully because the FOV is also reduced by interlocking. In this study, we attempted to select the grating period in which the side lobe strength is the smallest, taking into account that the strength of the side lobe depends on the grating period. It should be noted that as the grating period increases, the axial resolution deteriorates. Considering such factors, the optimal grating period was set to be 25 μm at which the outlier around the edge is the smallest.

Table 6. Measured FWHM of axial intensity profile by objective lens and by grating spatial frequency

Grating spatial frequency	**FWHM by Objective Lens (μm)**	
	50× *NA* = 0.95	**40× *NA* = 0.65**
50 lp/mm	0.71	1.10
40 lp/mm	0.97	1.56
25 lp/mm	1.51	1.93

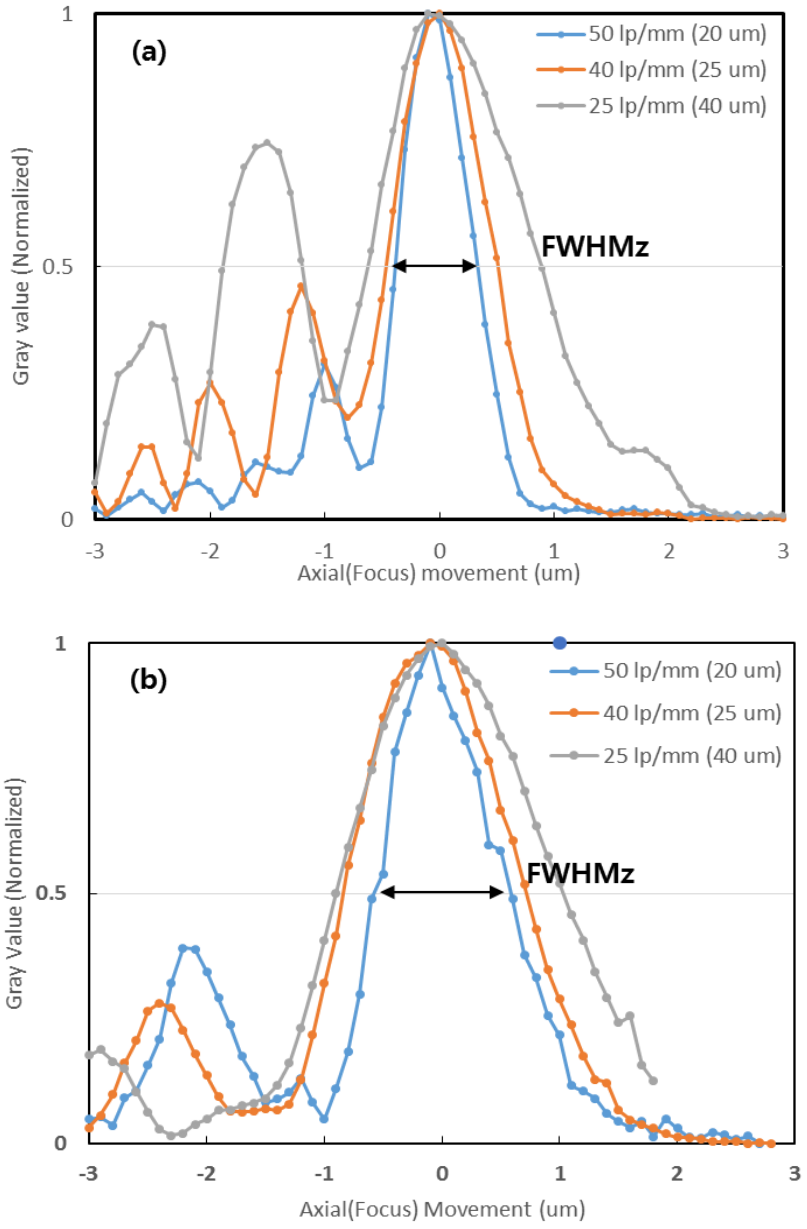

Figure 2.20 Variation of axial intensity profile with grid period; (a) objective lens is 50× *NA* = 0.95, (b) 40× *NA* = 0.65; specimen is standard flat sample (VLSI Standards, Inc.).

2.6. Summary and discussion

We aimed to develop a high speed, high precision, simple, and cost effective method for measuring 3D surface profile. For this purpose, the HiLo technique developed in the field of fluorescence imaging had been examined. To verify HiLo imaging technique, the mathematical background of HiLo imaging technique was reconstructed in accordance with the reflected light measurement of the surface, the experimental system was constructed using the general optical components and the custom-made parts, and the software algorithm was implemented. The performance was verified by using a standard sample with a proven shape and height and confirmed that the same horizontal and vertical brightness distribution as the fluorescence image can be obtained even when the reflected light of the target surface is measured. This means that HiLo technique can be applied even when the reflected light of the surface is measured. By changing the grating period, which is a core design parameter of HiLo imaging technique, it was also confirmed that the axial resolution was improved as the grating period was decreased.

While the feasibility of measuring the 3D surface profile with HiLo imaging technique is demonstrated, there are additional issues that need to be improved.

First, the physical movement of the grating filter makes it difficult to enable real-time imaging. The simplest way to eliminate the physical movement of the grating filter is using a spatial light modulator (SLM) or digital micro-mirror device (DMD) [34]. The grating filter movement time (about 0.5 ~ 1 s) can be shortened to several milliseconds by applying SLM or DMD. However, the imaging speed is limited to less than half of the camera's imaging speed since the method of acquiring a uniform image and a structured image sequentially remains unchanged. Both the SLM and the DMD shows higher noise

than a separately manufactured grating filter, due to light leakage between the pixel apertures and irregularities in the grating when the grating direction is not formed horizontally with the pixels. Also, this is not cost-effective, considering the high price of SLM and DMD equipment.

Another method of high-speed imaging is acquiring a uniform image and a structured image at the same time by changing the image acquisition method itself in parallel. By using two light sources with different wavelengths, uniform light and structured light illuminate simultaneously on the specimen, and the reflected light is separated by a bandpass filter to simultaneously image in two cameras. This method needs a more complicated optical system and requires correction for the wavelength difference of the two light sources, but it can be a fundamentally better alternative as it can acquire a real-time image using a general-purpose camera without moving the grating filter. This method is described more in detail in Chapter 3.

CHAPTER 3.

DUAL WAVELENGTH HILO IMAGING TECHNIQUE FOR SURFACE PROFILE MEASUREMENT

3.1. Dual-wavelength HiLo imaging technique

Basic idea of dual wavelength HiLo imaging technique

HiLo imaging technique requires time to move the pattern filter and take sequential shots to capture two images (Figure 2.6). To reduce the time required, the physical movement of the grating filter can be replaced by electronic image changes using a spatial light modulator (SLM) or a digital micro-mirror device (DMD) [34]. However, since two images still have to be taken sequentially, the image implementation speed is limited to less than half of the camera's imaging speed. A camera capable of high-speed imaging can be used, but the short camera exposure time will lower the contrast of the obtained image. Also, it is not the cost-effective method considering the price of a high-speed camera.

Therefore, we developed a dual-wavelength HiLo imaging technique that can acquire uniform illumination images and structured illumination images simultaneously by arranging two cameras in parallel (Figure 3.2).

The dual-wavelength HiLo technique is a technique for illuminating a specimen simultaneously with two light sources having different wavelengths and detecting the reflected lights with two cameras. If a grating pattern is arranged on the optical path of one of the two light sources, a uniform illumination image can be obtained from one camera and a structured illumination image can be obtained from the other camera.

As shown in Figure 3.1, unlike the case of measuring fluorescence, the frequency of incident light and reflected light is not changed when measuring reflected light, and different wavelengths can be separated and detected with a band pass filter which passes only the corresponding wavelength.

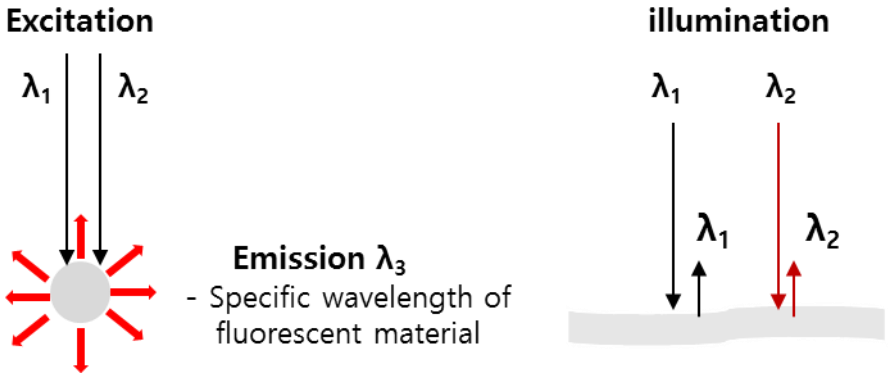

Figure 3.1 Conceptual diagram of wavelength change of fluorescence imaging (left) and reflected light imaging (right)

A concrete conceptual diagram of the system is shown in Figure 3.2.

First, the white light source is split by 50:50 beam splitter, and two uniform lights with different wavelengths are extracted by passing through a bandpass filter for each

predetermined wavelength. The selection criterion of the wavelength band satisfies the four following conditions.

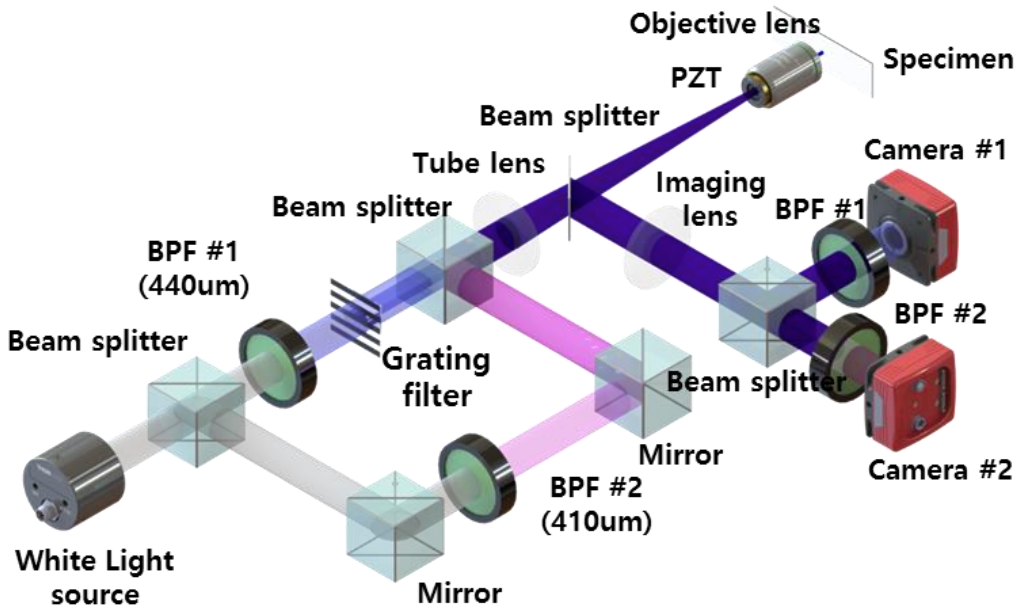

Figure 3.2 Optical system design of dual-wavelength HiLo technique

1) Considering the emission characteristics of the selected white light source, two lights with different wavelengths with sufficiently strong and similar intensities can be acquired.

2) The difference between wavelengths should be small in order to minimize the effect of aberration.

3) The wavelengths should be as short as possible in order to obtain good optical resolution in the visible region.

4) The bandpass filter should be able to separate two wavelengths without mutual interference.

Taking above conditions into account, we selected 410 *nm* wavelength whose intensity peaks at a position nearest to 440 *nm*, along with the 440 *nm* wavelength selected in Chapter 2. 3. The structured light is implemented by inserting a grating filter into the light path of one of the two light sources (the right side of band pass filter # 1 in Figure 3.2). Here the position of the grating filter should be aligned to the focal length (f = 200 mm) of the tube lens.

Next, the uniform light and structured light were integrated again using a 50:50 beam splitter, and the integrated light was simultaneously projected onto the sample through the tube lens and the objective lens.

Finally, the light reflected from the sample surface was measured through the objective lens and the imaging lens, and then split with 50:50 beam splitter. Then, the split lights passed through the band pass filter corresponding to each wavelength and images were acquired simultaneously with two cameras.

As the light passes through 4 beam splitters, *i.e.* separation of light source, integration of separated light sources, objective lens front, and camera front, the amount of light is reduced by half in each step. Therefore, the intensity of light source and the performance of the CCD camera such as pixel sensitivity, exposure time, gain, etc. should be good enough. In case a sufficiently strong light source is not available, the amount of light loss can be reduced by separating and integrating the light source, and replacing the beam splitter at the front of the camera with a dichroic mirror that can distinguish between 410 and 440 *nm* wavelengths.

Modification HiLo formula considering wavelength difference

The formula of HiLo technique was modified in consideration of dual-wavelength. In particular, in interpreting images taken using light sources of mutually different wavelengths, the focus position of the lens is changed according to the difference of wavelengths, and the resulting aberration is taken into account.

The change of the optical resolution due to the wavelength difference occurs because the refractive index of the lens changes with the wavelength and the PSF also changes accordingly. Consideration such effects, it is necessary to convert the PSF by one incident light among the two incident lights into a PSF by another incident light through mathematical calculation.

If the wavelengths of the two incident light beams are defined as λ_1 and λ_2, respectively, the uniform illumination image obtained from each wavelength can be expressed as Eq. (3.1), Eq. (3.2), respectively.

$$I_{\lambda_1}(\vec{\rho}) = O(\vec{\rho}) \otimes PSF_{\lambda_1}(\vec{\rho}) \tag{3.1}$$

$$I_{\lambda_2}(\vec{\rho}) = O(\vec{\rho}) \otimes PSF_{\lambda_2}(\vec{\rho}) \tag{3.2}$$

Eq. (3.1) and Eq. (3.2) are Fourier transformed, and the two equations are expressed as the ratio of OTF.

$$FT(I_{u,\lambda_1}(\vec{\rho})) = FT(O(\vec{\rho})) \bullet FT(PSF_{\lambda_1}(\vec{\rho})) \tag{3.3}$$

$$FT(I_{\lambda_2}(\vec{\rho})) = FT(O(\vec{\rho})) \bullet FT(PSF_{\lambda_2}(\vec{\rho})) \tag{3.4}$$

$$FT(I_{\lambda_2}(\vec{\rho})) = FT(I_{\lambda_1}(\vec{\rho}))\bullet\frac{OTF_{\lambda_2}(\vec{\rho}))}{OTF_{\lambda_1}(\vec{\rho}))} \tag{3.5}$$

Since the OTF is expressed by the Bessel function in the case of uniform illumination [35], the ratio of OTF can be approximated to the ratio of the wavelength in an optical system using the same lens and showing only the difference of the near wavelength.

$$\frac{OTF_{\lambda_2}(\vec{\rho}))}{OTF_{\lambda_1}(\vec{\rho}))} = \frac{J_1[z(1-\alpha\lambda_2)]}{J_1[z(1-\alpha\lambda_1)]}\frac{f(\lambda_2)}{f(\lambda_1)} \sim \frac{\lambda_2}{\lambda_1} \tag{3.6}$$

$$FT(I_{u,\lambda_2}(\vec{\rho})) \approx \frac{\lambda_2}{\lambda_1} FT(I_{u,\lambda_1}(\vec{\rho})) \tag{3.7}$$

$$I_{u,\lambda_2}(\vec{\rho}) \approx \frac{\lambda_2}{\lambda_1} I_{u,\lambda_1}(\vec{\rho}) \tag{3.8}$$

Therefore, in the dual wavelength HiLo technique, Eq. (2.2) through Eq. (2.11) should be modified to Eq.(3.9) through Eq.(3.12) to reflect the wavelength difference.

$$I_{u,\lambda_1}(x) = I_{in,\lambda_1}(x) + I_{out,\lambda_1}(x) = \frac{\lambda_2}{\lambda_1}\left(I_{in,\lambda_2}(x) + I_{out,\lambda_2}(x)\right) \tag{3.9}$$

$$I_{s,\lambda_2}(x) = I_{in,\lambda_2}(x)[1 + M\sin(2\pi\kappa_g x)] + I_{out,\lambda_2}(x) \tag{3.10}$$

$$LP_\kappa\left(\left|I_{s,\lambda_2}(x) - \frac{\lambda_2}{\lambda_1} I_{u,\lambda_1}(x)\right|\right) \approx \frac{2M}{\pi} LP_\kappa(I_{in,\lambda_2}(x)) \tag{3.11}$$

$$I_{HiLo}(x) = HP(I_{u,\lambda_1}(x)) + \eta\frac{\pi}{2M} LP_\kappa\left(\left|I_{s,\lambda_2}(x) - \frac{\lambda_2}{\lambda_1} I_{u,\lambda_1}(x)\right|\right) \tag{3.12}$$

That is, in the dual-wavelength HiLo, it is necessary to pre-process the uniform image among the acquired uniform image and the structured image to compensate for the wavelength equivalent to the structured image considering the wavelength difference. Once the preliminary work is performed and HiLo image is implemented by applying HiLo algorithm, it is possible to obtain the same result as existing HiLo technique.

Chromatic aberration correction

Differences between wavelengths causes aberration, which results in distorted images. Aberrations in the lens can be broadly divided into chromatic and monochromatic aberration [36][37]. Chromatic aberration is caused by the wavelength difference, while monochromatic aberration is caused by the shape of the lens.

In a dual-wavelength HiLo, only the aberration due to the difference in wavelength need to be considered because the only difference is in wavelength and the optical system and the lens used are the same. Therefore, in the dual wavelength HiLo, only the effect of chromatic aberration was considered. Chromatic aberration occurs because the refractive index of lens n differs according to the wavelength of the light source, and focal length difference occurs in the same optical system depending on the wavelength. Focal length difference not only makes images blurry due to defocusing but also causes magnitude difference of images; see Figure 3.3.

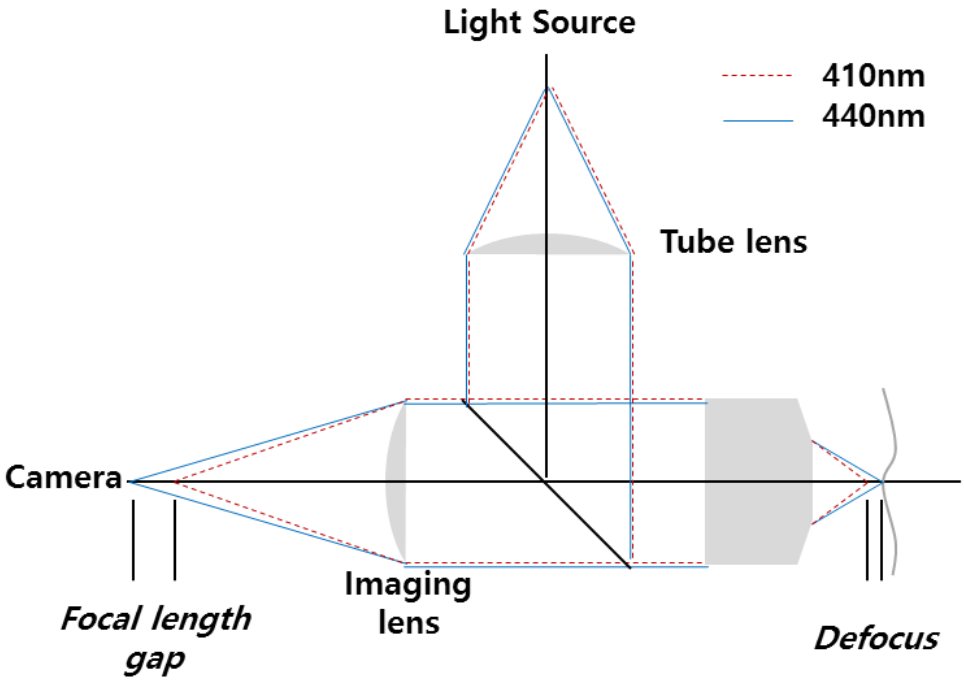

Figure 3.3. Chromatic aberration of wavelength difference

The change in focal length depending on the wavelength can be calculated using the lens maker's formula (see Figure 3.4). As for the curvature radius *R*, the value published by the lens manufacturer (Thorlabs, Inc.) can be used. And the refractive index of optical medium *n* of each wavelength can be obtained by using the values given by the lens manufacturer or by using the Sellmeier equation or Cauchy's equation [36].

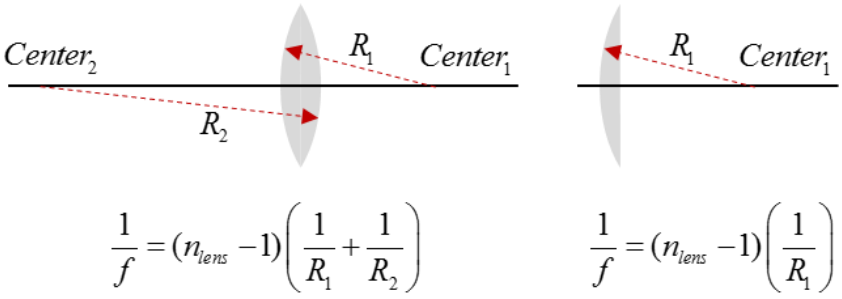

Figure 3.4 Lens maker's formula for thin lens: for bi-convex lens (left) and for Plano-convex lens (right)

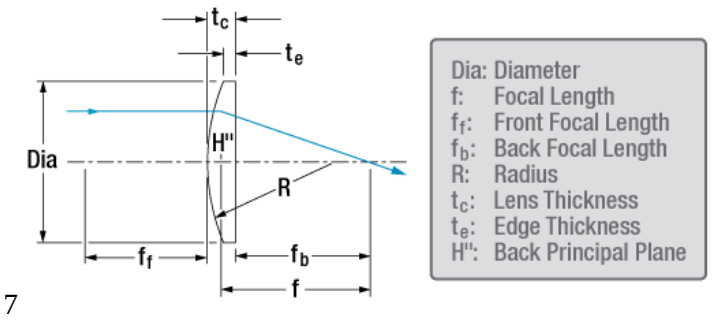

7

Figure 3.5 Dimension of Plano-convex lens (from Thorlabs Inc., USA)

The focal length of the lens adopted in this study is calculated by applying the lens maker's formula. It is confirmed that the focal length difference is 0.63 % for each lens according to the wavelength; see Table 7.

In the case of an objective lens, the focal length changes depending on the wavelength. Since several lenses are arranged in a complex manner within the lens, it is difficult to treat the lens as a thin lens. Moreover, as the manufacturer does not disclose the refractive index depending on the wavelength, it is difficult to calculate the exact focal length

changes for different wavelengths. However, it is reasonable to assume that the focal length changes at the same rate as the thin lens and measure experimentally.

Table 7. Focal length difference for each wavelength

Wavelength (*nm*)	Index of Refraction	Tube lens (f :200)	Imaging lens (f :150)
		R=103mm	R=73mm
410	1.529568767	194.5	146.0
440	1.52626886	195.7	146.9

The following two correction methods are applied considering the focal length difference according to the wavelength.

1. Adjustment of camera position and objective lens defocusing

Focal position matching should be considered for the camera and for the objective lens separately because the focus position is changed by the wavelength difference as shown in Figure 3.6. Since two movable cameras are used, the position of the image sensor of the camera is individually matched to the focus position of the imaging lens according to each wavelength.

Even in the case with the objective lens, although the focus position varies depending on the wavelength difference, it is difficult to reflect the change of the focus position directly to the hardware configuration because only one objective lens is used. For this reason, as

shown in the lower part of Figure 3.6, the focal position difference δ_{focal} was determined by experimentally finding the best focal point for each wavelength while moving the actual focal plane. The chromatic aberration was corrected by applying the method of matching the slice numbers of the image stack in 3D reconstruction considering the determined δ_{focal} values. Actual measurement showed that the δ_{focal} value varies depending on the objective lens; it is 1 μm with the 50 × objective lens and 1.1 μm with when the 40 × objective lens.

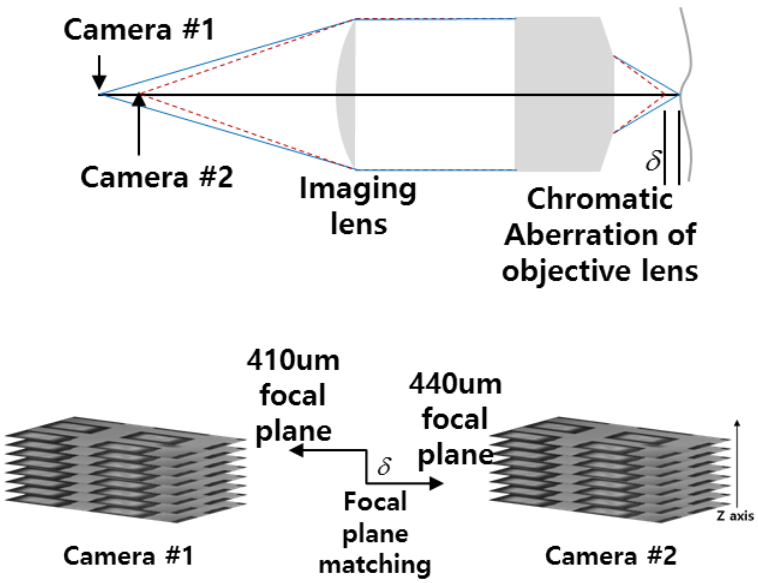

Figure 3.6 Focus position matching

2. Adjustment of image magnitude difference due to focal length difference

When the positions of the two cameras are corrected considering the focal length, the magnitude difference of the two images acquired occurs due to the distance difference.

That is, the distance with 410 *nm* wavelength is 0.63% shorter than that with 440 *nm* wavelength and the magnitude is also 0.63% smaller. The same phenomenon occurs with the objective lens. As calculated by Eq. (3.13), the image taken at the wavelength of 410 *nm* should be enlarged by 1.3%.

$$\frac{f_{imaging,440}}{f_{imaging,410}} \times \frac{f_{objective,440}}{f_{objective,410}} = 1.013 \tag{3.13}$$

Registration of images taken with two cameras

For acquiring a HiLo image by calculating a uniform illumination image and a structured illumination image, it is very important that two cameras photograph the same position of the specimen. In the existing HiLo system, there is no positional error between the uniform illumination image and the structured illumination image because two images are obtained one by one by replacing the pattern filter with one camera. However, in a dual-wavelength HiLo where images are acquired simultaneously with two different cameras, it is very difficult to get two cameras to capture the exact same position. For this reason, before entering HiLo processing, a pre-processing process is required during which two photographed images are compared with one another and registered at the same position.

As a representative method of image registration, Thévenaz P., Ruttimann U.E. and Unser M (1988) [38] and HSU and Wei Yen (2011) [39] have proposed the pyramid approach. This method compares two images based on the intensity of the image and then aligns them. While this method can be easily automated, it has a drawback that it is difficult to register when there is a difference in image signals of the two images to be registered caused by noise such as dust.

Cross correlation method is another image alignment method in which an appropriate control point is presented and images are aligned based on the point having the highest cross correlation as a reference point [40]. However, this method is not suitable for automating the entire system because the control point for image alignment has to be provided by the user.

In an actual HiLo image processing process, as shown in Figure 3.9, two images are simultaneously acquired through a dual camera, and then two matching images are aligned to create a HiLo image. The uniform image and the structured image registration are obtained by adopting the above-described pyramid approach or intensity-based registration (Figure 3.7). The image stack registration process is performed in the 3D reconstruction step using the acquired HiLo image stack, which is described in detail in Chapter 4.

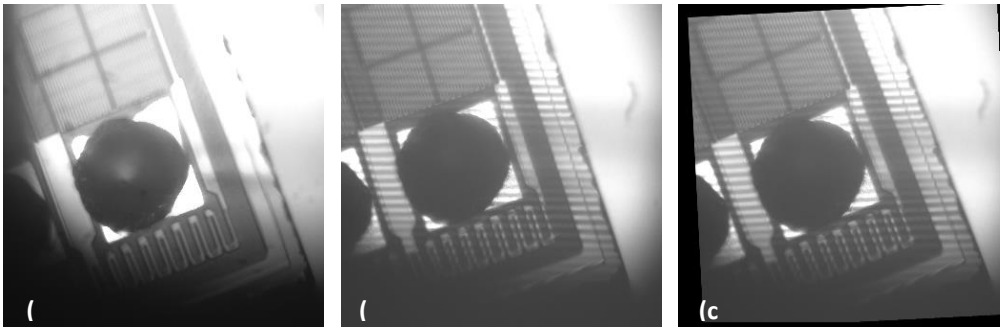

Figure 3.7 Example of two image registration: uniform illumination image (or reference image) (left), original structured illumination image (center), and registered structured illumination image (right)

3.2. Optical system modification for dual wavelength HiLo

The optical configuration and software shown in Figure 2.12 were modified to fit the dual-wavelength HiLo. In terms of optical configuration, the light source and detector was adjusted. In terms of software, the alignment of the two cameras and the algorithm to adjust the image considering the wavelength difference after image acquisition were added.

The modified optical configuration was shown in Figure 3.8. As described in Chapter 3.1, in order to utilize the 440 *nm* and 410 *nm* wavelengths as light sources, a bandpass filter selectively passing only those two wavelengths was disposed.

Among the light sources of the two wavelengths obtained, a structured light was generated by arranging the same grating filter as used in Chapter 2 on the optical path of the 440 *nm* light source (light source 1). The two light sources were combined using a 50:50 beam splitter and illuminated on the specimen surface through a tube lens and an objective lens. Light reflected from the specimen surface was separated by a 50:50 beam splitter through an imaging lens, passed through a bandpass filter corresponding to each wavelength, and was photographed simultaneously with two cameras.

Optical components such as objective lens, tube lens, and PZT were the same as those of the existing HiLo in Chapter 2.3. Both cameras were equipped with Allied Vision Technology's G-145-30fps Giga-E. Two Gigabit interface cards were installed in the PC separately to minimize the possibility of a bottleneck in image acquisition.

In constructing the experimental apparatus using the above two cameras, the center points of the cameras are physically aligned so that the same position of the specimen can be

simultaneously photographed. However, as described in Chapter 3.1, it is physically difficult to eliminate the fine position error of the photographed image. Therefore, the acquired image is matched with software

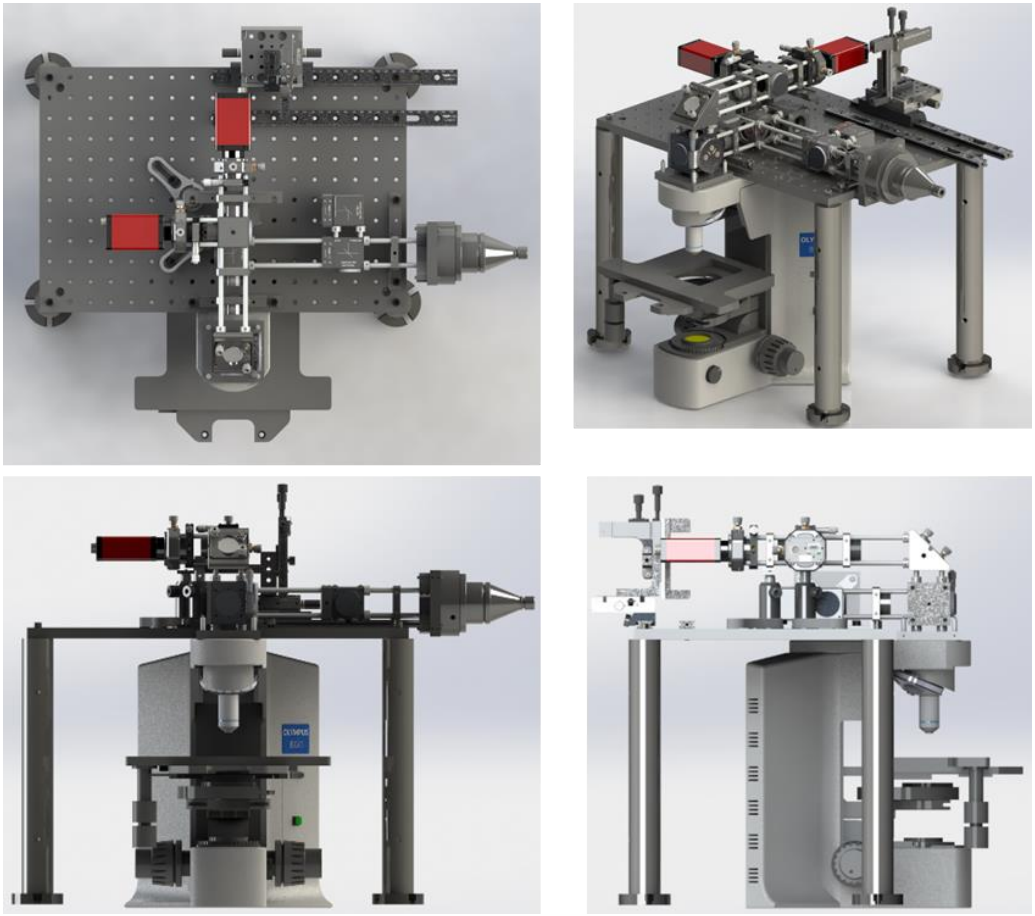

Figure 3.8 Optical configuration for dual-wavelength HiLo

Specification of the dual-wavelength HiLo imaging technique

To determine the basic specification of the optical configuration, we measured the FOV and image size per camera pixel of the dual-wavelength HiLo. Ronch-ruling with a distance of 400 lp/mm was taken by the same method as in Figure 2.13. The measured image areas using different cameras and objective lenses are shown in Table 8. Objective lens not only affects the FOV of the two cameras, but also the FOV ratio between the two cameras. In order to compensate for such effects, the size of the uniform image was enlarged and matched using the bicubic interpolation [41] in the pre-processing process.

Table 8. FOV and pixel size of the optical system of dual wavelength HiLo

		Camera 1 (410 *nm*)	**Camera 2 (440 *nm*)**	**Difference**
50×, *NA* 0.95	**pixel size** (μm)	0.130	0.128	1.76%
	Total Pixels	1388 × 1038	1388 × 1038	
	FOV (μm)	180.66 × 135.10	178.3 × 133.34	
40×, *NA* 0.65	**pixel size** (μm)	0.163	0.161	1.42%
	Total Pixels	1388 × 1038	1388 × 1038	
	FOV (μm)	226.96 × 169.73	223.79 × 167.36	

3.3. Software modification for dual-wavelength HiLo

Unlike existing HiLo technique, dual-wavelength HiLo technique acquire images using two different CCD cameras with different wavelength image signals. Therefore, it is necessary to perform pre-processing such as image magnitude correction and fine position error correction; see Figure 3.9.

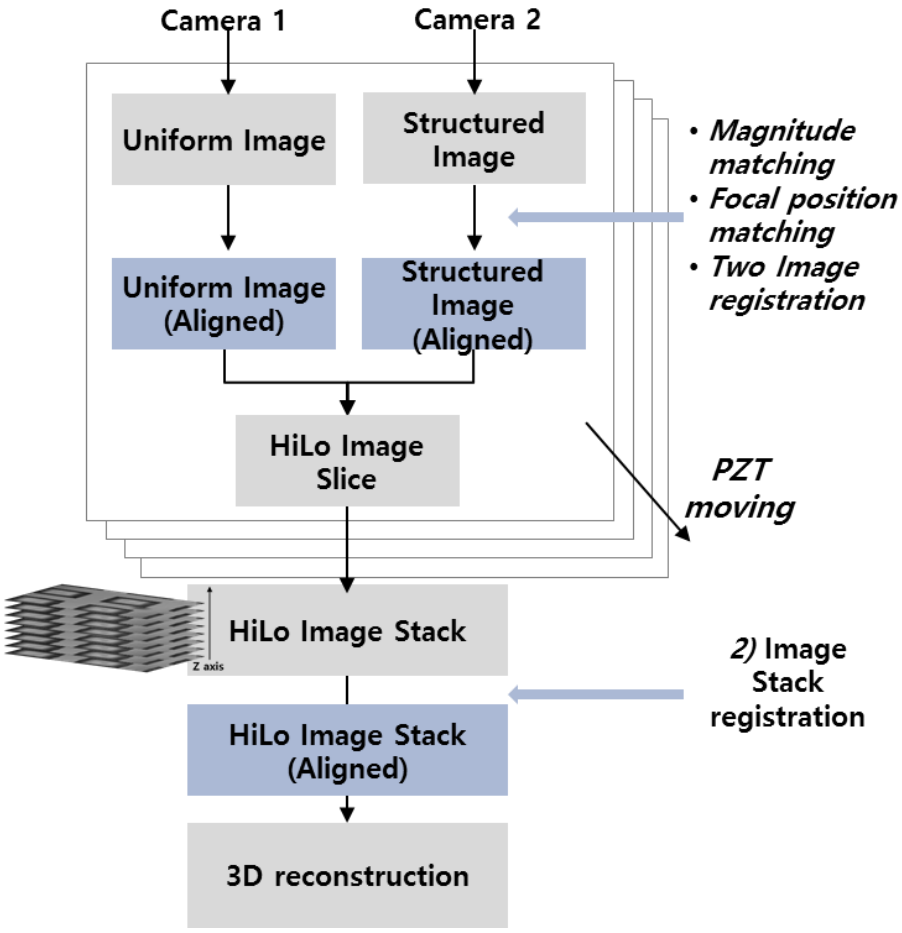

Figure 3.9 Modified software block diagram of 3D surface measurement with dual wavelength HiLo technique

3.4. Optical resolution of dual-wavelength HiLo and comparison to existing HiLo

In order to verify the performance of the dual wavelength HiLo, the lateral resolution and axial resolution were sequentially compared with those of the following four cases in the same manner as in Chapter 2.

Case 1) Commercial LSCM (LEXT OLS 5000, Olympus corp., Japan)

Case 2) WFM Image at illumination wavelength 440 *nm* / Camera 1

Case 3) Existing HiLo image using combination of uniform image at 440 *nm* / Camera1 and structured image at 440 *nm* / Camera 1

Case 4) Dual wavelength HiLo image using combination of Uniform image at 410 *nm* / Camera2, structured image at 440 *nm* / Camera 1

Lateral resolution of dual-dual wavelength HiLo

To compare the performance of each case, USAF-1951 Target group 7 was measured. 50× *NA* = 0.95 objective lens was used for all cases. By operating the equipment in the darkroom, the disturbance caused by other light sources was blocked as much as possible.

The measured FWHM values for WFM, existing HiLo, dual-wavelength HiLo, and LSCM are compared in Figure 3.10. It was confirmed that the same FWHM value as existing HiLo can be obtained even with the dual-wavelength HiLo method.

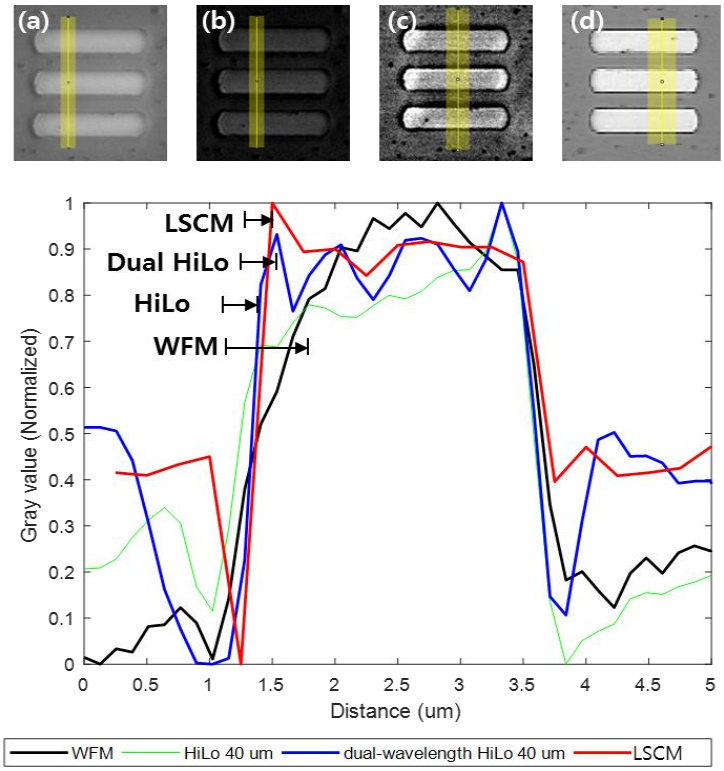

Figure 3.10 Lateral resolution comparison of (a) WFM, (b) existing HiLo, (c) dual-wavelength HiLo and (d) LSCM. FWHM for WFM, existing HiLo, dual-wavelength HiLo and LSCM is 0.77 μm , 0.38 μm , 0.38 μm , and 0.25 μm , respectively; Target: USAF-1951 Positive, group 7 elements 6, Objective lens: 50× *NA* = 0.95

Axial resolution of dual wavelength HiLo

Figure 3.11 and Table 9 show the axial response in the dual-wavelength HiLo. For comparison with existing HiLo, the same sample and the same objective lens were used. With dual-wavelength HiLo, the same axial response was shown and the same level of FWHM was measured as with existing HiLo.

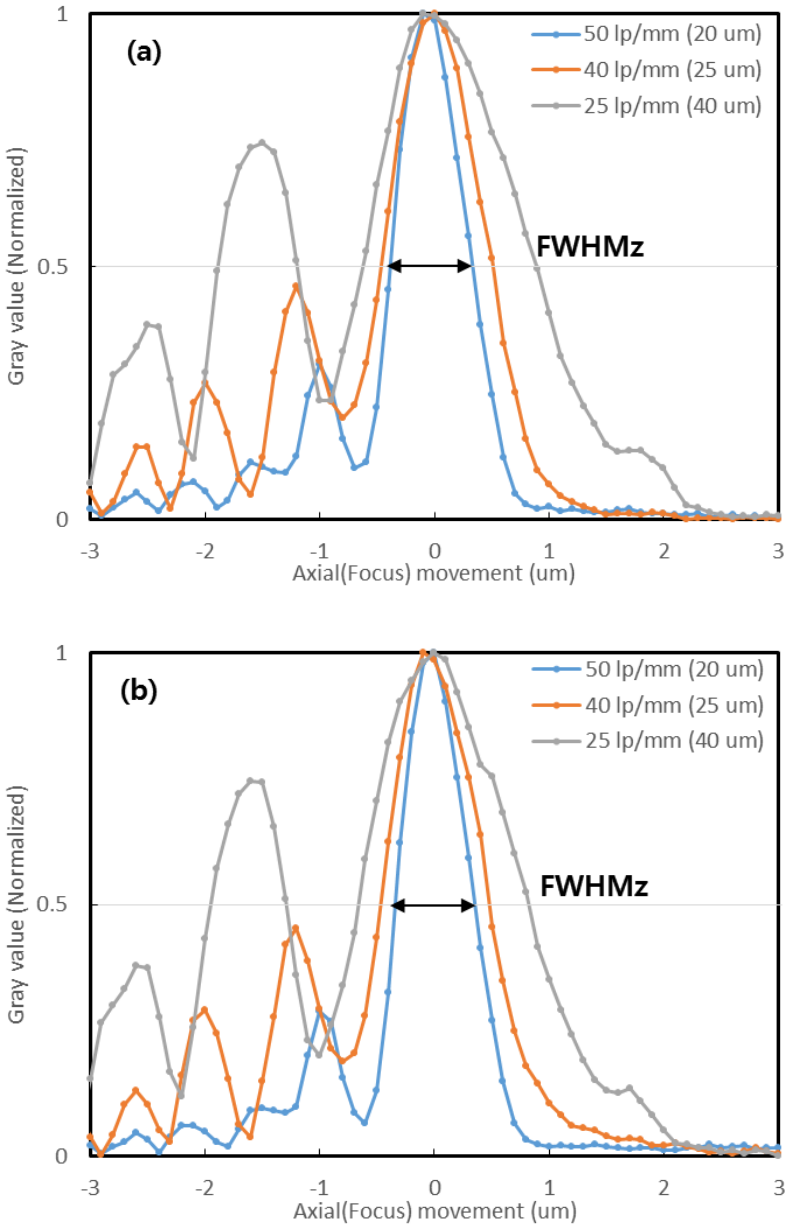

Figure 3.11 Axial intensity profile with grid period of (a) existing HiLo and (b) dual-wavelength HiLo; specimen is standard flat sample (VLSI Standards, Inc.); objective lens is 50× *NA* = 0.95

Table 9 FWHM of axial intensity profile by grating spatial frequency

(a) Existing HiLo (unit : μm)

No. of measure	FWHM by grating spatial frequency		
	50 lp/mm	40 lp/mm	25 lp/mm
1st	0.72	0.97	1.52
2nd	0.71	0.97	1.47
3rd	0.70	0.97	1.52
4th	0.71	0.97	1.51
5th	0.71	0.98	1.52
Mean	**0.71**	**0.97**	**1.51**
sigma	**0.5 %**	**0.4 %**	**1.9 %**

(b) Dual-wavelength HiLo (unit : μm)

No. of measure	FWHM by grating spatial frequency		
	50 lp/mm	40 lp/mm	25 lp/mm
1st	0.69	0.94	1.48
2nd	0.70	0.96	1.49
3rd	0.70	0.96	1.49
4th	0.70	0.97	1.49
5th	0.70	0.97	1.49
Mean	**0.70**	**0.96**	**1.49**
sigma	**0.2 %**	**1.1 %**	**0.3 %**

3.5. Summary and discussion

In order to improve the speed of the existing HiLo technique, which requires physical movement of the grating filter, we proposed a dual-wavelength HiLo technique that can simultaneously acquire uniform illumination images and structured illumination images in parallel. Considering that two cameras and two optical systems are constituted, the physical alignment of the two optical systems is proceeded, and the slight misalign of the two cameras is corrected with the software algorithm. In addition, the positions of the two cameras are adjusted in consideration of the difference of the focal lengths of the optical system due to the difference of the two wavelengths. Image size matching was also performed to correct the magnitude difference of the acquired images with a software algorithm.

The performance of the proposed dual-wavelength HiLo is evaluated by measuring lateral and axial resolutions and comparing them to those measured with existing HiLo technique. As a result, it is confirmed that the same level of resolution can be achieved with the dual-wavelength HiLo as with existing HiLo technique.

In conclusion, the proposed dual-wavelength HiLo method is an effective way to improve speed without sacrificing the performance of existing HiLo technology.

CHAPTER 4.

3D RECONSTRUCTUON WITH VERTICALLY SCANNED HILO IMAGE STACK

4.1. Concept of 3D reconstruction using 2D image slices (image stack)

Chapters 2 and 3 describe the process of obtaining a 2D HiLo image corresponding to a specific z-axis focal plane using HiLo / dual-wavelength HiLo technology.

Chapter 4 describes how to reconstruct the 3D surface profile by signal processing a number of 2D HiLo images acquired while moving the focal plane of the objective lens at a specific interval in the z-axis direction using PZT.

First, the objective lens is scanned in the z-axis direction using PZT, and the 2D HiLo image slice corresponding to each height is obtained while moving the z-axis at regular intervals, and the image stack is constructed as shown in Figure 4.1. Then, the 3D surface profile of the specimen is obtained by applying a numerical algorithm optimized to HiLo image stack.

This process is similar to the “focus variable” or “shape from focus” method in that PZT is used to find the focal plane in the acquired image stack while moving the focus. However, in HiLo technology, there is a difference in that it is easy to obtain the height information of the focal plane by removing the blur image signal corresponding to the background from the acquisition step of the 2D image corresponding to each focal plane.

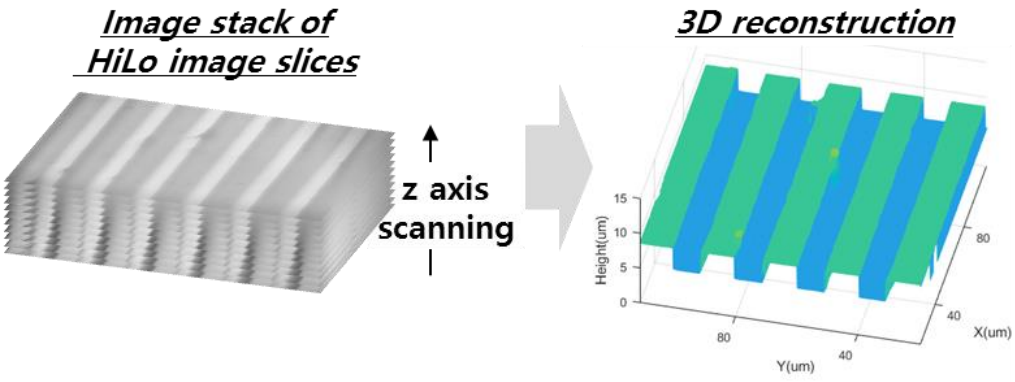

Figure 4.1 Reconstructed 3D surface profile using 2D image slices obtained by z-direction scanning; typical z-axis step size: 0.1 μm

Prior to 3D reconstruction using image stack, it is necessary to carry out a pre-processing process to correct alignment errors of optical system through image registration algorithm. Also, post-processing should be performed to calibrate the surface profile obtained through the 3D reconstruction algorithm, considering the shape and size of the actual specimen.

Chapter 4.2 through Chapter 4.4 describe pre-processing, 3D reconstruction algorithm implementation, and post-processing. In Chapter 4.5, the reconstructed 3D surface profile using HiLo technique for the actual specimen is compared with the reconstructed 3D surface profile using the LSCM, and the results are analyzed.

4.2. Preprocessing before applying 3D reconstruction algorithm to the image stack – image stack registration through z-axis

HiLo technique improves the resolution in the horizontal direction by removing the background signal from the non-focal plane, and also finds the position of the 3D surface on the image stack acquired in the axial direction.

However, since the optical system itself is not in perfect alignment, the position of the acquired image may be shifted due to the movement in the z-axis direction. In this case, even if the three-dimensional shape is reconstructed, a shape different from the actual shape of the measurement sample can be obtained. Figure 4.2 shows 100 images obtained by moving the z-axis at 1 μm intervals for testing the optical system and observing them on the orthogonal axis. As shown in the Figure 4.2, it can be seen that the z-axis direction image is deflected in a specific direction because it is not aligned in the z-axis direction. For this reason, it is important to correct the positions between the respective image slices and to register them in the axial direction.

In this study, the pyramid approach used in Chapter 3 was applied once again to the image stack to register the axially acquired N image slices. Figure 4.3 shows the registration result, and it is confirmed that the artifact due to miss-alignment of the optical system is improved as compared with Figure 4.2.

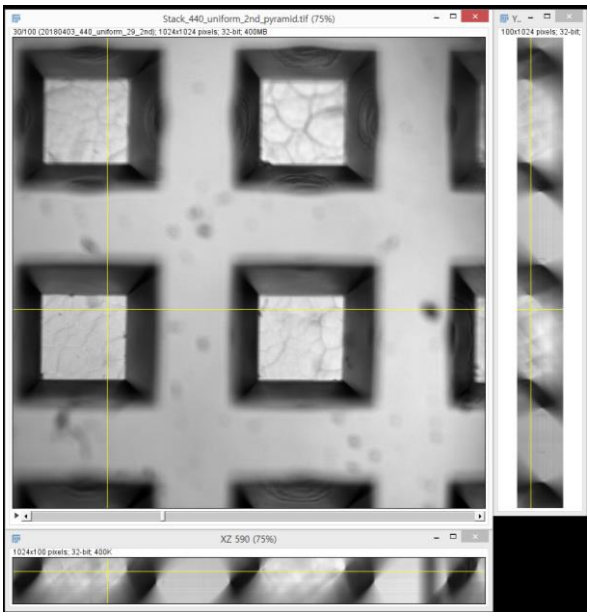

Figure 4.2 Orthogonal view of the image stack, before image registration through z-axis

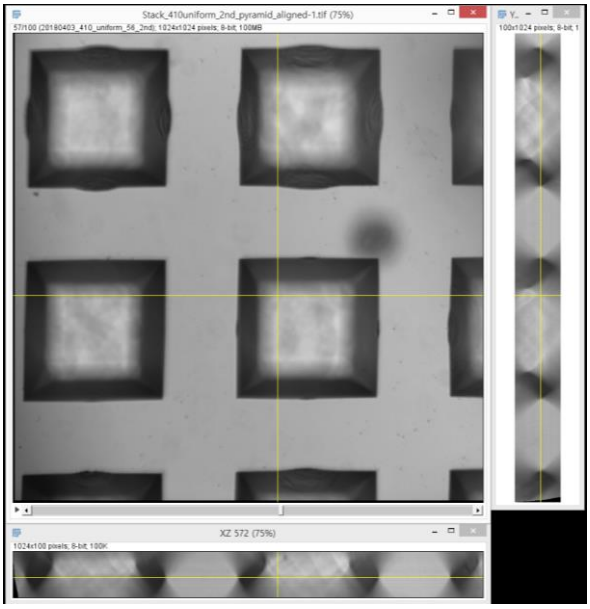

Figure 4.3 Orthogonal view of the image stack, after image registration through z-axis

In above method, image alignment is performed in the process of acquiring each image while moving the focal plane in the z-axis direction. After implementing HiLo image through the image alignment, the pyramid approach is used once again to complete the image alignment. However, this method has a problem in that it does not guarantee appropriate results as it depends on the state and characteristics of the uniform image and the structured image. In other words, as shown in Figure 4.4, there are many cases in which registration is not normally performed by the sinusoidal signal of the grating filter included in the structured image.

The image registration time for N images is expressed by $t_{align} \times N + t_{align} \times (N-1)$, and experiments show that the image alignment time t_{align} of 1,024 $\times$ 1,024 size is 1 ~ 1.5 seconds. Therefore, with an image stack with N = 400, the image alignment process takes over 5 minutes.

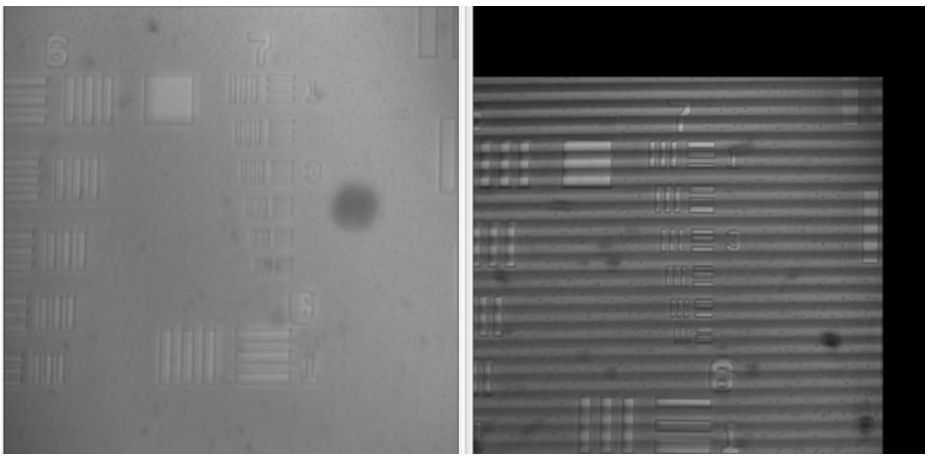

Figure 4.4 Error on image registration process; reference 410 *nm* uniform image (left) and aligned 440 *nm* structured image by pyramid approach (right)

Considering the computation time of image alignment and the possibility of errors in the alignment process, we concluded that the proposed method would not be suitable for the purpose of this study. Therefore, the image alignment algorithm has been modified to improve the reliability and speed of image alignment processing (Figure 4.5).

1) Acquire images simultaneously with Camera 1 and Camera 2 without pattern filter in the initial optical system initialization process, and obtain image stack of uniform illumination image slices in z direction
2) The images (taken with Camera 1) corresponding to the uniform illumination image in the two stacks are sorted by the intensity-based registration technique described above, and the x-axis and y-axis displacement values of each image slice are separately recorded ($\Delta x_1, \Delta y_1$ corresponding to z values).
3) The corresponding image slice in another Image Stack are sorted with respect to each image slice and the displacement of the x-axis and the displacement of the y-axis are separately recorded ($\Delta x_2, \Delta y_2$ corresponding to z values).
4) The x-axis displacement and the y-axis displacement recorded in 2) and 3) are applied to the subsequent uniform illumination image and structured illumination image (The image taken with Camera 1 is moved Δx_1, Δy_1 of its corresponding z value and the image taken with Camera 2 is moved $\Delta x_1 + \Delta x_2$, $\Delta y_1 + \Delta y_2$ from the origin).

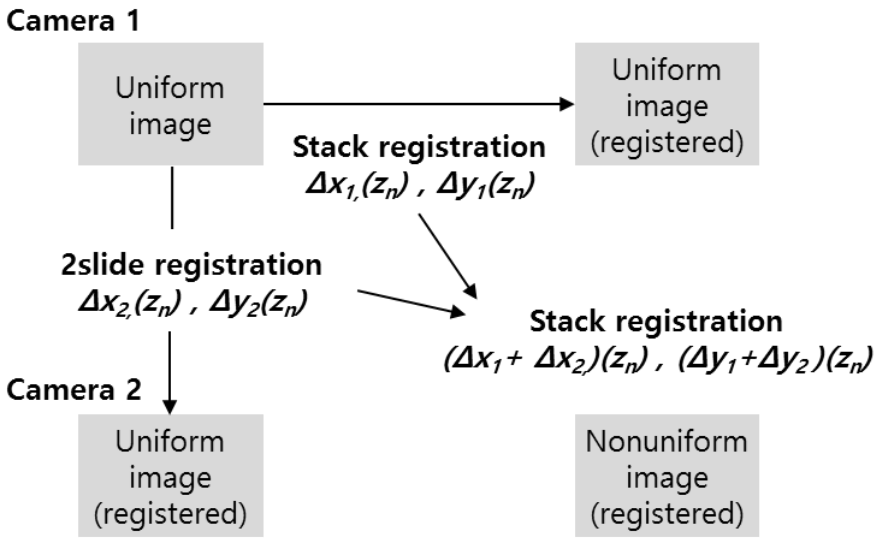

Figure 4.5 3-step image registration algorithm

The final two aligned images and the HiLo image will have a dark area due to the alignment process. In HiLo image processing process, the dark region that may have occurred by unnecessary noise is cropped. The pixel size of the original image acquired through the selected camera are 1388 × 1038 but only 1024 × 1024 from center is selected considering that the measurement error increases due to lens distortion as the distance from the center increases.

In order to measure the actual reference value, we arranged 100 images of the sample 4) pyramid structures obtained at 1 μm intervals in the z direction. First, the uniform illumination image obtained by the 410 *nm* incident light was aligned in the z direction, Δx_1 and Δy_1 ware obtained. This will be used as an alignment reference value for 410 μm uniform illumination images when measuring other parts of the same sample.

Then, the 440 *nm* uniform illumination image was sequentially aligned with the primary aligned uniform illumination image as the reference, and Δx_2 , Δy_2 were obtained.

Finally, we applied Δx_2 , Δy_2 to the 440 *nm* structured illumination image to complete the registration.

The alignment results are shown in Figure 4.6. The optical system is slightly tilted in the z direction and the alignment error in the vertical direction of the optical system for measuring the 440 μm wavelength band is larger. Since it is very difficult to correct it physically, the image stacks taken in the same optical system are then aligned by software based on this profile

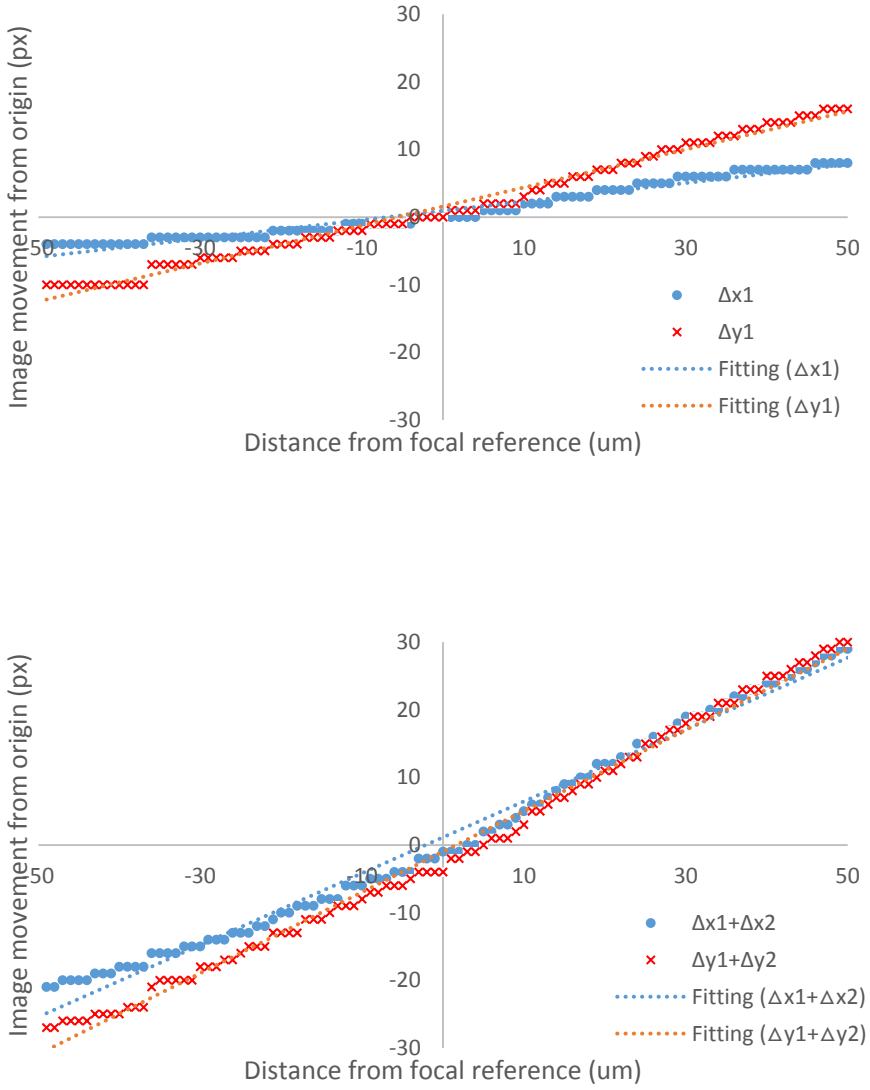

Figure 4.6 Align profile (pixel movement) of each image slice; 410 *nm* uniform image stack (top), 440 *nm* structured image stack (bottom)

4.3. 3D reconstruction with image stack

The final goal of this study is to realize 3D images using N HiLo images acquired through vertical scanning in the z-axis direction. An algorithm for 3D reconstruction using an image stack was proposed and the repeatability, which is a key performance factor of microscopy, was measured using a standard flat sample.

3D reconstruction algorithm

As described in Chapter 2.2, each point *(x, y)* of the scanned image along the z axis shows the brightest and clearest image at the z-point corresponding to the focal plane, and the brightness and sharpness decrease as the distance from the focal plane increases. Using this axial response, height information can be obtained at each *(x, y)* point and the surface profile in the whole image can be acquired.

In order to identify the $z_{focal}(x,y)$ value corresponding to the focal plane at a specific *(x, y)* point of the Image Stack, the following four methods are typically used [8].

1) The z value when the intensity of the corresponding point *(a, b; z)* of each image slice becomes maximum (*i.e.* brightest) for the specific *(a, b)* is recognized as the focal plane.

$$z_{focal}(a,b) = z(a,b; at\ Max(i(a,b)) \tag{4.1}$$

where, $z_{focal}(x,y)$: the surface position at given lateral position (*x,y*)

$i(a,b)$: gray values of each image slices at *(a,b).*

2) The intensity value obtained from 1) is gaussian or parabola fitted and the z value corresponding to the peak is recognized as the focal plane

$$z_{focal}(a,b) = z\left(\frac{d}{dz} f(i_z(a,b)) = 0 \right) \tag{4.2}$$

where, f : curve fitting function (Gaussian or parabola)

3) The z values corresponding to the intensity which is 50% or more based on the peak value among the intensities obtained from 1) are selected and the value corresponding to the Barycenter is recognized as the focal plane.

$$z_{focal}(a,b) = average\left(z\left(i_z(a,b) = \frac{1}{2} Max(i_z(a,b)) \right) \right) \tag{4.3}$$

4) A 5 × 5 or 7 × 7 region is set as the intensity matrix around a specific *(x, y)* position of the individual image, and the image number having the largest standard deviation of the matrix is regarded as the focal plane

$$z_{focal}(a,b) = z(a,b; at\ Max(\sigma(M))) \tag{4.4}$$

where, σ : standard deviation, and

M : 5 × 5 or 7 × 7 intensity matrix near *(a,b).*

In this study, we adopt the first method to shorten the calculation time in consideration of the fact that the axial response of HiLo technique is sufficiently narrow. However, it is difficult to measure the exact height by the method of finding the brightest point, due to the noise generated by the diffuse reflection occurring on the surface of the sample. Therefore, the mean gray value $m(x, y)$ of a 3 × 3 matrix near the lateral position *(x,y)* is

used instead to find the axial position z value of the focal plane. If the mean gray value $m(x, y)$ at given position is smaller than the threshold value, which can be calculated as the mean gray value of a HiLo image at a totally out-of-focus position, then that point is excluded from the calculation, thereby reducing the influence of noise and improving the operation speed.

$$z_{focal}(x, y) = z(x, y; at\ Max(m(x, y)) \tag{4.5}$$

$$m(x, y) = \begin{cases} m(x, y), if\ \ m(x, y) \geq threshold \\ 0 \quad\ , if\ \ m(x, y) < threshold \end{cases}$$

In this way, we can measure the height by finding the brightest point in the axial direction at each point on the image stack. However, this is to find the brightest point among the points corresponding to the position of the PZT, and therefore, it will be an approximation of the actual focal plane position. To measure the focal plane more precisely, it is more reasonable to regard the point corresponding to the peak value of the curve as the focal plane by curve fitting around the brightest point (Figure 4.7) using Gaussian interpolation [20] or second-order polynomial [42]. This method has the disadvantage of longer computation time, compared to simple brightest-point searching, but it has the advantage of yielding more reliable results. Further research is expected to reduce computation time, and to enhance accuracy for surface profile measurements by applying multiple noise-suppression methods [43].

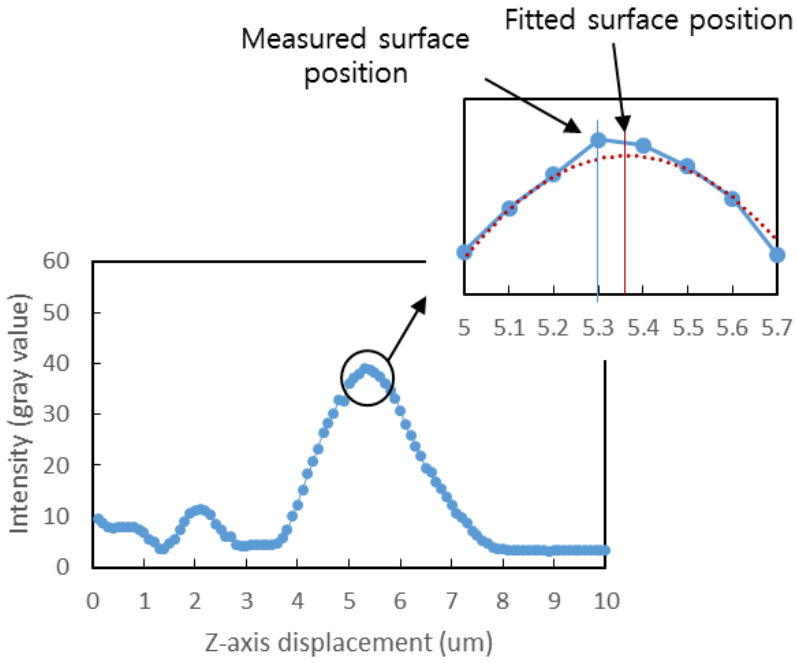

Figure 4.7 Illustration of curve fitting to determine the focal plane

The height profile of the protected silver mirror was measured, to confirm the precision of the axial surface position. The image stack was obtained by moving the focal plane in the *z* direction in steps of 0.1 μm, and the 3D profile was obtained according to Eq. (4.5). The standard deviation of the 3D measurement was 0.069 μm. For a more accurate result, as described in Chapter 2 and shown in Figure 4.7, we recalculated the surface position by curve fitting near the brightest point using a second-order polynomial. After curve fitting, we got a smaller value for the standard deviation, 0.017 μm. Therefore we can confirm that the height-profile precision of HiLo optical imaging technique is about 20 *nm* (Figure 4.8), which is about 1.5 times the standard deviation of 13 *nm* measured by commercial LSCM.

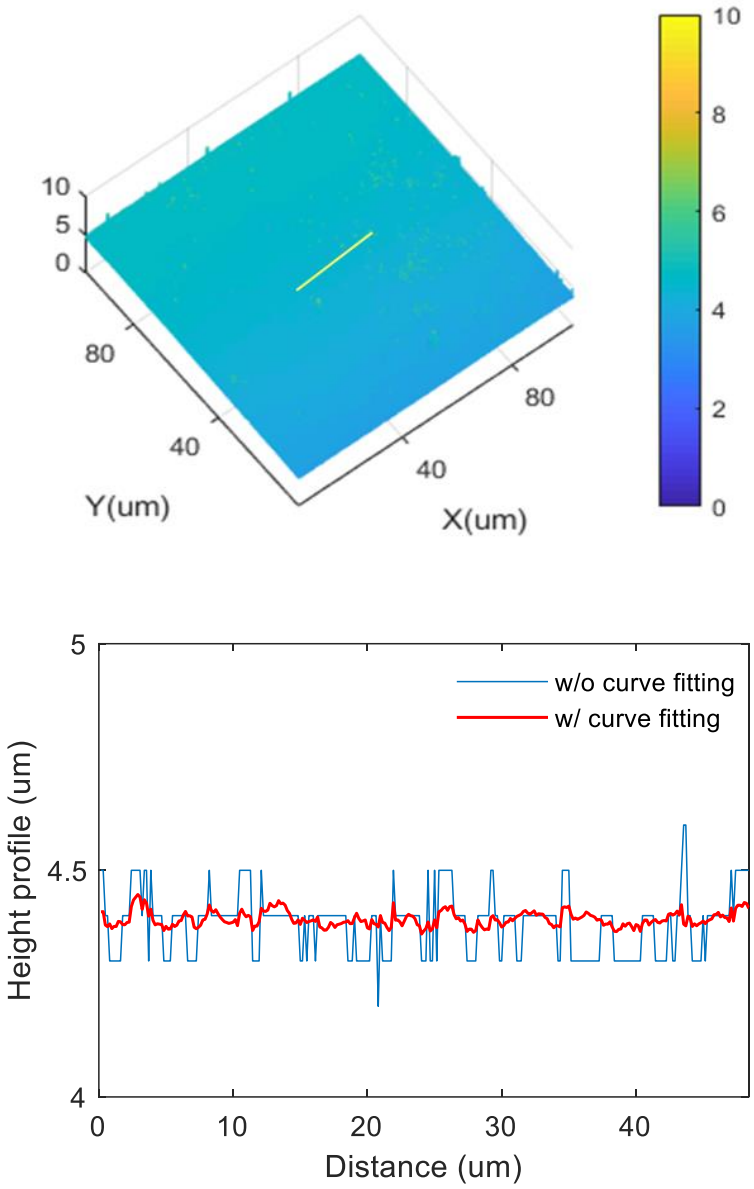

Figure 4.8. 3D surface profile and height profile of a protected silver mirror by applying existing HiLo technique and searching brightest point through z-axis. Measured standard deviation of the height profile is 0.069 μm (without curve fitting) and 0.017 μm (with curve fitting); objective lens: 50×, *NA* = 0.95

Repeatability of 3D surface profile measurement

Axial resolution is affected by grating spatial frequency, axial scanning step size, signal-to-noise, 3D reconstruction algorithm, and optical system registration. In order to measure the axial precision of the proposed HiLo and dual-wavelength HiLo technique, a repeatability test was conducted to obtain the standard deviations by imaging the same specimen multiple times.

For the test, we used a step height standard sample (step height: 3 μm, VLSI Standards Inc., USA) that guarantees the flatness and height step of the surface. The standard sample was measured by AFM and the height step was measured as 3.0007 μm.

The results are shown in Figure 4.9 and Table 10. As the grating spatial frequency becomes smaller, *i.e.* the grating period becomes larger, the standard deviation becomes smaller. On the other hand, as the grating period becomes larger, outliers increase in number, which makes it difficult to guarantee the reliability of measurement.

Table 10. Average standard deviation of 10 repeated measurement result

Grating spatial frequency	Standard deviation (n=10)
50 lp/mm (20 μm)	0.162 μm
40 lp/mm (25 μm)	0.051 μm
25 lp/mm (40 μm)	0.044 μm

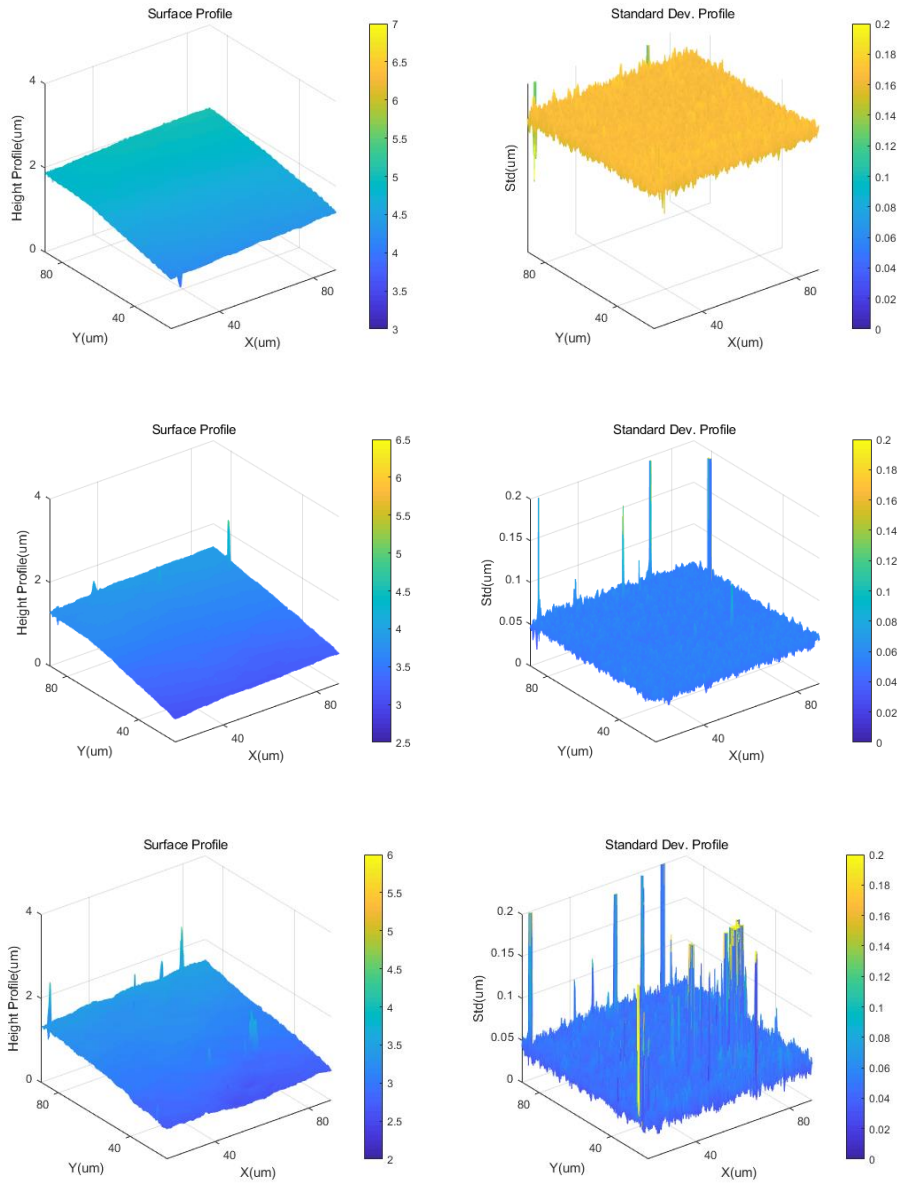

Figure 4.9 Repeatability test result : The surface profile of the standard flat surface measured 10 times, average value of surface profile (left), standard deviation of the intensity value in the z direction at each *(x, y)* point (right); objective lens: 50× *NA* = 0.95, grating filter: 20 μm (top), 25 μm (middle), 40 μm (bottom)

Reselection of optimal grating spatial frequency

In Chapter 2.5 and Chapter 3.4, 50 lp/mm, or grid period 20 μm, was chosen as the grating spatial frequency at which the FWHM is the minimum axial response. However, the grating period of 20 μm is more disadvantageous than the larger grating period in terms of repeatability of the 3D reconstruction. For this reason, 25 μm is reselected as the optimum grating spatial frequency considering FWHM, repeatability, and outlier generation simultaneously.

4.4. Post-processing after getting the 3D surface profile with standard sample

Even though the 3D surface profile is implemented using the suggested 3D reconstruction algorithm, the result is different from the actual shape of the specimen due to misalignment of the optical system, lens aberration, non-uniformity in the light source and sensor error. Therefore, some calibration through a post-processing process is necessary in order to make the result as close as possible to the shape of the specimen.

For post-processing, the standard sample used in Chapter 4.3 was measured, and the result was compared with the standard sample to be calibrated. In this study, we calibrated the surface flatness, outlier, and height, which have the greatest effect on measured values.

Surface flatness calibration with standard sample

Distortion of the 3D reconstruction result occurs due to the alignment of the optical system and aberration of the lens. That is, even if a flat surface is measured, the measurement result does not appear flat. Therefore, it is necessary to calibrate the measurement results using a standard flat sample. For this, a flat surface was measured several times as in Eq. (4.6) ~ Eq. (4.9), and the mean value of the flat surface was obtained. The flatness was then corrected by subtracting the mean value from the 3D surface profile of the specimen to be measured.

$$z_{measured}(x,y) = z_{actual}(x,y) + z_{error}(x,y) \tag{4.6}$$

$$z_{\text{standard},measured}(x,y) = z_{\text{standard},actual}(x,y) + z_{error}(x,y) \tag{4.7}$$

$$z_{\text{standard},measured} = mean(z_{i,\text{stndard},measured}(x,y)) \tag{4.8}$$

$$z_{actual}(x,y) = z_{measured}(x,y) - 1/n \sum_{i=1}^{n} \left(z_{i,reference}(x,y) - mean(z_{i,reference}(x,y)) \right) \tag{4.9}$$

First, the standard sample used in Chapter 4.3 was measured 10 times and the mean value was obtained. The reference 3D surface profile of the flat surface was obtained by applying a 7 × 7 median filter to remove the outlier (see Figure 4.10 (a)) [44]. Then, by subtracting the obtained reference data from the 3D surface profile value of the specimen to be measured, a flat surface-corrected 3D surface profile can be obtained (see Figure 4.10 (b) (c) (d)).

However, even if the same specimen is measured with the microscope, the measurement result slightly varies depending on the spatial frequency of the objective lens and the grating. Therefore, it should be noted that reference values corresponding to the combination of the two core measurement variables must be held in advance.

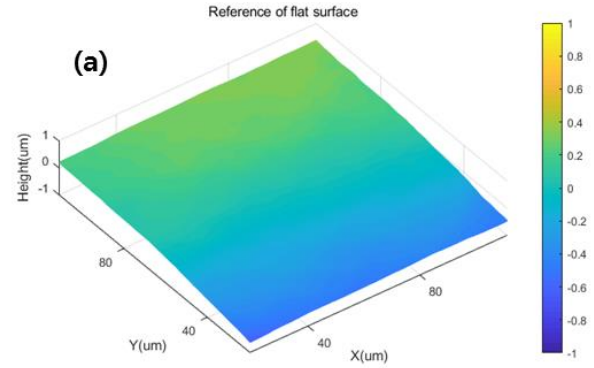
Reference of flat surface
(a)
Height(um)
1
0
-1
80
40
Y(um)
40
80
X(um)
1
0.8
0.6
0.4
0.2
0
-0.2
-0.4
-0.6
-0.8
-1

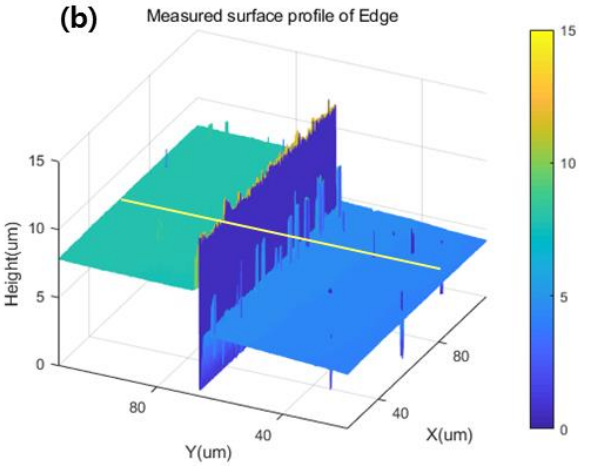
(b)
Measured surface profile of Edge
Height(um)
15
10
5
0
80
40
Y(um)
40
80
X(um)
15
10
5
0

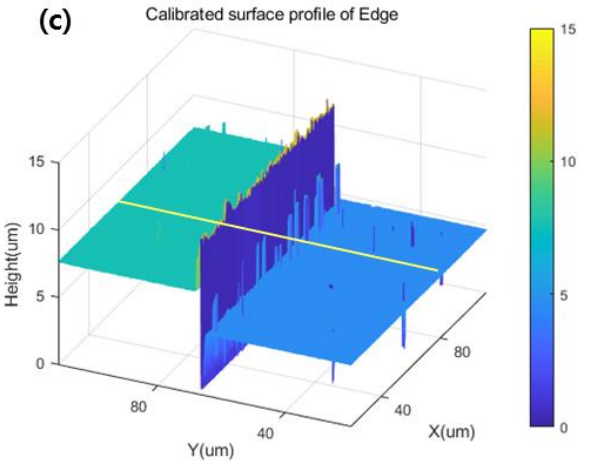
(c)
Calibrated surface profile of Edge
Height(um)
15
10
5
0
80
40
Y(um)
40
80
X(um)
15
10
5
0

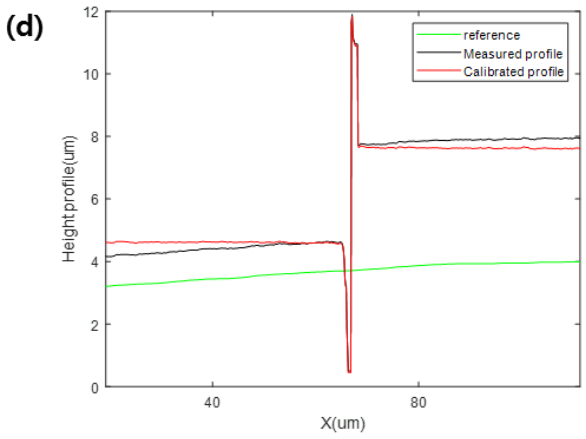

Figure 4.10 Surface flatness calibration by using standard sample; (a) surface profile of reference flat surface, (b) measured profile, (c) calibrated profile, (d) height profile of each case

Outlier calibration with median filter

The 3D surface profile measured by HiLo technique has a batwing corresponding to the outlier at the edge as shown in Figure 4.10 (d). This is because it is difficult to measure the exact focal plane due to diffuse reflection at the edge of the specimen. This phenomenon appears in white light microscopy using vertical scanning such as WLI and LSCM [45] .

Various techniques have been developed to remove outliers from surface profile measurements and are documented in the ISO 16610 / TS standard [46]. Most of the techniques utilize the method of applying the numerical filter using the information of the peripheral height of a specific point *(a,b)* of the measured 3D profile. In this study, the outlier was removed by applying the [2n + 1 × 2n + 1] median filter proposed by Ismail *et al*. [44]. It should be noted that as n increases, the outlier is effectively removed, but

the 3D profile is made smooth and it is impossible to recognize the surface roughness information.

Figure 4.11 shows the results of applying the [25 × 25] median filter to Figure 4.10(c). It can be seen that the batwing effect on the edge has been removed. In addition, the results of applying the grid type structure of the standard sample to verify the applicability in a more complex shape are shown in Figure 4.12. The gap of grid is 10 μm, and the width of the structure is also 10 μm.

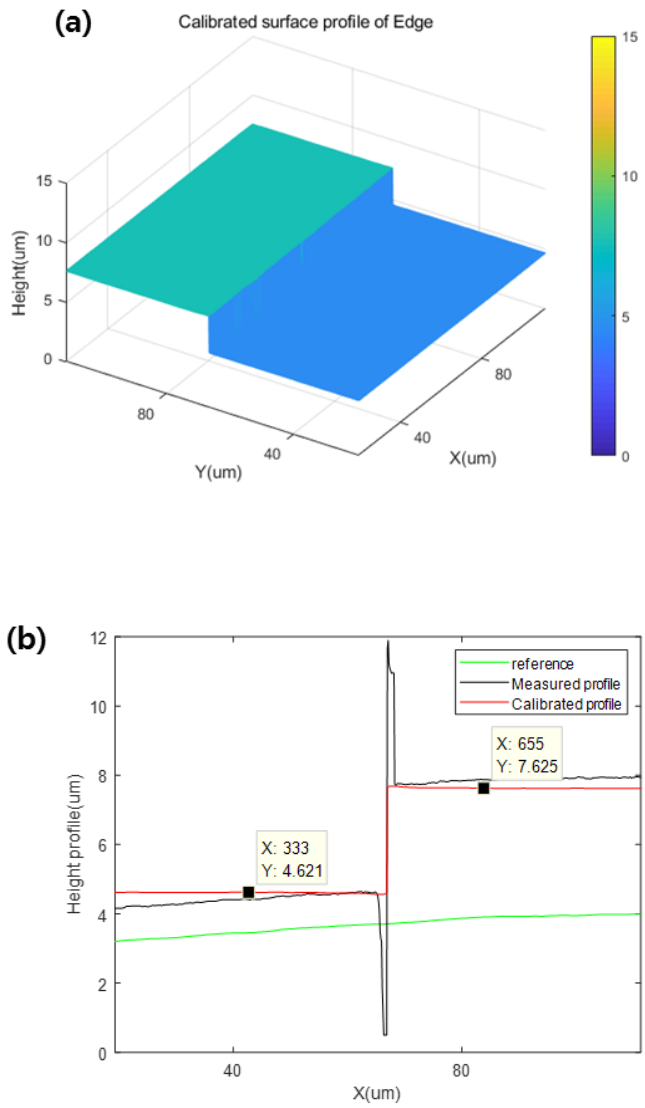

Figure 4.11 Edge calibration by median filter (single edge); [25 × 25] median filter is applied.

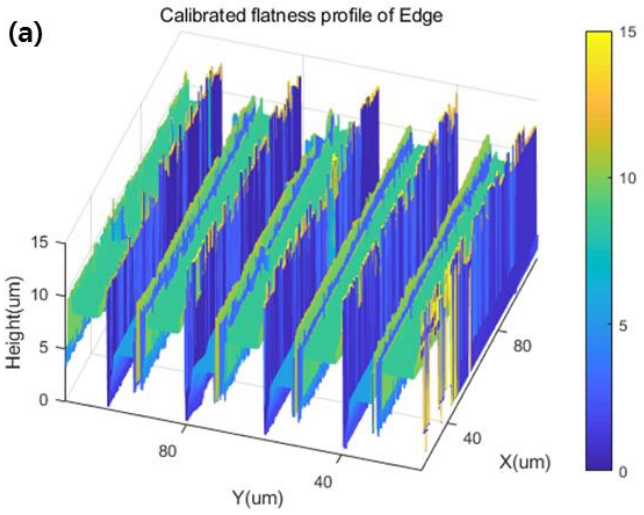
(a)
Calibrated flatness profile of Edge
Height(um)
15
10
5
0
80
40
Y(um)
80
40
X(um)
15
10
5
0

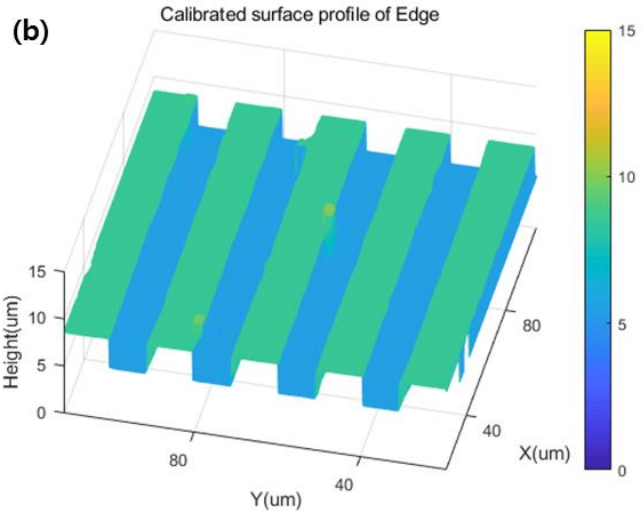
(b)
Calibrated surface profile of Edge
Height(um)
15
10
5
0
80
40
Y(um)
80
40
X(um)
15
10
5
0

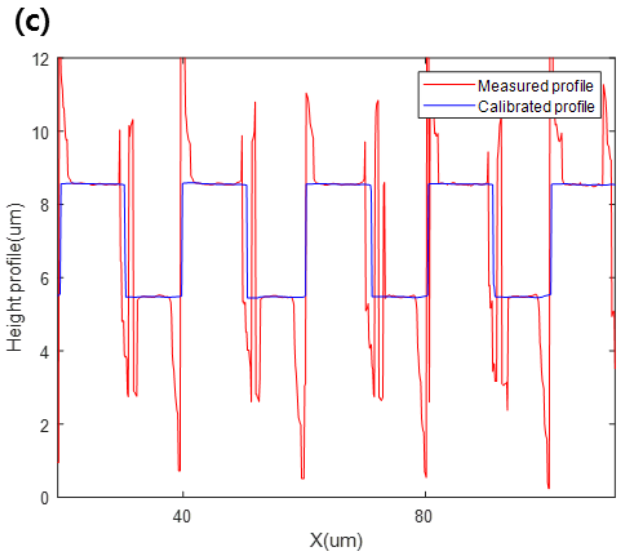

Figure 4.12 Edge calibration by median filter (grid structure); [25 × 25] median filter is applied.

4.5. Step height measurement of sample after 3D reconstruction of the specimen

Leveling of the acquired 3D surface profile

After obtaining the 3D surface profile of the specimen through the 3D reconstruction, the leveling process of converting the plane into a horizontal plane should be carried out first considering the tilt of the specimen in order to measure the step height of the specimen. The HiLo technique applied in this study implements a 3D surface profile through vertical scanning using the PZT, so theoretically, the measurement results of the specimen should be parallel to the horizontal direction. However, in practice, as shown in Figure 4.13, when the specimen is placed in the stage of the measuring device, the microscopic slope of the stage is unintentionally included. In the state including the inclination, it is impossible to simply regard the $z_i(x_i, y_i)$ as the height information at a specific point (x_i, y_i), and it is necessary to level the measurement results in parallel with the x-y plane and acquire the height information through an appropriate algorithm.

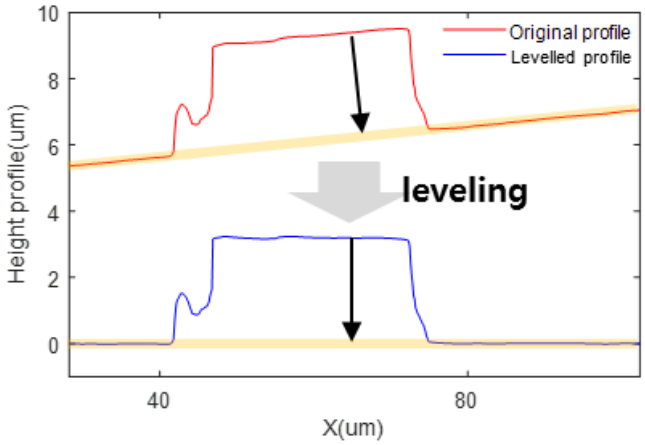

Figure 4.13 Illustration of surface profile leveling

In case of 3D surface profile, it is necessary to correct the measured data in parallel with the x-y plane by correcting the tilt in the 3D coordinate system since tilting occurs in each axis direction of x, y and z. As shown in Figure 4.14, we find the plane $ax+by+cz+d=0$ corresponding to the approximate value by fitting the each (x, y, z) information of the measured surface profile, and calculate the angle θ between the normal vector $\vec{\upsilon}=(a,b,c)$ of the plane and the unit normal vector $\vec{k}=(0,0,1)$ of x-y plane. After θ is found, the data can be converted to a value parallel to the x-y plane by rotating the plane by θ.

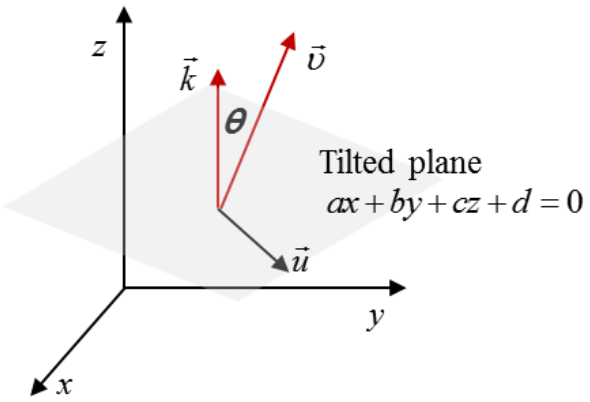

Figure 4.14 3D plane equation and normal vector of the plane

To obtain the fitted plane $ax+by+cz+d=0$ using the measured information of (x,y,z), we can try calculating the least square plane of all values of (x,y,z). That is, it is possible to obtain the constant value (a,b,c,d) of the least square plane by calculating when the sum of the squares of the distances h_i between the respective measured points (x_i,y_i,z_i) and the plane becomes minimum [47]. This method is suitable for observing the overall tendency of the measured values. However, when the measured values of the different

regions are mixed as in the case of measuring the height difference of the sample, it is difficult to calculate the plane as the measurement data need to be allocated to each region. For this reason, when measuring the height difference of the specimen, it is more appropriate to obtain three points that can be regarded to be on the same plane as shown in Figure 4.15 rather than using the least square method. More specifically, the plane passing through three points (x_1, y_1, z_1), (x_2, y_2, z_2) and (x_3, y_3, z_3) is given by Cramer's rule [48] and can be expressed as Eq. (4.10).

$$ax + by + cz + d = 0 \tag{4.10}$$

$$\text{where, } a = \det\begin{pmatrix} 1 & y_1 & z_1 \\ 1 & y_2 & z_2 \\ 1 & y_3 & z_3 \end{pmatrix}, \quad b = \det\begin{pmatrix} x_1 & 1 & z_1 \\ x_2 & 1 & z_2 \\ x_3 & 1 & z_3 \end{pmatrix},$$

$$c = \det\begin{pmatrix} x_1 & y_1 & 1 \\ x_2 & y_2 & 1 \\ x_3 & y_3 & 1 \end{pmatrix}, \quad d = -\det\begin{pmatrix} x_1 & y_1 & z_1 \\ x_2 & y_2 & z_2 \\ x_3 & y_3 & z_3 \end{pmatrix}$$

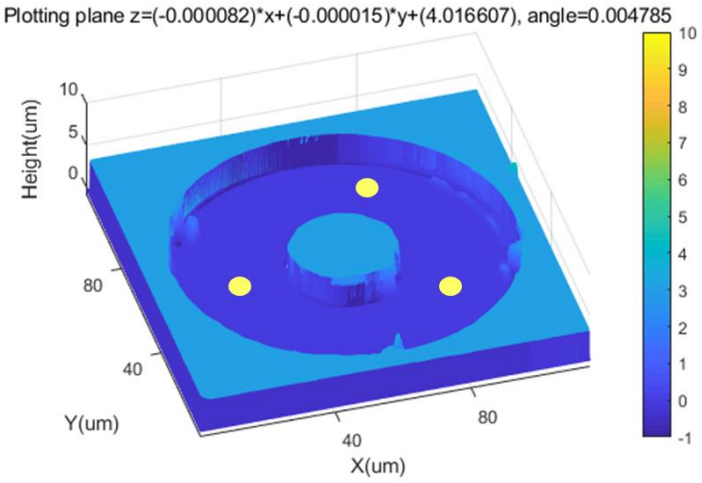

Figure 4.15 Levelled plane with 3 measurement data (yellow dots)

After acquiring a leveled plane passing through three points, the process of rotation conversion to the x-y plane is performed using the normal vector $\vec{\upsilon} = (a,b,c)$ of this plane. In Figure 4.14, the angle θ between the normal vector of the plane $\vec{\upsilon}$ and the normal vector of the x-y plane $\vec{k} = (0,0,1)$ can be expressed as Eq. (4.11).

$$\cos\theta = \frac{\left(\vec{\upsilon},\vec{k}\right)}{|\vec{\upsilon}|} = \frac{c}{\sqrt{a^2+b^2+c^2}},\ \sin\theta = \sqrt{\frac{a^2+b^2}{a^2+b^2+c^2}} \tag{4.11}$$

The cross product $\vec{u}$ of the two normal vectors is

$$\vec{u} = \frac{\vec{\upsilon}\times\vec{k}}{|\vec{\upsilon}|} = \frac{c}{\sqrt{a^2+b^2+c^2}}\left(b,-a,0\right)^T = (u_1,u_2,0)^T \tag{4.12}$$

And the matrix that rotates the plane by θ with $\vec{u}$ as the rotation axis can be expressed as Eq. (4.13) [49].

$$R = \begin{pmatrix} \cos\theta + u_1^2(1-\cos\theta) & u_1u_2(1-\cos\theta) & u_2\sin\theta \\ u_1u_2(1-\cos\theta) & \cos\theta + u_2^2(1-\cos\theta) & -u_1\sin\theta \\ -u_2\sin\theta & u_1\sin\theta & \cos\theta \end{pmatrix} \tag{4.13}$$

The rotation-transformed plane can be expressed as $Cz + D = 0$, which is a plane offset by $-D/C$ in z-axis direction. Since the step height can be measured more conveniently when the z-axis height of the plane is changed to 0 at the same time as the rotation, the final transformed value is obtained by subtracting the offset $-D/C$ in z direction after the rotation transformation, as in Eq. (4.14).

$$\begin{pmatrix} x_{final,i} \\ y_{final,i} \\ z_{final,i} \end{pmatrix} = R \begin{pmatrix} x_i \\ y_i \\ z_i \end{pmatrix} + \begin{pmatrix} 0 \\ 0 \\ D/C \end{pmatrix} \quad (4.14)$$

When θ is very small, *i.e.* < 1 degree, there is little difference in height z between rotation conversion and projection in z direction. For example, if there is a tilt of 1 degree, a distance error of 0.015 % occurs between the tilt plane, the shortest distance and the z-axis distance, which corresponds to an error of 0.15 *nm* per height step of 1 μm. As this is a very small value compared to the z-direction resolution of HiLo technique, projecting in the z-axis direction without rotating the 3D surface profile does not cause a significant error in the measurement results. Therefore, in this study, when the tilt value of the specimen is relatively small (<1 degree), the measurement value is leveled by using the z-axis projection instead of the rotation conversion.

Step height measurement of the specimen

We measured the step height of 3D surface profile after leveling. However, merely comparing the z values between specific points of a measuring device is not an appropriate method in view of errors in image acquisition and processing. It is more reasonable to select a specific area around the two points to be measured and to regard the average value as the height of the point. In this study, we used a method of automatically selecting 30 × 30 square areas centered on selected points or selecting a region of interest (ROI) as shown in Figure 4.16.

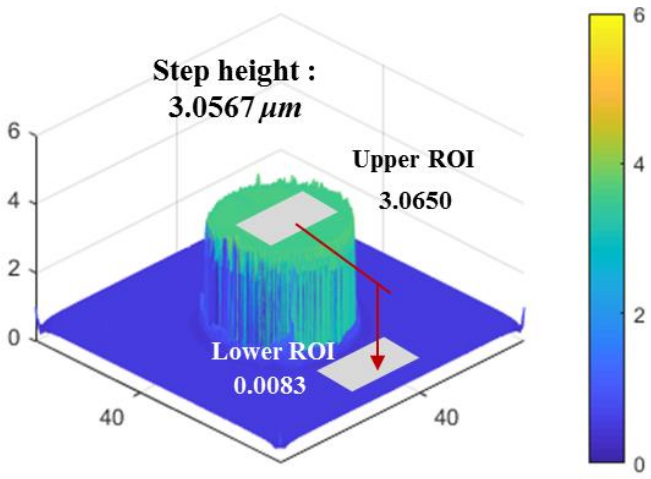

Figure 4.16 Step height measurement with mean value of 2 ROIs; measured by LSCM, objective lens 50× *NA* = 0.95, the specimen is the standard sample (AFM result is 3.0007 μm)

Precision of the step height measurement and height calibration with standard sample

Once the shape calibration of the 3D surface profile is completed, it is necessary to test the precision of measured height information using repeatability test. The same sample can be repeatedly measured and the standard deviation of the measured values can be obtained to confirm the precision and error rate of the measured value, which should be presented as a performance index of the measuring device. For this reason, a standard sample with height step of 3.0007 μm measured by AFM was measured 12 times using HiLo technique. The average value and standard deviation were calculated as 3.0454 μm and 0.0213 μm, respectively, as shown in Table 11. This means that when the step height is measured using HiLo technique, it is within 64 *nm* on the basis of 3σ at 95% reliability.

Table 11. Repeatability test of height measurement with standard sample (step height of the sample measured by AFM is 3.0007 μm)

	Top surface	Bottom surface	Step height
Average	**3.0504**	**0.0050**	**3.0454**
Std. deviation (σ)	**0.0222**	**0.0040**	**0.0213**
3 σ	**0.0666**	**0.012**	**0.0639**
1	3.0716	0.0044	3.0672
2	3.0416	0.001	3.0406
3	3.0551	0.0027	3.0524
4	3.1012	0.0055	3.0957
5	3.0318	0.0043	3.0275
6	3.0414	0.0032	3.0382
7	3.0047	0.0018	3.0029
8	3.0453	0.0122	3.0331
9	3.0621	0.0099	3.0522
10	3.0571	0.0113	3.0458
11	3.0494	0.0047	3.0447
12	3.0435	-0.0014	3.0449

In addition, as shown in Table 11, the height step of the standard sample was measured as 3.0454 μm . This is 1.469% larger than the value measured by AFM (3.0007 μm). Therefore, when measuring the actual specimen, the height profile measured by HiLo should be reduced by 1.469%. In the same way, utilizing the measurement results obtained in Chapter 4.3, the step height measured by LSCM was also corrected by 1.890 %.

4.6. Selected sample measurement result and comparison to LSCM

The performance of HiLo imaging technique for measuring a 3D surface profile was verified by using actual samples and comparing to the result from a commercially available LSCM (Olympus OLS 4100, Olympus, Inc., Japan) with the same objective lens (50×, *NA* = 0.95, MPLAPON50X, Olympus, Inc., Japan). For comparison, we selected three stepped, circle, and grid structures from a standard sample with accurate height information through AFM. We also selected one additional MEMS rectangular well structure. As suggested in Chapter 4. 5, leveling is performed and the appropriate ROI is chosen to calculate the average of the top and bottom surfaces to calculate the step height. In addition, height calibration was applied to both HiLo and LSCM.

In Figure 4.17 ~ Figure 4.20, the 3D profile of the image acquired by HiLo optical imaging technique is presented, and compared to the result from LSCM.

Figure 4.17 shows the result of measuring the edge part of the standard sample. The 3D profile of the image acquired by HiLo optical imaging technique is presented in Figure 4.17(c), and compared to the result from LSCM (Figure 4.17(b)). We confirmed that both HiLo and LSCM can reconstruct the same profile. The step height measured with LSCM and HiLo were 3.0016 μm and 2.9999 μm, respectively, and the difference was within 10 *nm*. Considering the measurement errors of LSCM (13 *nm*) and HiLo (21 *nm*), it is confirmed that the measurement results of the two methods are at equivalent level.

Figure 4.18 shows the result of measuring the circle structure in the same standard sample. The step height was 2.999 μm and 3.0002 μm for LSCM and HiLo, respectively, and the

difference was within 10 *nm*. As a circle type sample was used, the influence of the angle of the grating can be examined, and it was be confirmed that the influence of the angle is insignificant.

Figure 4.19 shows the result of measuring the grid structure in the same standard sample. Based on the top surface, the grid width and grid gap are equal to 10 μm. In contrast to the results of edge and circle measurements, it can be seen that the step height is larger in both LSCM and HiLo than AFM measurement results. This could be due to the shape of the sample or the errors in the height calibration method. Further studies are needed to obtain more accurate height information and enhance performance.

Figure 4.20 shows the measurement result of a MEMS rectangular well made by lithography. The designed rectangular size on the top surface was 250 μm by 85 μm and designed depth of well was 0.72 μm. It can be confirmed that the measured shape and height profile was almost the same as the designed shape and the measured result from LSCM. And the measured height is 2.3% larger than design height; this seems to be due to a combination of manufacturing error and measurement error.

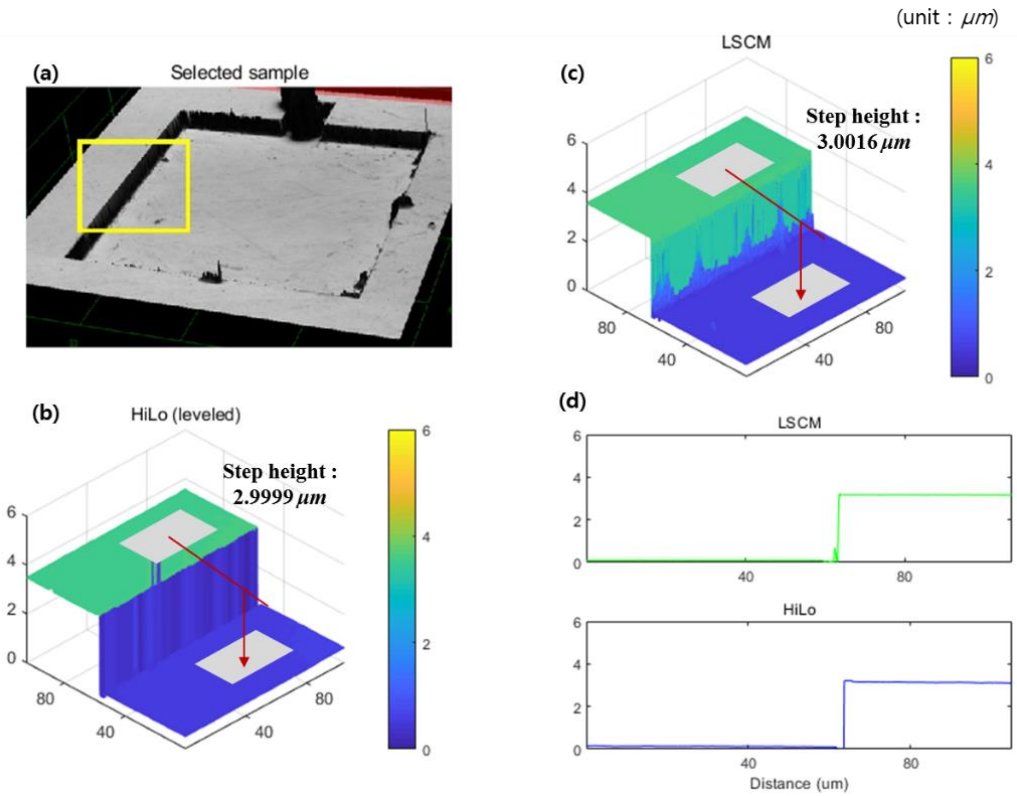

Figure 4.17 Result of 3D surface profile measurement of (a) edge of standard sample, acquired by (b) HiLo and (c) LSCM; (d) height profiles of both techniques

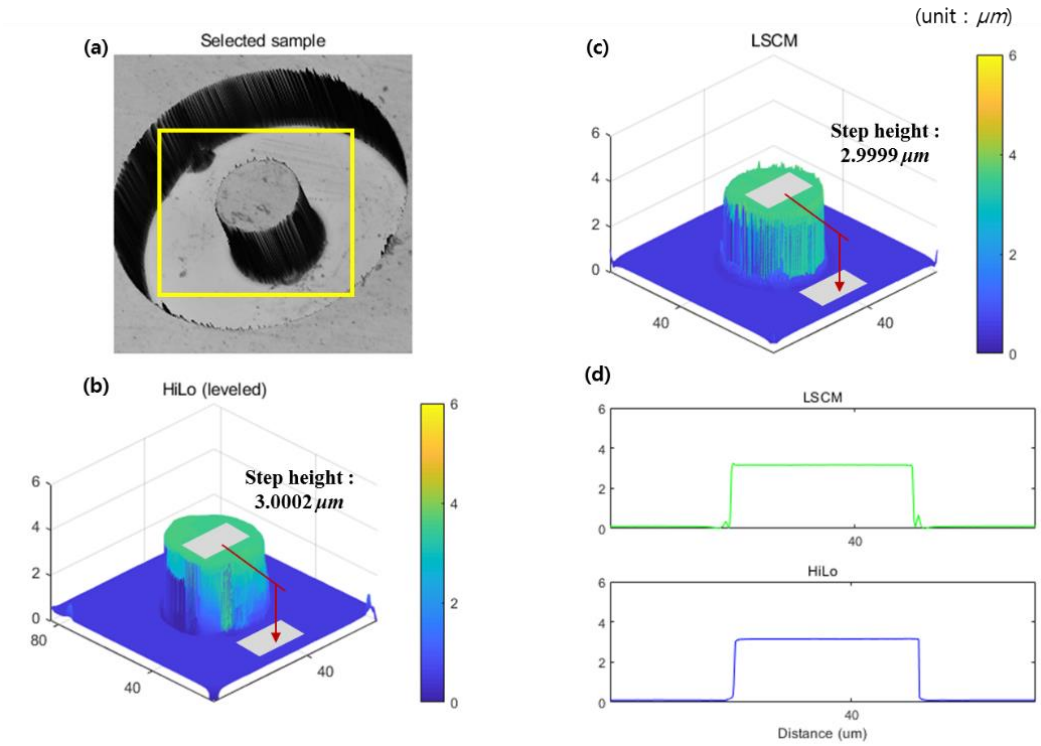

Figure 4.18 Result of 3D surface profile measurement of (a) circular structure of standard sample, acquired by (b) HiLo and (c) LSCM; (d) height profiles of both techniques

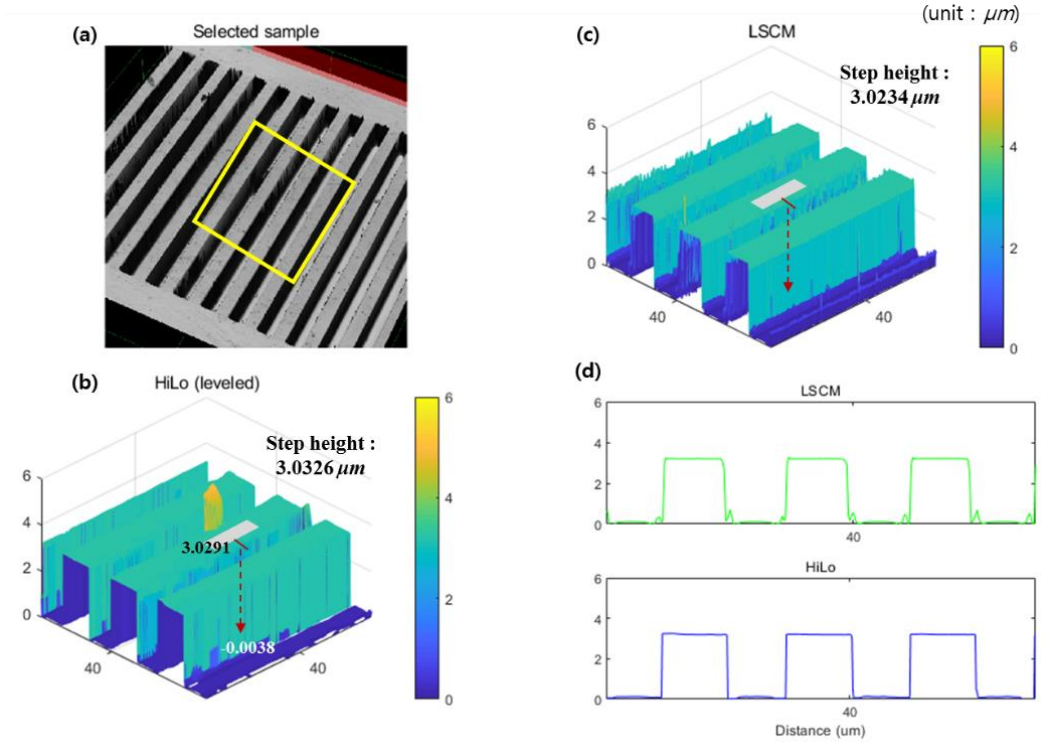

Figure 4.19 Result of 3D surface profile measurement of (a) grid structure of standard sample, acquired by (b) HiLo and (c) LSCM; (d) height profiles of both techniques

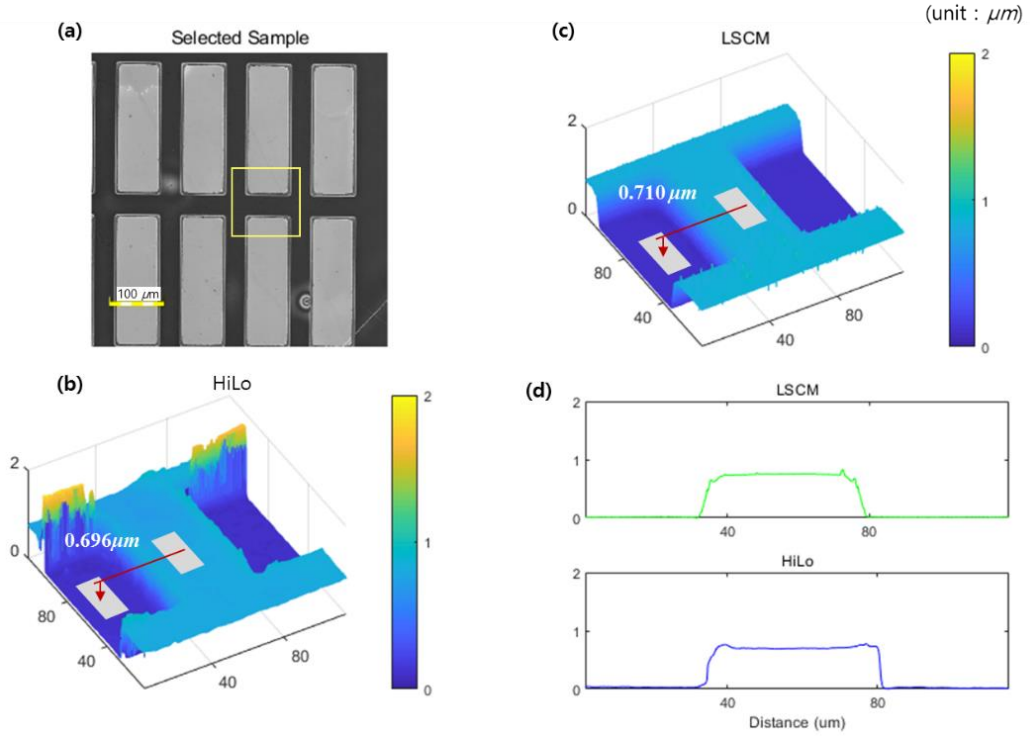

Figure 4.20 Result of 3D surface profile measurement of (a) mems rectangular well acquired by (b) HiLo and (c) LSCM; (d) height profiles of both techniques.

4.7. Summary and discussion

Chapter 4 describes how to reconstruct the 3D surface profile by using HiLo and dual-wavelength HiLo image stack acquired while moving the focus position at regular intervals in the z axis direction.

In order to find the z-point corresponding to the surface of the specimen at a specific *(a, b)* position in the image stack, we applied an algorithm that recognizes the brightest position in the z-direction in the image stack as the height. This is basically the same as the technique applied in focus-variable microscopy (or shape from focus) and is similar to the way LSCM determines the surface position. In addition, to minimize the influence of the z-step movement interval, we added an algorithm that approximates the position of the actual surface plane by curve fitting around the measured intensity peak point.

In order to verify 3D surface reconstruction performance using HiLo technique, the precision, which is the most important performance factor of surface profiler, was confirmed by repeatability test. The repeatability varies with the grating period, and the larger the grating period, the smaller the standard deviation of the measurement results. However, considering that the axial direction FWHM becomes larger as the grating period increases (Chapter 2.5, Chapter 3.4), the optimum value of the grating period was determined as 25 μm.

It is difficult to say that the acquired 3D surface profile itself reflects the actual shape of the specimen. This is a result of a combination of the aberration of the optical system itself, the fine alignment error of the optical system, the tilting of the stage, the non-uniformity of the light source, etc., and need to be corrected through the post-processing process so

as to express the shape and size of the actual sample. In this study, surface flatness, outlier elimination, and height matching were performed using a standard sample with a verified shape and size.

The surface flatness was corrected by measuring the standard sample 10 times repeatedly, designating the average value as a reference value, and subtracting this value from the calculation result of the 3D surface profile of the actual sample. In the case of outlier elimination, it is possible to mitigate the phenomenon that accurate measurements are not obtained due to diffuse reflection especially at the edges of the specimen. In this study, outliers were removed by applying median filter. In addition, various filtering techniques specified in ISO 16610 standard can be applied for performance comparison. Finally, height calibration was performed by comparing the AFM result of the standard sample with the height difference of the sample derived from HiLo technique, and adjusting it to be the same as the AFM result.

The 3D surface profile was obtained by measuring the actual sample and compared with the measurement results of commercial LSCM. It was confirmed that the same shape as LSCM was obtained, and the measured height value was the same value with LSCM within 1%.

In addition, the ability to measure inclined surfaces was tested using real samples. In the case of the smooth surface, the measurement of the inclined plane at the level of 13 degrees using the protected silver mirror was performed without difficulty, but failed to derive an appropriate result for the mirror with the inclination of 45 degrees. This is because only a very small number of grating patterns are totally incident on the objective lens due to the total reflection at high angled slopes, and thus the corresponding signal is

lost in HiLo image processing. It was confirmed that the measurement capability of the inclined surface is lower than that of the LSCM.

On the other hand, in the case of a rough surface, it was possible to measure a slope at a comparatively high angle. It can be interpreted that signals are not lost in HiLo image processing since a relatively large amount of reflected light is incident on the objective lens due to the diffuse reflection on the surface.

CHAPTER 5.

SUMMARY AND DISCUSSION

With the development of micro and nanotechnology, the demand for 3D measurement of microstructures is also increasing. 3D measuring devices are largely classified into a contact type and non-contact type, and the latter is preferred because of the measurement speed and the contamination of the sample. The non-contact type is again divided into an electron microscope and a visible light microscope depending on the wavelength used. In the visible light region, AFM, WLI, LSCM, and SIM are mainly used. However, the above-mentioned microscopes have various constraints such as long measurement time, expensive laser equipment, limited measurement area, and the like. Considering such constraints, the goal of this study was set to develop a 3D measurement technique capable of wide-field imaging with vertical resolution comparable to a LSCM and high measurement speed without the use of expensive equipment such as a laser.

HiLo imaging technique, introduced in 2008 in the field of fluorescence imaging, is a technique for acquiring images with 3D resolution by signal processing two wild-field fluorescence images with pattern filters. This technology, which is based on wide-field imaging, has the advantage that it is very fast compared with the laser scanning method of a conventional three-dimensional fluorescence LSCM and maintains a comparable level with the conventional three-dimensional resolution.

Since its introduction, HiLo imaging technique has been applied only in the field of fluorescence imaging, and its application to the measurement of the reflected light on the 3D surface is examined for the first time in this study.

In Chapter 2, to verify HiLo imaging technique, the theoretical background of HiLo imaging technique was reconstructed in accordance with the reflected light measurement of the surface. The experimental device was constructed using the general optical components and the self-manufactured parts, and the software algorithm was implemented. The performance was verified by using the standard sample with the proven shape and height and it confirmed that the same horizontal and vertical brightness distribution as the fluorescence image can be obtained even when the reflected light of the target surface is measured. This means that HiLo technique can be applied even when the reflected light of the surface is measured. In addition, it was confirmed that the vertical resolution is improved as the lattice spacing of the structured illumination filter, which is a core design parameter of HiLo imaging technique, is decreased.

Although HiLo imaging method is a high-speed imaging method capable of simultaneously imaging a large area, it takes 1 to 2 seconds to sequentially acquire two images along with the physical movement of the pattern filter and thus difficult to implement real-time imaging. An electronic pattern generator such as a spatial light modulator (SLM) or a digital micro-mirror device (DMD) can be used to suppress the physical movement of the pattern filter to improve the speed, but sequential image acquisition poses as a fundamental limitation.

In Chapter 3, we proposed a dual-wavelength HiLo imaging technique to fundamentally overcome the sequential image acquisition of HiLo imaging.

The dual-wavelength HiLo method is a method that realizes two images simultaneously by using two light sources with different wavelengths. Unlike the fluorescent dyeing field in which the wavelength band of the output light is fixed irrespective of the wavelength of the incident light depending on the characteristics of the dye, the reflected light of the same wavelength range as that of the incident light can be separately detected.

First, a structural contrast pattern is disposed only on the optical path of one of the two light sources having different wavelengths to generate a structured contrast light source and a uniform contrast light source, respectively. The two generated light sources were simultaneously imaged on the sample, and two video signals were acquired simultaneously using two cameras equipped with a band-pass filter so that the reflected light of the sample could pass through only the light of each light source. In this way, it is possible to simultaneously acquire two images required for HiLo technique without physical movement of the pattern filter, and the conventional HiLo image acquisition time of 1 to 2 seconds could be shortened to real time.

In addition to hardware changes, we have proposed and applied a software technique to compensate for image errors due to the use of light sources of different wavelengths. In order to correct the aberration due to the wavelength difference, the size of the image was adjusted to reflect the change of the focal length according to the difference in the refractive index of the lens, and the fine position error of the two cameras was corrected. We compared the results of the dual-wavelength HiLo imaging method with those of the conventional HiLo, and found that they have the same horizontal and vertical resolution.

In Chapter 4, images acquired through HiLo and dual-wavelength HiLo are reconstructed into a 3D surface profile and compared with commercial LSCM.

The 3D surface profile reconstruction algorithm is proposed using HiLo and dual-wavelength HiLo images obtained by moving the objective lens at regular intervals in the vertical direction. The 3D surface profile obtained through the proposed algorithm shows a measurement accuracy of 50 *nm* level through the repeatability test. In addition, the process of acquiring the final 3D image through a preprocessing step for aligning the 2D image stack, a 3D reconstruction step for determining the position of the surface based on the brightness information, a post-processing process for flatness calibration, outlier elimination, and height calibration of the obtained 3D surface profile is explained.

Comparing the results with commercial LSCM, it was confirmed that the same or similar level shape and measurement result value can be obtained with dual-wavelength HiLo.

Although we confirmed the feasibility of using the dual-wavelength HiLo imaging technique in this study, there still remain areas for further improvement.

First, we need to find a way to reduce overshooting and undershooting at the edge, which is commonly called the bat-wing effect. A number of studies have introduced techniques to eliminate the batwing effect, and the median filter was chosen and applied in this study. However, applying the median filter results in the removal of the surface roughness information from parts other than the edge. Therefore, it is necessary to develop a better technique for selectively eliminating the batwing effect only at the edge.

Second, it is necessary to develop theoretical analysis and to improve measurement technique for high angle slope measurement. Especially for a smooth surface, the actual measurable range within the theoretically measurable slope angle is very narrow. It is necessary to establish the rationale to explain this phenomenon and to derive the maximum measurement angle for the smooth surface.

Third, although the image acquisition time is shortened by eliminating the physical movement of the pattern filter through the dual-wavelength HiLo, there is still a limitation in acquiring real-time HiLo images due to the time-consuming software processing such as HiLo processing and 3D reconstruction. In addition to developing more optimized algorithms at each step, software optimization tasks such as changing codes to utilize the GPU should be performed.

Despite the need for additional research and improvement, the proposed dual-wavelength HiLo technique can be expected to be an appropriate alternative to LSCM technology in terms of resolution and speed. In particular, it is necessary to pay attention to the fact that it is highly competitive in terms of the economy. Reflected LSCM usually costs more than 1 million US dollars, depending on the performance of the mounted laser. In contrast, the dual-wavelength HiLo technique can be implemented at a low cost of 10,000 to 20,000 US dollars by using a conventional optical microscope body and a commercial CCD camera.

REFERENCES

[1] F. Chen, G. M. Brown, and M. Song, "Overview of three-dimensional shape measurement using optical methods," *Opt. Eng.*, vol. 39, no. 1, pp. 10–22, 2000.

[2] D. R. Lee, Y. D. Kim, D. G. Gweon, and H. Yoo, "High speed 3D surface profile without axial scanning: Dual-detection confocal reflectance microscopy," *Meas. Sci. Technol.*, vol. 25, no. 12, 2014.

[3] John Kuo, Ed., *Electron microscopy: Methods and protocols*, Third Edit. Humana Press, Totowa, NJ, 2014.

[4] D. B. Williams and C. B. Carter, *Transmission Electron Microscopy*. 2009.

[5] K D Vernon-Parry, "Scanning electron microscopy : an introduction," *III-Vs Rev.*, vol. 13, no. 4, pp. 40–44, 2000.

[6] E. Meyer, "Atomic force microscopy," *Prog. Surf. Sci.*, vol. 41, no. 1, pp. 3–49, 1992.

[7] G. Zeng, Y. Duan, F. Besenbacher, and M. Dong, "Nanomechanics of Amyloid Materials Studied by Atomic Force Microscopy," *At. Force Microsc. Investig. into Biol. - From Cell to Protein*, no. May 2014, 2012.

[8] Richard Leach, Ed., *Optical Measurement of Surface Topography*, 1st ed. Springer-Verlag Berlin Heidelberg, 2011.

[9] E. McLeod and A. Ozcan, "Unconventional methods of imaging: Computational microscopy and compact implementations," *Reports Prog. Phys.*, vol. 79, no. 7, 2016.

[10] N. Múnera, G. J. Lora, and J. Garcia-Sucerquia, "Evaluation of fringe projection and laser scanning for 3D reconstruction of dental pieces | Evaluación de

proyección de franjas y escaneo láser para la reconstrucción 3D de piezas dentales," *DYNA*, vol. 79, no. 171, pp. 65–73, 2012.

[11] P. Giacomo, "The Michelson interferometer," *Mikrochim. Acta*, vol. 93, no. 1–6, pp. 19–31, 1987.

[12] P. Lehmann, S. Tereschenko, and W. Xie, "Fundamental aspects of resolution and precision in vertical scanning white-light interferometry," *Surf. Topogr. Metrol. Prop.*, vol. 4, no. 2, 2016.

[13] D. Lim, K. K. Chu, and J. Mertz, "Wide-field fluorescence sectioning with hybrid speckle and uniform-illumination microscopy.," *Opt. Lett.*, vol. 33, no. 16, pp. 1819–1821, 2008.

[14] J. Mertz, "Optical sectioning microscopy with planar or structured illumination," *Nat. Methods*, vol. 8, no. 10, pp. 811–819, 2011.

[15] D. Lim, T. N. Ford, K. K. Chu, and J. Mertz, "Optically sectioned in vivo imaging with speckle illumination HiLo microscopy," *J. Biomed. Opt.*, vol. 16, no. 1, p. 016014, 2011.

[16] T. N. Ford, D. Lim, and J. Mertz, "Fast optically sectioned fluorescence HiLo endomicroscopy," *J. Biomed. Opt.*, vol. 17, no. 2, p. 021105, 2012.

[17] S. Santos *et al.*, "Optically sectioned fluorescence endomicroscopy with hybrid-illumination imaging through a flexible fiber bundle," *J. Biomed. Opt.*, vol. 14, no. 3, p. 030502, 2009.

[18] E. Muro *et al.*, "Single-shot optical sectioning using two-color probes in HiLo fluorescence microscopy," *Biophys. J.*, vol. 100, no. 11, pp. 2810–2819, 2011.

[19] D. Bhattacharya *et al.*, "Three dimensional HiLo-based structured illumination for a digital scanned laser sheet microscopy (DSLM) in thick tissue imaging," *Opt.*

Express, vol. 20, no. 25, pp. 27337–27347, 2012.

[20] S. K. Nayar and Y. Nakagawa, "Shape from Focus," *IEEE Trans. Pattern Anal. Mach. Intell.*, vol. 16, no. 8, pp. 824–831, 1994.

[21] M. Peikari, T. K. Chen, and A. Lasso, "Medical Image Computing and Computer-Assisted Intervention – MICCAI 2011," vol. 6892, no. May 2014, 2011.

[22] M. A. A. Neil, R. Juškaitis, and T. Wilson, "Method of obtaining optical sectioning by using structured light in a conventional microscope," *Opt. Lett.*, vol. 22, no. 24, p. 1905, 1997.

[23] T. Wilson, "Resolution and optical sectioning in the confocal microscope," *J. Microsc.*, vol. 244, no. 2, pp. 113–121, 2011.

[24] P. A. Stokseth, "Properties of a Defocused Optical System*," *J. Opt. Soc. Am.*, vol. 59, no. 10, p. 1314, Oct. 1969.

[25] D. Dan, B. Yao, and M. Lei, "Structured illumination microscopy for super-resolution and optical sectioning," *Chinese Sci. Bull.*, vol. 59, no. 12, pp. 1291–1307, 2014.

[26] H. L. Fu *et al.*, "Optimization of a Widefield Structured Illumination Microscope for Non-Destructive Assessment and Quantification of Nuclear Features in Tumor Margins of a Primary Mouse Model of Sarcoma," *PLoS One*, vol. 8, no. 7, 2013.

[27] B. Christoffer Lagerholm, S. Vanni, D. Lansing Taylor, and F. Lanni, "Cytomechanics applications of optical sectioning microscopy," *Methods Enzymol.*, vol. 361, pp. 175–197, Jan. 2003.

[28] F. Lanni, "Grating imager systems for fluorescence optical-sectioning microscopy," *Cold Spring Harb. Protoc.*, vol. 2014, no. 9, pp. 923–931, 2014.

[29] C. A. Schneider, W. S. Rasband, and K. W. Eliceiri, "NIH Image to ImageJ: 25

years of image analysis," *Nat. Methods*, vol. 9, p. 671, Jun. 2012.

[30] Daryl Lim, "HiLo ImageJ Plugin (version 1.2)," 2013. [Online]. Available: http://biomicroscopy.bu.edu/resources/4.

[31] G. Bradski, "The OpenCV Library," *Dr. Dobb's J. Softw. Tools*, 2000.

[32] C. J. Sheppard and M. Gu, "Aberration compensation in confocal microscopy.," *Appl. Opt.*, vol. 30, no. 25, pp. 3563–3568, 1991.

[33] I. Escobar, G. Saavedra, and M. Martínez-corral, "Reduction of the spherical aberration effect in high-numerical-aperture optical scanning instruments," *America (NY).*, vol. 23, no. 12, pp. 3150–3155, 2006.

[34] D. Dan *et al.*, "DMD-based LED-illumination Super-resolution and optical sectioning microscopy," *Sci. Rep.*, vol. 3, pp. 1–7, 2013.

[35] B. E. A. Saleh and M. C. Teich., *Fundamentals of photonics*, 2nd editio. Hoboken, N.J. : Wiley Interscience, 2007.

[36] Pedrotti, *Introduction to Optics*, 3rd editio. Pearson Education, 2007.

[37] S. H. Song, "Aberration Theory," *http://optics.hanyang.ac.kr/~shsong/20-Aberration theory.pdf*. [Online]. Available: http://optics.hanyang.ac.kr/~shsong/20-Aberration theory.pdf.

[38] P. Thevenaz and M. Unser, "A pyramid approach to sub-pixel Registration Based on Intensity," *IEEE Trans. IMAGE Process.*, vol. 7, no. 1, pp. 27–41, 1998.

[39] W. Y. Hsu, "Analytic differential approach for robust registration of rat brain histological images," *Microsc. Res. Tech.*, vol. 74, no. 6, pp. 523–530, 2011.

[40] B. B. Avants, M. Grossman, and J. C. Gee, "Symmetric Diffeomorphic Image Registration: Evaluating Automated Labeling of Elderly and Neurodegenerative Cortex and Frontal Lobe," in *Biomedical Image Registration*, 2006, pp. 50–57.

[41] R. G. Keys, “Cubic Convolution Interpolation for Digital Image Processing,” *IEEE Trans. Acoust.*, vol. 29, no. 6, pp. 1153–1160, 1981.

[42] Z. Xie, Y. Tang, Y. Zhou, and Q. Deng, “Surface and thickness measurement of transparent thin-film layers utilizing modulation-based structured-illumination microscopy,” *Opt. Express*, vol. 26, no. 3, p. 2944, 2018.

[43] S. Pertuz, D. Puig, and M. A. Garcia, “Analysis of focus measure operators for shape-from-focus,” *Pattern Recognit.*, vol. 46, no. 5, pp. 1415–1432, 2013.

[44] M. Fauzi Ismail, K. Yanagi, and A. Fujii, “An outlier correction procedure and its application to areal surface data measured by optical instruments,” *Meas. Sci. Technol.*, vol. 21, no. 10, 2010.

[45] H. Jeong, H. Yoo, and D. Gweon, “High-speed 3-D measurement with a large field of view based on direct-view confocal microscope with an electrically tunable lens,” *Opt. Express*, vol. 24, no. 4, p. 3806, 2016.

[46] ISO, *ISO 16610-1:2015 Geometrical product specifications (GPS) – Filtration-Part 1: Overview and basic concepts*. 2015.

[47] D. Eberly, “Least Squares Fitting of Data by Linear or Quadratic Structures,” 2018. [Online]. Available: https://www.geometrictools.com/. [Accessed: 12-Dec-2018].

[48] J. H. Kwak and Sungpyo Hong, *Linear Algebra*, Second edi. Birkhäuser, Boston, MA, 2004.

[49] I. R. Cole, “Modelling CPV,” Loughborough University, 2015.

요약

마이크로 및 나노 기술의 발달에 따라, 미세구조의 3 차원 측정에 대한 요구 또한 증가하고 있다. 3 차원 측정 장치는 크게 접촉식과 비 접촉식으로 구분되며, 측정 속도, 시료의 오염 등의 이유로 비접촉식이 선호되고 있다. 비 접촉식은 다시 파장의 크기에 따라 전자현미경과 가시광선 현미경으로 구분되는데, 가시광선 영역에서는 원자 현미경, 백색광 간섭계, 레이저 스캐닝 공초점 현미경, 구조조영 현미경 등을 주로 활용한다. 그런데, 상기의 방법들은 측정 시간이 길거나, 고가의 레이저 장비가 필요하거나, 측정 영역이 제한 되는 등 각각의 제약 요소가 존재한다. 본 연구에서는, 이러한 제약 요소를 고려하여 대면적 촬영이 가능하여 측정 시간이 빠르고, 레이저 등 고가의 장비를 활용하지 않으면서, 레이저 스캐닝 공초점 현미경과 비견되는 수직방향 해상도를 가지는 3 차원 측정 기법을 개발하는 것을 목표로 하였다.

형광영상 분야에서 2008 년 소개된 HiLo 영상기법은 패턴필터가 적용된 2 장의 대면적 형광영상을 신호처리하여 3 차원 분해능을 가진 영상을 획득하는 기술이다. 대면적 영상을 기반으로 하는 이 기술은 기존의 3 차원 공초점 형광현미경의 레이저 주사방식에 비해 매우 빠르면서도 기존의 3 차원 해상도와 비교할 만한 수준을 유지하고 있다는 장점을 가지고 있다.

HiLo 영상 기법은 최초 소개된 이후 형광영상 분야에서만 적용되어 왔으며, 현재까지 3 차원 표면의 반사광을 측정하는 연구가 진행되지 않아 본 연구에서 그 가능성을 최초로 검토하였다. HiLo 영상 기법을 검증하기 위해 HiLo 영상 기법의 이론적 배경을 표면의 반사광 측정에 맞게 재구성하였으며, 범용 광학 부품과 자체 제작한 부품을 활용하여 실험 장치를 구성하였고, 소프트웨어 알고리즘을 구현하였다. 형상과 높이가 검증된 표준샘플을 활용하여 성능을 검증하였으며, 시료 표면의 반사광을 측정하는 경우에도, 형광영상과 동일한 수평 및 수직방향 밝기 분포를 획득할 수 있음을 확인하였다. 이와 함께, HiLo 영상 기법의 핵심 설계 변수인 구조조영 필터의 격자 간격을 변화시키면서 측정하여 최적 격자 간격을 도출하였다.

그런데, HiLo 영상 기법이 대면적을 동시에 촬영할 수 있는 고속 영상 기법임에도 불구하고, 패턴필터의 물리적 이동과 함께 순차적으로 2 개의 영상을 획득하는 과정에서 발생하는 시간 소요로 실시간 영상을 구현하기는 어렵다. Spatial light modulator (SLM) 또는 digital micro-mirror device (DMD) 등을 채택하여 속도를 개선시킬 수 있으나, 순차적 영상 획득이라는 근본적인 한계가 있다. 이 때문에, HiLo 영상 처리에 필요한 2 개의 영상을 동시에 획득할 수 있는 양파장 HiLo 영상 기법을 제안하였다. 이것은 염색물질의 특성에 따라 입사광의 파장과 무관하게 출력광의 파장대가 일정한 형광 염색 분야와 달리, 반사광을 측정하는 경우에는 다수 파장대의 입사광을 동시에 조영하여도 입사광과 동일한 파장대의 반사광을 분리 검출할 수 있다는 점에 착안하였다..

먼저, 서로 다른 파장을 가지는 2 개의 광원 중 1 개 광원의 광 경로에만 구조조영 패턴를 배치하여 구조조영 광원과 균일 조영 광원을 각각 생성하였다. 생성된 2 광원을 동시에 시료에 조영한 후, 시료의 반사광을 각 광원의 파장대의 빛만 통과시키도록 band-pass filter 가 설치된 2 대의 카메라를 활용해 2 개의 영상을 동시에 획득하도록 하였다. 상기 방법으로 패턴 필터의 물리적 이동 없이 HiLo 기법에 필요한 2 개의 영상을 동시에 획득할 수 있게 되어, 1~2 초 수준의 기존 HiLo 영상 획득 시간을 실시간으로 단축할 수 있었다.

이때, 서로 다른 파장의 광원과 2 개의 카메라를 사용하는 것을 고려하여 기존 HiLo 영상 처리 방법을 일부 수정하였다. 파장 별 렌즈 초점거리 차이를 보정하였고, 동시에, 2 개 카메라의 미세한 정렬 오차를 소프트웨어적으로 보정하였다. 기존 HiLo 영상 기법과 동일한 시료를 측정한 결과와 양파장 HiLo 를 통해 측정한 결과를 비교한 결과 기존 HiLo 와 동일한 수준의 수평, 수직방향 해상도를 가짐을 확인하였다.

본 연구에서는 또한, 수직 방향으로 일정 간격으로 대물렌즈를 이동시키면서 획득한 HiLo 및 양파장 HiLo 이미지들의 활용해 3 차원 표면 프로파일을 재구성하는 알고리즘을 제시하였다. 적층한 2 차원 영상을 정렬하는 전처리 단계, 밝기 정보에 기반하여 표면의 위치를 결정하는 3 차원 재구성 단계, 획득한 3 차원 프로파일의 평평도 및 측정 오차를 보정하여 최종 영상을 획득하는 단계를 거치게 된다.

반복성 테스트를 통해 20 *nm* 수준의 측정 정밀도를 보임을 확인하였으며, 다수 샘플 측정 결과 상용 레이저 스캐닝 공초점 현미경과 동일 또는 유사한 수준의 형상과 측정 결과값을 획득할 수 있음을 확인하였다.

주요어 : 3D 프로파일, HiLo 영상 기법, 양파장 HiLo 영상 기법, 구조 조영, 고속 영상,

학　번 : 2000-30646

감사의 글

오랜 시간이 걸렸습니다. 2002 년 수료 후 사회생활을 하면서도 늘 미완성에 대한 아쉬움이 있었는데, 좋은 인연을 만나 2014 년부터 연구를 재개할 수 있었고 이제서야 마침표를 찍게 되었습니다. 그 과정에서 너무나 많은 분들의 격려와 도움이 있었습니다. 모든 분들께 감사 인사 올립니다.

지도 학생 중 유일하게 졸업하지 못한 못난 제자를 늘 격려해 주시고 걱정해 주신 고상근 교수님께 깊은 감사의 말씀을 올립니다. 여러 가지 전례가 없는 형태로 연구를 진행했음에도 그 모든 것을 허락해 주시고 적극 지지해 주셨기에 무사히 과정을 마칠 수 있었던 것 같습니다.

김대근 교수님, 감사합니다. 연구의 주제와 방향, 연구 인프라 모든 면에서 전폭적으로 지원해주시고 이끌어 주셨습니다. 지난 5 년간의 시간이 너무나 소중했습니다. 앞으로 5 년 10 년 그리고 그 이후에도 소중한 인연이 계속 이어질 수 있도록 노력하겠습니다.

심사과정에서, 졸고를 우호적이고 따뜻한 시선으로 바라봐 주시고 바른 방향으로 갈 수 있도록 지도를 아끼지 않으셨던 박희재 교수님과 고승환 교수님, 임시형 교수님께도 진심으로 감사 드립니다. 미처 고려하지 않았거나 미진했던 많은 부분을 심사 과정에서 보완할 수 있었던 것 같습니다.

많은 관심과 조언과 도움을 아끼지 않았던 멋진 동기 이정철 교수, 좋은 인연을 만들어준 박선호 교수께도 감사 드립니다. 그리고, 늙다리 아저씨와 같이 생활해 준 실험실 동료들 인건이, 은우, 호진이, 예현이, 재현이, 상원이 모두 고맙습니다. 동료들 무사히 졸업할 수 있도록 적극 돕겠습니다.

사랑하는 가족들, 고맙습니다. 가족들이 있기에 이 모든 일들을 할 수 있었습니다. 연구를 이유로 대부분의 시간을 함께하지 못했음에도, 싫은 내색 없이 잘 다녀오라고 힘내서 열심히 하라고 응원해 줬던 두 딸 지운이와 영운이가 너무나 고맙고 자랑스럽습니다. 잘하고 있다고 항상 응원해 주시고, 물심양면으로 도와주시는 장인어른과 장모님께도 감사드립니다. 특히, 먼저

걸으셨던 학문의 길을 바탕으로 많은 조언과 함께, 할 수 있다는 용기를 계속 불어넣어주신 장모님께 더욱 머리 숙여 감사 드립니다.

마지막으로, 그 어떤 표현으로도 고마움을 다 표현하기에 부족한 사랑하는 아내이자 동반자인 김수안님께 깊이 감사드립니다. 당신의 지지와 희생이 있었기에 오랜 기간 동안 연구에 몰입할 수 있었습니다. 더욱이, 과정을 중도에 포기해야 할 정도로 큰 위기가 닥쳤을 때, 당신이 보여준 깊은 통찰력과 행동력이 없었다면 결단코 과정을 무사히 마치지 못했을 것입니다. 정말로 감사하고 또 감사합니다.

부담될까 봐 어떻게 되고 있냐고 자주 물어보시지도 못하고 속으로만 노심초사하셨던 어머니. 그리고 학위 과정 마치기를 늘 바라셨지만 끝내 보지 못하고 눈을 감으신 아버지. 이제서야 인생에 점 하나 무사히 찍었습니다. 늦어서 죄송합니다.